Principles for Open-Arc Weld Deposition of High-Chromium White Iron Surface Layers

John Anthony Francis

Department of Mechanical Engineering
The University of Adelaide

July 1999

A thesis submitted to The University of Adelaide
for the degree of Doctor of Philosophy

TABLE OF CONTENTS

LIST OF FIGURES

LIST OF TABLES

LIST OF SYMBOLS

a	fitted parameter for deposition rate equation (eq. 2.4)
A	cross-sectional area of a weld bead
$a_1, \ldots, a_5$	fitted constant terms or indices (general)
A_d	cross-sectional area of weld bead resulting from material deposited in that pass
A_m	cross-sectional area of material that is melted in an overlapping bead, excluding the area that is contributed by material that is deposited in that pass
$A_{s(ov)}$	cross-sectional area of substrate melted per pass in a multi-pass overlay under steady-state conditions
$A_{s(sb)}$	cross-sectional area of substrate melted in a single-bead deposit
A_{st}	cross-sectional area of steel melted
A_{wi}	cross-sectional area of white iron melted
b	fitted parameter for deposition rate equation (eq. 2.4)
B	width of steel substrate (Fig. 5.5)
$b_1, \ldots, b_5$	fitted constant terms or indices (general)
$[C]$	carbon concentration in the deposit
C_1, C_2	fitted parameters for bead width equation (eq. 3.4)
$[C]_{awm}$	carbon concentration in an all-weld-metal deposit
$[C]_{eut}$	average carbon concentration in the eutectic constituent
$[C]_m$	average carbon concentration in the matrix constituent
$[Cr]$	chromium concentration in the deposit
$[Cr]_{awm}$	chromium concentration in an all-weld-metal deposit
d	diameter of welding consumable
D	dilution of a weld deposit (general)
D_1	steady-state dilution of first layer
D_2	steady-state dilution of second layer with respect to substrate
$D_{2/1}$	steady-state dilution of second layer with respect to first layer

D_{av}	average dilution of a multi-pass deposit
$D_{n(sb)}$	normalised single-bead dilution
D_{ov}	steady-state dilution of a multi-pass overlay
D_{sb}	single-bead dilution
$D_{sb/wi}$	dilution of a single bead deposited on to white iron
E_{fm}	change in enthalpy required to melt filler material
E_s	change in enthalpy required to melt substrate
f	wire feed rate
$F(\ )$	a mathematical function (eq. 3.2)
G	gas flow rate
h	single-bead height
H_{av}	average height of a multi-pass deposit
H_p	peak height of a bead in a multi-pass overlay under steady-state conditions
H_{ss}	average height of a multi-pass overlay under steady-state conditions
HD_{com}	hardness of a composite material
HD_c	microhardness of the carbide phase
HD_m	microhardness of matrix constituent
I	welding current
k	area fraction of a bead contributed by material deposited in that pass
K	fitted constant parameter (eq. 2.6)
k'	thermal conductivity
l	work distance
L	length of an overlay
m	mass of welding consumable per unit length
n	dimensionless operating parameter
N	number of beads in an overlay
p	single-bead penetration
P_{av}	average penetration of a multi-pass deposit

P_{ss}	average penetration of a multi-pass overlay under steady-state conditions
$PCVF$	primary carbide volume fraction
q	fitted parameter in wear resistance equation (eq. 4.5)
R	peak-to-valley ripple for a multi-pass overlay under steady-state conditions
S	travel speed
t	total welding time
T_o	initial substrate temperature
T_c	chosen reference temperature
$TCMF$	total carbide mass fraction
$TCVF$	total carbide volume fraction
V	welding voltage, measured from the contact tip to the work piece
V_a	arc voltage
V_{fm}	volume of filler material deposited in a single pass
v	volume fraction of the reinforcing phase present in the material
v_i	volume fraction of i^{th} phase present in the material
w	single-bead width
w_n	normalised single-bead width
W	deposition rate
W_c	wear rate of a composite material
W_c^{-1}	apparent wear resistance of a composite material
$W_{dendrites}^{-1}$	apparent wear resistance of dendrites
$W_{eutectic}^{-1}$	apparent wear resistance of eutectic constituent
W_i	wear rate of i^{th} phase
W_i^{-1}	apparent wear resistance of i^{th} phase
W_m	wear rate of matrix constituent
W_m^{-1}	apparent wear resistance of matrix constituent
$W_{primary\ carbides}^{-1}$	apparent wear resistance of primary carbides
W_r	wear rate of reinforcing constituent

W_r^{-1}	apparent wear resistance of reinforcing constituent
w^*	width of melting parabola in geometric model
$[x]_{awm}$	concentration of element x in an all-weld-metal deposit
$[x]_{bm}$	concentration of element x in the base material
$[x]_i$	concentration of element x in the i^{th} bead of a multi-pass overlay
$[x]_{ss}$	concentration of element x in a multi-pass overlay under steady-state conditions
z	width of the parabolic function representing the steady-state bead profile
α	fitted parameter for single-bead dilution equation (eq. 2.2)
α'	thermal diffusivity
β	fitted parameter for single-bead dilution equation (eq. 2.2)
γ	$A_{s(ov)}$ as a fraction of $A_{s(sb)}$ for a matching single-bead deposit
δ	step-over between adjacent weld beads in a multi-pass overlay
η_a	arc efficiency
η_d	deposition efficiency
η_m	melting efficiency
θ	bead wetting angle (see Figure 3.4(b))
θ_g	gun angle
θ_r	angle of rotation used in geometric model
λ	area fraction of a bead contributed by material from the previous bead
ρ	density of an all-weld-metal deposit
ρ_c	density of carbide phase
ρ_m	density of matrix constituent
ϕ	overlap between adjacent weld beads in a multi-pass overlay

ABSTRACT

This study examines the mechanisms controlling the dilution, geometry and wear performance of weld-deposited high-chromium white iron surface layers. These layers are often deposited on steel components when resistance to abrasion is required. Manual-metal-arc welding (MMA) and flux-cored-arc welding (FCAW) are the processes most frequently employed to deposit such overlays. This work focuses on layers deposited by mechanised FCAW, as this process achieves higher deposition rates than MMA welding and affords a greater degree of control over individual welding variables.

Attention is first given to the factors affecting the dilution and geometry of single-bead deposits. The work presented in previous studies is reviewed and the findings are explained with reference to the welding literature. The findings of previous studies are also compared with results obtained in the current work. Expressions for the single-bead width and height are presented.

The wear performance of high-chromium white iron weld deposits is addressed. Wear testing was conducted both under laboratory conditions and in a series of field trials. The results of both sets of experiments are presented. The observed trends are then discussed and compared with the results of previous studies.

The mechanisms controlling dilution in multi-pass overlays were found to be different to those controlling the dilution of a single-bead deposit. Consequently, two distinct approaches were developed for predicting dilution in multi-pass overlays deposited in the

down-hand position. The first approach is semi-empirical and the second is based on first principles and geometry. The trends in the output data from each model were in close agreement. This agreement and the accuracy of the predictions provided a level of confidence in the output and, as such, the models could be used to draw conclusions and identify trends over a broader range of welding conditions.

This work culminates in what is believed to be the first set of working principles for the deposition of high-chromium white iron multi-pass overlays. Until now, the two most important features of a multi-pass overlay, namely the composition and geometry, had been determined by a trial-and-error process or retrospectively. It is believed that these principles will substantially improve the production and performance of weld overlays.

DECLARATION

This work contains no material which has been accepted for the award of any other degree or diploma in any university or other tertiary institution and, to the best of my knowledge and belief, contains no material previously published or written by another person, except where due reference has been made in the text.

I give consent to this copy of my thesis, when deposited in the University Library, being available for loan and photocopying.

John Francis

Department of Mechanical Engineering
The University of Adelaide

July 1999

PUBLICATIONS

Portions of this work appear in the following articles:

- ARNOLD, B.K., BEDNARZ, B., FRANCIS, J.A., JONES, E.P. and BEE, J. (1998): "Principles for Weld Deposition of Hardfacing – Field Trials", CRC Project 95:23, Final Report – Part 2.

- FRANCIS, J.A. and JONES E.P. (1997): "The Influence of Welding Parameters on the Wear Performance of High Chromium White Iron Hardfacing Alloys", *WTIA National Seminars*, July, Mackay, Australia.

- FRANCIS, J.A., BEDNARZ, B., ARNOLD, B.K., JONES, E.P. and BEE, J. (1998): "Principles for Weld Deposition of Hardfacing", CRC Project 95:23, Final Report – Part 1.

- POWELL, G.L.F., FRANCIS, J.A., BEDNARZ, B. and LLOYD, P.G. (1997): "Undercooling and Welding Metallurgy", Paper 49 in Proceedings of the Conference *Technological Developments and Advances for Australian Industry*, November, Melbourne, Australia.

- YELLUP, J.M., ARNOLD, B.K., FRANCIS, J.A. and BEE, J.V. (1996): "Development of a Hardfacing Procedure – The Significance of Welding Parameters", *WTIA National Seminars*, July - August, Gladstone, Perth and Newcastle, Australia.

ACKNOWLEDGMENTS

This work formed part of Project CRC 95:23, a broader project investigating the effects of welding parameters on the wear performance of hardfacing overlays. In particular, I would like to express my gratitude to the Cooperative Research Centre for Materials Welding and Joining for providing a financial scholarship which made this work possible. The project itself was conceived and initiated by WTIA Panel 8, "Reclamation", and I am grateful for the support and encouragement given by the members of this panel.

I would like to thank Dr. John Bee of The University of Adelaide for his supervision, guidance and good humour.

I am grateful for the supervision and guidance of Dr. John Yellup, formerly with CSIRO Manufacturing Science and Technology, in the early part of this work.

Several other people were always willing to assist me with my work. In particular I would like to thank:

- Dr. Bernie Bednarz (CSIRO), project leader for CRC 95:23, who deserves special mention for his inspiration, guidance and friendship.
- Professor Ian Henderson, formerly with the Department of Mechanical Engineering at The University of Adelaide.
- Mr. Rick Gorman, formerly with Weldtronics Ltd., for invaluable discussions on many occasions.

- Mr. Geoff Goss for his enthusiasm and assistance with many of the experiments and his valuable advice on record keeping.
- Mr. Mark Banks and Mr. John Milde of Boral Quarries for their cooperation with the heel plates experiment in chapter 5.
- Mr. David Viano (CSIRO) for his advice and assistance in preparing this thesis.
- Mr. Theo Heijkoop and Mr. Phil Pederson (CSIRO) for casting the white iron bars used in the GTAW welding experiments in chapter 7.
- Mr. Brian Arnold and Mr. Ted Jones (CSIRO) for their assistance and advice on general experimental matters.
- Mr. Ken Barton and Mr. Mike Pullen (CSIRO) for their assistance with welding matters.
- Mr. Trevor Kenyon (CSIRO) for assistance and advice in preparing this thesis.
- Mr. Laurie Jarvis and Dr. Wojtek Mazur (CSIRO) for valuable discussions.
- Mr. John Terlet (The University of Adelaide – CEMMSA) for his assistance and advice relating to metallography.

Finally, I would like to thank my family for their support and encouragement.

To My Parents

Anthony John Francis

and

Kathleen Frances Chesher

1
INTRODUCTION

Hardfacing refers to a process in which a hard surface layer is deposited on to a component in order to improve its wear resistance. An arc welding process is often employed to deposit the layer when resistance to abrasion is required. High-chromium white iron alloys are the most widely used overlay materials in applications involving abrasive wear.

A great deal of research effort has been directed at studying the factors affecting the wear performance of high-chromium white irons. Unfortunately, the majority of these studies have focussed on the wear performance of white iron castings and little effort has been devoted to weld deposits, despite their widespread use in industry. This is possibly related to the flexibility that casting processes offer with regard to the range of heat treatments and microstructures that can be achieved. For practical reasons weld deposits are usually left in the as-welded condition and, in that regard, the range of attainable microstructures is reduced. However, another significant difference arises in that, until now, casting processes have offered a greater degree of control of the alloy composition. The composition of a casting is determined before the process proceeds, whereas with a weld deposit the composition is essentially determined by the dilution that occurs as the overlay is deposited. The dilution, in turn, is very sensitive to the selected welding parameters. At the time this work commenced the hardfacing industry did not have a formal or reliable procedure for predicting the dilution, and hence the composition of a

hardfacing overlay. Thus the most important variable has either been an unknown quantity or, at best, a quantity that is determined retrospectively.

The aims of this work were to identify the effects that welding parameters have on the dilution of a weld deposit and to develop principles for predicting and controlling overlay dilution. Attention was focussed on the flux-cored arc welding (FCAW) process and self-shielded high chromium, high carbon welding consumables. The terminology is somewhat of a misnomer in that the consumables studied were alloy-cored tubular electrodes, comprising a carbon-steel sheath and a fill with high-carbon ferrochromium as the main constituent. The contribution of flux to the core ingredients was small. This process was selected, however, primarily because it affords better control over process variables than manual-metal-arc welding. FCAW is an increasingly popular choice in the Australian hardfacing industry as it also offers higher deposition rates than manual-metal-arc welding. Electrodes 2.8mm in diameter are used extensively as they achieve higher deposition rates than consumables with smaller diameters. Most hardfacing in Australia is also performed with the direct-current, electrode-positive configuration (DCEP) and most manufacturers recommend using this polarity with their product. For these reasons, the emphasis was placed on DCEP hardfacing with 2.4 and 2.8mm diameter consumables.

This work commences with a review of the literature. The review is intended to provide the background for research described in later chapters, and it includes some analysis where appropriate. Attention is then given to single-bead deposits and, in particular, the factors affecting dilution, geometry, composition and abrasive wear performance under laboratory test conditions. Chapter 5 is concerned with a series of field trials that proved

to be a turning point in the work. In designing the experiments for these trials it was observed that minimising dilution in multi-pass overlays is a fundamentally different problem to minimising the dilution of a single-bead deposit. Consequently chapters 6 and 7 address the dilution of multi-pass overlays. Chapter 8 then describes, for the first time, a set of principles for open-arc weld deposition of both single-bead and multi-pass overlays. Finally, conclusions and suggestions for future research are presented in chapter 9.

2

A REVIEW OF THE LITERATURE

2.1 INTRODUCTION

Hardfacing is a complicated subject as it embraces aspects of welding technology, materials science and wear. While there have been many studies that focus on one or two of these particular aspects, few have dealt with all three. Consequently, this review addresses each aspect sequentially and draws on the relevant studies in each case. Sections 2.2 to 2.4 are concerned with various aspects of welding science, section 2.5 deals with the metallurgy of high-chromium white irons and section 2.6 addresses wear. Finally, section 2.7 outlines the rationale for the current work.

2.2 THE EFFECTS OF WELDING PARAMETERS ON DILUTION

2.2.1 Dilution – Its Definition and Significance

The ASM Handbook (1993a) defines dilution as:

"The change in chemical composition of a welding filler metal caused by the admixture of the base metal or previous weld metal in the weld bead. It is measured by the percentage of base metal or previous weld metal in the weld bead."

Dilution occurs when a volume of deposited filler material is mixed with a volume of substrate material. However, if dilution is to be measured by metallographic methods it is typically calculated in terms of a ratio of areas, as illustrated in Figure 2.1.

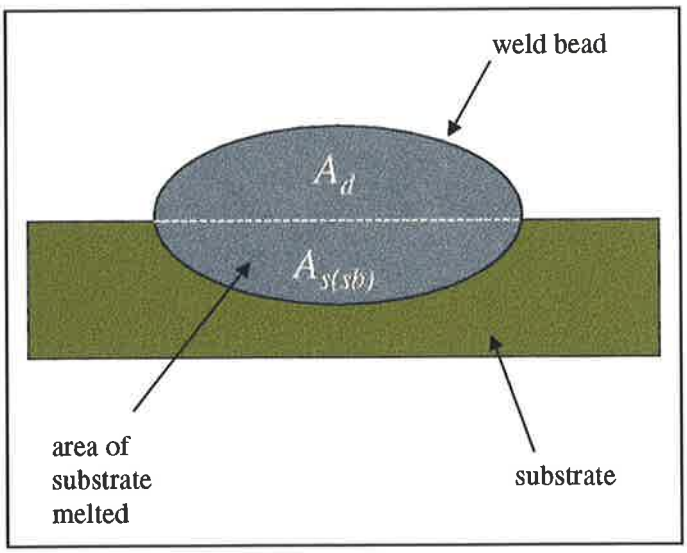

$$Dilution,\ D_{sb} = \frac{A_{s(sb)}}{A_{s(sb)} + A_d} \quad (0 \le D_{sb} \le 1) \quad \ldots\ldots\ldots \quad (2.1)$$

Figure 2.1: - The metallographical measurement of dilution for a single-bead deposit. $A_{s(sb)}$ is the cross-sectional area of substrate melted and A_d is the cross-sectional area of material deposited.

This method of measurement is acceptable provided that the individual cross-sectional areas do not vary along the length of the weld.

Dilution is a parameter of prime importance because weld surfacing usually involves the joining of two materials with very different compositions. The substrate is often a steel containing 0.1-0.2 wt.% carbon and no chromium, whereas a typical welding consumable contains 5 wt.% carbon and 25 wt.% chromium. It can be seen that even a small change in dilution will result in a significant change in overlay composition, and hence microstructure and wear properties.

2.2.2 Previous Dilution Studies

It has long been known that the selected welding parameters affect the dilution and hence wear performance of high-chromium white iron overlays. Avery and Chapin (1952), in their study, made the following statement: *"The difference in performance due to welding technique is as great or greater than variations that can be assigned to (consumable) composition."* Despite this knowledge, there have been few studies investigating the role that welding parameters play in determining the overlay dilution. The most comprehensive studies were those of Thorpe (1980), Rense *et al.* (1983), Ellis and Garrett (1986) and Yellup and Smoker (1995). Each of these studies examined the effects of a range of different process variables. Rather than describe the findings in relation to individual parameters, a brief description is given of each study. A summary of the findings relating to each parameter is then given in Table 2.1. Trends in Table 2.1 are identified and explained with reference to the welding literature.

2.2.2.1 Thorpe (1980)

Thorpe prepared a range of three-layer deposits. The first layer of three beads was deposited with direct-current, electrode-positive polarity (DCEP), whereas the second layer, comprising two beads, and a third comprising one bead were both deposited with direct-current, electrode-negative polarity (DCEN). A 2.8mm diameter, self-shielding austenitic chromium-carbide-type consumable was used. A fully automatic flux-cored arc welding system was chosen to deposit the samples. It was found that dilution varied systematically with voltage but not with current. The effects of travel speed and work distance on dilution were also investigated.

Thorpe concluded that there was a trade-off between bead profile and the desired low-dilution microstructures.

2.2.2.2 Rense, Edwards and Frost (1983)

Heat input is a parameter of prime importance in many welding applications. Rense *et al.* (1983) selected combinations of parameters in such a way that they would detect any correlation between dilution and heat input. Each sample comprised a single-layer white iron overlay with overlapping beads. The voltage, current and travel speed were varied so that one of three heat input conditions were achieved, namely 1, 2 or 5kJ/mm. In this study it was found that there was no correlation between dilution and heat input, but that there was a correlation between dilution and current with an increase in current resulting in a reduction in dilution. However, the experimental design did not involve changing one parameter independently of another. The reduction in dilution observed by these workers could well have resulted from the simultaneous decrease in voltage (see Yellup and Arnold, 1996).

2.2.2.3 Ellis and Garrett (1986)

Ellis and Garrett reported work by Ellis (1985), who used factorial design to plan his experiments. The experiments included the deposition of sixty-four single beads on mild steel bars. The effects of such variables as arc polarity, voltage, current, travel speed, work distance and preheat temperature were considered. The welding consumable was 2.8mm in diameter, high in chromium but low in carbon. The major finding in this work was that there was an interaction between current and polarity in determining the dilution of the deposits. If DCEN polarity were used, increases in

current would result in reduced dilution. However, if DCEP polarity was used an increase in current resulted in a slight increase in dilution.

2.2.2.4 Yellup and Smoker (1995)

These workers used a 2.4mm diameter austenitic chromium-carbide-type consumable to deposit a range of multi-pass overlays. The effects of voltage, current, travel speed, torch angle and overlap were considered. Voltage was found to have the strongest effect on dilution with an increase in voltage leading to an increase in dilution. An increase in bead overlap was found to reduce the dilution in the case of multi-pass deposits.

2.2.2.5 Other Studies

Raveendra and Parmar (1987) and Martin *et al.* (1991) used factorial design techniques to study the geometry of single beads of steel deposited by flux-cored arc welding. They generated empirical equations for many parameters including dilution.

Kim, Basu and Siores (1994) studied single beads of steel deposited with the Gas-Metal Arc welding process (GMAW) and fitted their dilution data to an expression of the form:

$$D_{sb} = 10^{a_1} d^{a_2} S^{a_3} I^{a_4} V^{a_5}$$

where D_{sb} is the single-bead dilution, d is the diameter of the consumable, S is travel speed, I is current, V is voltage, and a_1, a_2, a_3, a_4 and a_5 are fitted constants. The effect that each parameter had on the dilution was inferred from the value of the index for that parameter.

Kalligerakis and Mellor (1994) studied overlay welding with stainless steel. The welding consumable was a 1.2mm diameter type 316 solid wire and the base metal was mild steel. The samples prepared by these workers comprised single beads-on-plate. Dilution was found to increase with increasing current.

Kotecki (1996) deposited a number of stainless steel overlays comprising overlapping beads with the submerged-arc welding technique. He found that by reducing the step-over between adjacent beads a very low dilution deposit could be achieved.

Table 2.1 summarises the findings of the major studies. For each welding parameter such as voltage or current, there is a box assigned to each publication. In each box there is an entry. An upward pointing arrow indicates that an increase in the welding parameter results in an increased dilution according to the findings of the study. Similarly, a downward pointing arrow indicates that an increase in the welding parameter will result in a reduction in dilution. If the entry is "~" the findings were inconclusive, or there was no noticeable trend, while "*N/C*" denotes that the particular parameter was not considered in the study.

2.2.3 The Effects of Voltage on Dilution

It can be seen that all of the studies that investigated the effect of voltage on dilution found that an increase in voltage resulted in an increase in dilution. This is in agreement with a first-principles model initiated by Deam (1996) and developed by Bednarz (1996). The resulting equation is described in Francis *et al.* (1998), where it was seen that the model described the single-bead dilution data obtained from two 2.8mm diameter chromium-carbide-type consumables. The equation is:

Study	Overlay Material	Voltage	Current	Work Dist.	Speed	Preheat Temp.
Thorpe (1980)	white iron	↑	~	↓	~	*N/C*
Rense *et al.* (1983)	white iron	↑	↓	*N/C*	*N/C*	*N/C*
Ellis and Garrett - DCEP (1986)	stainless steel	↑	↑	~	↑	↑
Ellis and Garrett - DCEN (1986)	stainless steel	↑	↓	~	↑	↑
Raveendra and Parmar (1987)	steel	↑	↓	↓	*N/C*	*N/C*
Martin, Taylor and Bahrani (1991)	steel	↑	*N/C*	↓	↑	*N/C*
Kim, Basu and Siores (1994)	steel	↑	↓	*N/C*	↑	*N/C*
Kalligerakis and Mellor (1994)	stainless steel	*N/C*	↑	*N/C*	*N/C*	*N/C*
Yellup and Smoker (1995)	white iron	↑	~	*N/C*	~	*N/C*

Table 2.1: - A summary of the influence of welding parameters on dilution according to previous studies. In all cases the substrate materials were mild steel.

$$\frac{D_{sb}}{1 - D_{sb}} = \alpha \frac{VI}{W}\left(1 + \beta V I S\right) \quad \ldots\ldots\ldots \quad (2.2)$$

where D_{sb} is the single-bead dilution, V is the contact tip-to-work voltage, I is the current, W is the deposition rate, S is the travel speed and α and β are fitted constants depending on the combination of welding consumable and substrate. Equation 2.2 suggests that the single-bead dilution generally increases with increasing voltage.

DuPont and Marder (1996) also modelled single-bead dilution. They arrived at an expression of the form:

$$D_{sb} = \frac{1}{1 + \dfrac{V_{fm} E_s}{\eta_a \eta_m VI - E_{fm} V_{fm}}} \quad \ldots\ldots\ldots \quad (2.3)$$

where V_{fm} is the volume of filler metal deposited, E_s and E_{fm} are the changes in enthalpy required to melt substrate and filler metal respectively while η_a and η_m are the arc and melting efficiencies respectively. If it is assumed that the deposition rate, and hence V_{fm}, does not change with voltage (see Lesnevich, 1958), then D_{sb} in equation 2.3 monotonically increases with increasing voltage.

Farmer (1966a) described the effect that arc voltage has on single-bead dilution. An increase in voltage results in an increase in arc energy. The deposition rate, however, generally does not increase as the voltage increases. The increase in arc energy will result in more substrate being melted and, if the deposition rate does not increase, a higher dilution.

2.2.4 The Effects of Welding Current on Dilution

There are conflicting conclusions regarding the effect of welding current on single-bead dilution. Dilution depends on the amount of substrate melted as well as the amount of material deposited and welding current has an effect on both of these parameters. In order to appreciate how conflicting trends may arise it is necessary to consider the relationship between the current and the deposition rate. Lesnewich (1958) and Halmøy (1979) studied solid-wire GMAW and arrived at an expression of the form:

$$W = a I + b l I^2 \quad \ldots\ldots \quad (2.4)$$

where W is deposition rate, I is current, l is work distance and a and b are constants depending on the wire diameter, electrode material and shielding gas. This form of expression has also been obtained by other workers (Rhee and Kannatey-Asibu, 1993; Hirata, 1995). Equation 2.4 suggests that the deposition rate is independent of the welding voltage. It is known, however, that deposition rate can vary with voltage in such a way that an increase in voltage causes a reduction in deposition rate (Kiyohara *et al.*, 1980). Nevertheless equation 2.4 does prove useful in estimating the deposition rate with both solid and flux-cored wires (Ushio *et al.*, 1985). If it is substituted into equation 2.2 the result is:

$$\frac{D_{sb}}{1 - D_{sb}} = \frac{\alpha V}{a + b l I} + \frac{\alpha \beta V^2 I S}{a + b l I} \quad \ldots\ldots \quad (2.5)$$

The second term in equation 2.5 is monotonically decreasing in I and the third term is monotonically increasing. Equation 2.5 suggests that dilution could either increase or decrease with increasing current, depending on the term that dominates. Thus the Bednarz-Deam model for single-bead dilution appears to account for the seemingly contradictory findings in previous dilution studies. It suggests that the effects of welding current on single-bead dilution are not immediately evident, and that they will depend on the characteristics of the particular combination of substrate and consumable.

2.2.5 The Effects of Work Distance on Dilution

Three studies found that an increase in work distance resulted in a reduction in dilution. Thorpe (1980) concluded that the decreased dilution resulted from a reduction in arc voltage, due to an increase in the voltage drop between the contact tip and the tip of the electrode. Hinkel (1968) also acknowledged that there is a significant voltage drop associated with the electrode extension and estimated that it could be as high as 3 volts (V). French (1984) measured these voltage drops for flux-cored consumables and obtained values ranging from 0.5 to 4.5 volts (V); values which may be large enough to explain the observed reductions in dilution.

Another issue arises in that the work distance affects the deposition rate. Smith (1970) gave an example where the welding current could be reduced by 40%, while maintaining a constant deposition rate, by increasing the work distance from 25 to 95mm. The lower current will result in less substrate being melted and, since the deposition rate remains unchanged, a reduction in dilution. Conversely, if a constant current is maintained while the work distance is increased, there will be an increase in deposition rate according to equation 2.4. This will result in a larger cross-sectional area of deposited material and, since the amount of substrate melted will not increase, a lower dilution.

The only other work to consider the effect of work distance was that of Ellis and Garrett (1986). They found that there was no significant change in dilution as the work distance was changed. They did not, however, cover a wide range of work distances (see Ellis, 1985).

2.2.6 The Effects of Travel Speed on Dilution

Three of the studies found that dilution increases as the travel speed increases. In other work, Forsberg (1985) and Oh *et al.* (1990) also found that dilution increases with travel speed when cladding with strip electrodes. These findings are consistent with equation 2.2 and the Bednarz-Deam model for single-bead dilution.

The model developed by DuPont and Marder (see equation 2.3) does not directly suggest that an increase in travel speed results in an increase in dilution. However, the effect of travel speed may be accounted for by a change in the melting efficiency, η_m. DuPont and Marder define the melting efficiency as the ratio of energy used for melting to that which is delivered to the work piece. The melting efficiency has been shown to increase as the travel speed increases (Wells, 1952; Swift-Hook and Gick, 1973), and DuPont and Marder concluded that the increase in dilution with travel speed occurs as a direct result of the associated increase in melting efficiency.

2.2.7 The Effects of Preheat Temperature on Dilution

Ellis and Garrett (1986) considered the effects of preheat temperature. They found that an increase in preheat temperature resulted in an increase in dilution. Hotter substrates require less energy to reach their melting point. For a given heat input, an increase in preheat temperature will result in a greater amount of substrate material reaching the melting temperature. A higher dilution will result.

2.2.8 The Effects of Bead Overlap on Dilution

Yellup and Smoker (1995) and Kotecki (1996) both found that an increase in overlap, or a reduced step-over, resulted in reduced dilution for multi-pass single-layer deposits.

2.3 FACTORS AFFECTING WELD BEAD GEOMETRY

The prediction of weld bead geometry is an important step in the development of welding procedures. This section commences with a description of the analytical solutions for the temperature distribution in a weldment, and the weld bead geometry predicted by these solutions. The physical effects leading to discrepancies between the predicted and observed geometries are next to be addressed. Finally, some of the empirical correlations in the literature are discussed.

2.3.1 Studies Treating the Arc as a Point Source of Heat

Rosenthal (1941) was one of the first to present a solution for the temperature distribution in weldments. His solution applies to the case of a single bead being deposited on to a semi-infinite plate. The arc was assumed to be a point source of heat moving along the surface of the plate at a constant velocity. Physical properties such as density, specific heat and thermal conductivity were assumed to remain constant.

Christensen *et al.* (1965) generalised the early work of Rosenthal to arrive at a dimensionless temperature distribution for point sources. This distribution was compared with the results of experiments and measurements of weld pool geometry. The isotherm corresponding to the melting temperature of the material was the predicted fusion line. This isotherm is semi-circular and, as such, the predicted fusion line is a semi-circle. The predicted weld bead penetration is equal in magnitude to the radius of this semi-circle, whereas the predicted bead width is twice this value.

Christensen *et al.* found that there was good agreement between the predicted fused areas and those observed in experiment but, for most welding conditions, the weld bead

width was underestimated. They concluded that the semi-circular fusion line required by theory was not borne out in experiment.

2.3.2 Studies Treating the Arc as a Distributed Source of Heat

Rykalin (1951) acknowledged that the arc is a distributed source of heat. He argued that the arc produces heat at the cathode spot by direct conversion of the energy of electrically-charged particles into thermal energy. In addition, the region immediately adjacent to the cathode spot was said to receive thermal energy from the arc by convection and radiation. Rykalin pointed out that heating from the arc diminishes with increasing distance from the centre of the cathode spot and argued that the spatial distribution of heating could be approximated by the normal probability (or Gaussian) distribution.

Eagar and Tsai (1983) adapted Rosenthal's solution for the temperature distribution in a weldment and treated the heat flux from the arc as a Gaussian distribution. They demonstrated that, when predicting bead geometry, significant improvements over earlier models could be achieved. The depth-to-width ratios predicted by Eagar and Tsai achieved better agreement with experiment than the semi-circular fusion lines predicted by Rosethal (1941) and Christensen *et al.* (1965).

2.3.3 Weld Pool Convection and Its Effect

It is now known that the location of the fusion line is strongly influenced by convection in the weld pool (Kou and Wang, 1986). Fluid flow within the weld pool can result from surface tension gradients, the electro-magnetic force and the buoyancy force. The mechanism is described in each case.

2.3.3.1 Surface tension gradients

Heiple and Roper (1982) demonstrated the effects that surface tension gradients have on weld bead geometry. The gradients arise because there are temperature gradients within the weld pool and surface tension is a temperature-dependent property. If the surface tension within the weld pool decreases with increasing temperature (*i.e.* a negative gradient) the surface tension at the centre of the weld pool will be lower than at the periphery. The resulting convection pattern will be as shown in Figure 2.2(a). Heiple and Roper stated that it is normal for pure materials to exhibit a negative gradient. If, however, the surface tension of an alloy increases with increasing temperature (a positive gradient), the resulting convection pattern will be as shown in Figure 2.2(b). Heiple and Roper proposed that, for iron and steels, the presence of surface-active elements such as sulphur and oxygen produced a positive gradient.

A positive surface tension gradient favours the transfer of heat from the arc to the bottom of the pool thus producing deeper penetration. A negative surface tension gradient, however, retards the flow of metal from the top to the bottom of the pool and the resultant penetration is shallow (Kou and Wang, 1986).

2.3.3.2 The electro-magnetic force

The diverging electric current field in the weld pool creates a downward electro-magnetic force near the centre of the weld pool and pushes liquid metal in that region downward toward the bottom of the pool (Kou and Sun, 1985). Thus the electro-magnetic force favours a convection pattern such as that shown in Figure 2.2(b).

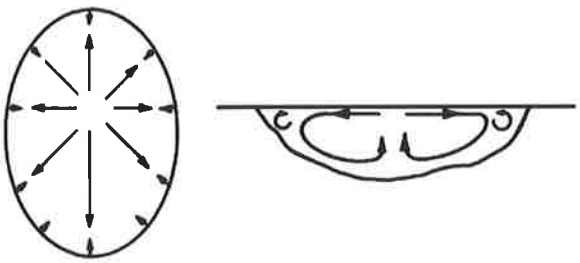

Figure 2.2(a): - Schematic representation of the flow pattern on the weld pool surface and the sub-surface flow pattern for a negative surface tension gradient (after Heiple and Roper, 1982).

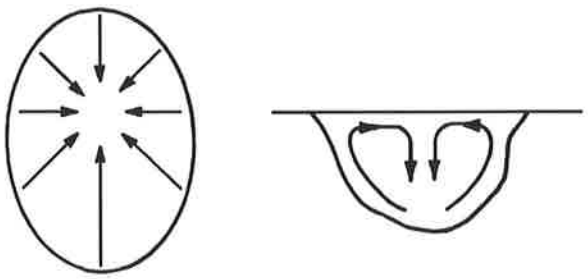

Figure 2.2(b): - Schematic representation of the flow pattern on the weld pool surface and the sub-surface flow pattern for a positive surface tension gradient (after Heiple and Roper, 1982).

2.3.3.3 Buoyancy

Under the influence of the buoyancy force the hotter liquid metal near the central region of the weld pool floats to the surface, while the cooler liquid metal near the pool boundary sinks to the bottom of the weld pool (Kou and Sun, 1985). Thus buoyancy effects favour a convection pattern such as that shown in Figure 2.2(a).

2.3.3.4 Combined driving forces

In arc welding there are several different driving forces for weld pool convection acting simultaneously. The convective flow direction will be governed by which driving force is dominant. However, it is possible for two flow loops of opposite directions to co-exist in a weld pool, the upper one being dominated by the surface tension gradient and the lower one by the electromagnetic force (Kou and Sun, 1985).

Kim and Na (1995) performed computer simulations of the 3-dimensional heat transfer and fluid flow within the weld pool for GMAW. In their work they calculated the position of the fusion line due to pure conduction with a distributed source of heat. They also calculated the location of the fusion line including the influences of three driving forces for convection; the electromagnetic force, surface tension and buoyancy. The results are shown in Figure 2.3.

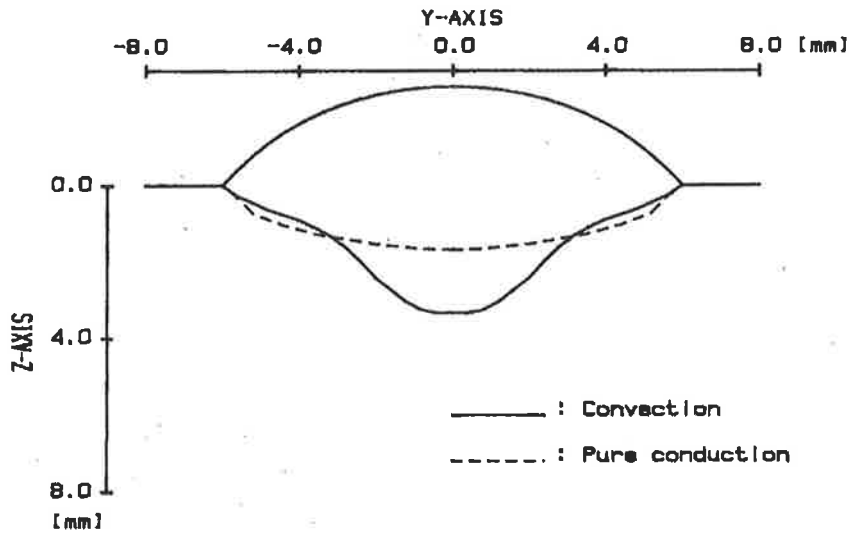

Figure 2.3: - A comparison of the calculated weld bead shapes for two different calculation methods (after Kim and Na, 1995). The electrode and substrate were both mild steel.

In section 2.3.1 it was noted that, for a point source of heat, the predicted fusion line was semi-circular. Figure 2.3 shows that pure conduction with a distributed source of heat produces a weld pool that is wider and approximately parabolic in shape. It is also evident that liquid metal flow plays an important role in the formation of the finger-like penetration profile frequently seen in GMAW welds. Kim and Na concluded that the electromagnetic force was the dominant driving force for liquid metal flow. They also found that the finger-like penetration profile was particularly prominent at low work distances. It was suggested that at low work distances the arc length is reduced and the current flux constricted, resulting in a large electro-magnetic force.

2.3.4 Weld Pool Depression and Its Effect

At high welding currents the surface of the molten weld pool becomes depressed, favouring transfer of heat from the arc to the root of the weld and producing a higher penetration (Friedman, 1978).

Friedman attributed the depression of the weld pool to the increase in arc pressure, since the force that the plasma jet imparts on the weld pool has been shown to increase with the square of the current (Lin and Eagar, 1986). However, Lin and Eagar (1985) in an earlier study, and later work by Rokhlin and Guu (1993) found that arc pressure alone could not explain the observed surface depression. Lin and Eagar developed a model of a compound vortex in the weld pool. This model did explain the surface depression and at the same time predicted a hysteresis in the relation between weld pool depression and current, the hysteresis being caused by vortex inertia. Hysteresis was not, however, observed by Rokhlin and Guu. Their results did not conclusively support the vortex model and they concluded that more work was required to explain the phenomenon of

weld pool depression. It was suggested that the electro-magnetic force, associated with the diverging current path in the weld pool, may play a significant role in the formation of the weld pool depression. This suggestion is supported by the work of Erokhin (1979), who suggested that there is no sense in separating the arc force from the electro-magnetic force in the plate. He measured the sum of these forces and obtained results that can explain weld pool depression.

2.3.5 Studies Considering the Effects of the Molten Droplets

Kim and Na (1995) considered the effects that the molten droplets travelling across the arc zone have on the shape of the weld pool. These effects were combined with those of a distributed source of heat, weld pool convection and depression. It was found that, when all of the influences were combined, a computer simulation could accurately predict the geometry of GMAW weld beads.

Kim and Na found that the inclusion of the molten droplets in the analysis resulted in an increase in penetration and an enhancement of the finger-like penetration profile. It should be noted, however, that the mode of metal transfer was assumed to be spray transfer. The effects of the molten droplets may vary if the transfer is globular, as is the case for most open-arc hardfacing consumables.

2.3.6 Prediction of Weld Bead Geometry

This section describes some empirical approaches for predicting weld bead geometry. All of the examples presented were derived from experiments involving a steel substrate and consumable. The parameters of main interest are penetration, and bead width and height. Work relating to each of these parameters will be considered separately.

2.3.6.1 Predicting penetration

McGlone (1982) in his review found that there was consensus in the literature regarding the effects of welding parameters on penetration. Penetration was primarily influenced by welding current, with an increase in current resulting in an increase in penetration. The work of Jackson and Shrubsall (1953) utilised an equation for penetration attributed to Gunnert. The equation combines the effects of voltage, V, current, I and travel speed S to predict penetration, p:

$$p = K \sqrt[3]{\frac{I^4}{S V^2}} \quad \ldots\ldots \quad (2.6)$$

where K is a constant depending on the characteristics of the welding process. This expression was obtained from samples deposited using the submerged-arc welding process.

Martin *et al.* (1991) examined the effects of welding parameters on the geometry of beads deposited by self-shielded flux-cored arc welding. They related the penetration, p, to the welding parameters with the following expression:

$$p = \text{constant} \times \frac{f^{1.213}\,\theta_g^{0.218}}{S^{0.096}\,l^{0.6}} \quad \ldots\ldots \quad (2.7)$$

where f is the wire feed rate, θ_g is the gun angle, S is the travel speed and l is the work distance. The strong dependence of penetration on current is evident in this case through the wire feed rate or deposition rate (see equation 2.4). The inclusion of other variables does, however, make it difficult to identify similar trends.

A different approach was adopted by Raveendra and Parmar (1987). They used fractional factorial techniques to develop mathematical models for predicting weld bead geometry. They considered the effects of voltage, current, travel speed, work distance and gun angle. This approach does consider a wide range of variables and possible interactions but leads to complicated relationships, such as the following twelve-term expression:

$$p = 3.487 + 0.356V + 0.338I - 0.400S - 0.088l - 0.356VI$$
$$-0.181VS + 0.200V\theta_g + 0.181Vl - 0.388Il - 0.156S\theta_g + 0.244\theta_g l \quad \ldots\ldots \quad (2.8)$$

where V is voltage, I is current, S is speed in mm/min, l is work distance in mm and θ_g is the gun angle in degrees.

2.3.6.2 Predicting bead width

Martin *et al.* (1991) and Kim *et al.* (1994) found that voltage was the dominant influence on bead width, with an increase in voltage resulting in an increase in bead width. Both of these works also found that an increase in travel speed resulted in a reduction in bead width. Raveendra and Parmar (1991) found that an increase in current increases the bead width, as did Kim *et al.* (1994).

Kim *et al.* (1991) obtained the following expression for bead width, w:

$$w = d^{0.3647} S^{-0.4873} I^{0.4151} V^{0.9273} \times \text{constant} \quad \ldots\ldots \quad (2.9)$$

where d is the consumable diameter, S is the travel speed, I is the welding current and V is the voltage.

Another expression was obtained by Martin *et al.* (1991):

$$w = \text{constant} \times \frac{V^{1.243} f^{0.221}}{S^{0.545} l^{0.09} \theta_g^{0.046}} \quad \cdots\cdots\cdots (2.10)$$

where V is voltage, f is wire feed rate, S is travel speed, l is work distance and θ_g is the gun angle.

2.3.6.3 Predicting bead height

Raveendra and Parmar (1987) and Kim *et al.* (1994) found that bead height increases with increasing current, while it decreases with increasing voltage and increasing speed. These findings agree with the work of Martin *et al.* (1991) who arrived at the following expression for bead height, h:

$$h = \text{constant} \times \frac{f^{0.933} \theta_g^{0.25}}{V^{0.417} S^{0.263} l^{0.239}} \quad \ldots\ldots\ldots (2.11)$$

where f is the wire feed rate, θ_g is the gun angle, V is the voltage, S is the travel speed and l is the work distance. The strong dependence of height on welding current is evident through the dependence on wire feed rate.

Unfortunately, with the wire feed rate as a variable, there is an implicit dependence on the consumable type. For the same wire feed rate, the deposition rate will change if the consumable diameter is changed.

Kim *et al.* (1994) also produced an expression for bead height:

$$h = d^{-0.4092} G^{-0.0844} S^{-0.4327} I^{0.7475} V^{-0.6649} \times \text{constant} \quad \ldots\ldots\ldots \quad (2.12)$$

where d is the electrode diameter, G is the gas flow rate, S is the travel speed, I is current and V is voltage. Both equations 2.11 and 2.12 predict that an increase in current will increase bead height and that increases in voltage and speed will reduce bead height.

2.4 HOMOGENEITY OF THE WELD BEAD

In continuous welds involving the deposition of filler material it is possible for macro-segregation to occur if mixing in the weld pool is insufficient. In arc welding, however, the electromagnetic force tends to promote bulk mixing within the weld pool (Kou and Wang, 1986). Even if double circulation loops are present, due to the combined action of different driving forces, it is anticipated that they will not prevent bulk mixing within the weld pool. The kinetic energy of the molten droplets, together with the force of gravity, will ensure that they are drawn into the lower circulation loop induced by the electro-magnetic force (Kou and Wang, 1986). These concepts are consistent with the findings of Houldcroft (1954), who observed a uniform composition in the bulk fusion zone of aluminium welds made with dissimilar filler materials. Kou and Wang (1986) did point out, however, that the velocity of the liquid metal at the pool boundary should be zero. They suggested that a thin unmixed layer of material would result adjacent to the interface, and noted that such an unmixed zone had been reported by Baeslack *et al.* (1979) and Lippold and Savage (1980). The unmixed zone so formed is represented schematically in Figure 2.4.

Powell (1979) studied hardfacing deposits, employing the manual-metal-arc technique, and identified a possible cause of inhomogeneity. He observed that in some instances

there were undissolved particles of ferrochromium present in the deposit. It is possible that, under certain conditions, ferrochromium particles in the welding consumable do not completely melt as they travel across the arc zone. Thorpe (1980) also observed some undissolved ferrochromium particles in his samples, but to a lesser extent. Thorpe employed FCAW and attributed the reduced occurrence to the higher heat input of this process. Noble (1985), in his review, suggested that another possible cause was variations in ferrochromium particle size between MMA and FCAW consumables.

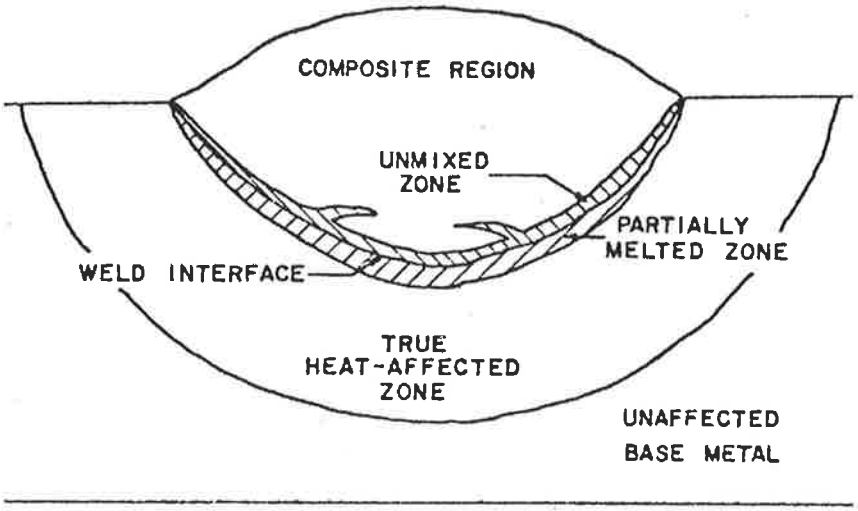

Figure 2.4: - Schematic illustration showing the regions of a heterogeneous weld (after Baeslack and Savage, 1979).

2.5 THE METALLURGY OF HIGH-CHROMIUM WHITE IRONS

In this section a brief description is given of the microstructures frequently observed in hardfacing weld deposits, and how they arise. The Fe-Cr-C liquidus surface is an appropriate starting point when studying the metallurgy of high-chromium white irons. The equilibrium phase diagram is described by Rivlin (1984) but, due to the rapid

cooling rates associated with arc welding, the metastable liquidus surface proposed by Thorpe and Chicco (1985) or Jackson (1970) is more appropriate. A recent study (de Sairre Balsamo *et al.*, 1995) found that the diagram proposed by Jackson (1970) adequately predicted weld-deposited high-chromium white iron microstructures. Jackson's diagram is shown in Figure 2.5.

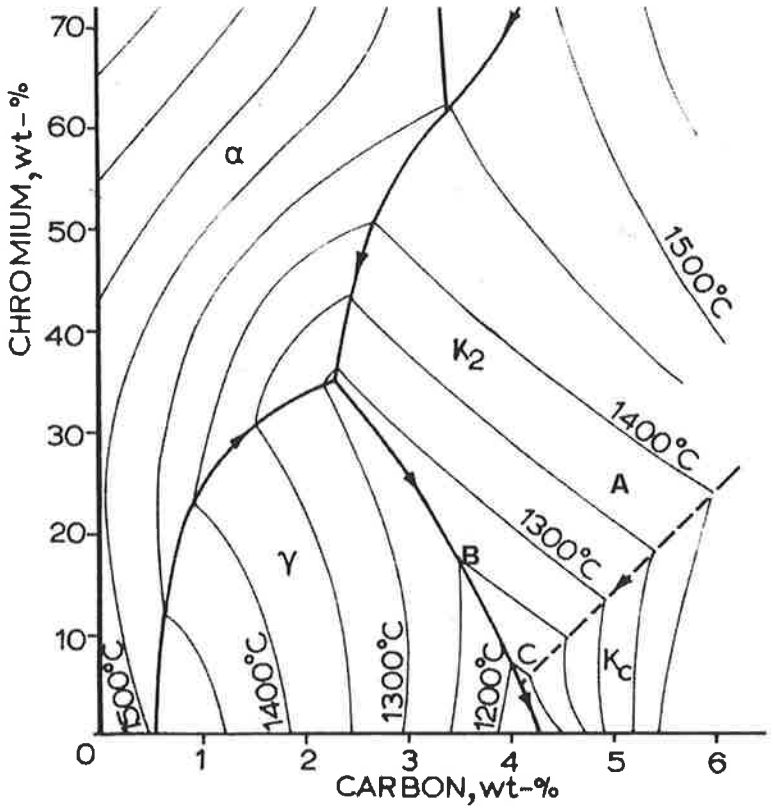

Figure 2.5: - The metastable Fe-Cr-C liquidus surface (after Jackson, 1970). K_c represents the $(Fe,Cr)_3C$ carbide and K_2 represents the $(Cr,Fe)_7C_3$ (or M_7C_3) carbide phase.

Many open-arc hardfacing consumables produce an all-weld-metal deposit with approximately 25 wt.% chromium and 5 wt.% carbon. A typical all-weld-metal composition is denoted "A" in Figure 2.5. The substrate is usually mild steel, containing

no chromium and approximately 0.1-0.2 wt.% carbon. For the purposes of this illustration the substrate can be considered to be at the origin in Figure 2.5. As an overlay is deposited, the weld pool is host to a mixing process between molten globules at the all-weld-metal composition (*i.e.* at "A") and molten substrate material (at the origin). The average composition of the bead will lie on the straight line between the origin and "A", with the exact point being determined by the dilution of that bead. "B" represents a point on the line "OA". If the dilution is high, the composition will fall to the left of "B" and a hypoeutectic microstructure will result. The microstructure will comprise primary dendrites of austenite (γ in Figure 2.5) in a eutectic mixture of austenite and carbide. The austenite may subsequently transform to martensite on cooling. A hypoeutectic microstructure is shown in Figure 2.6(a). If the composition falls on point "B" the microstructure will be entirely eutectic (Figure 2.6(b)). Finally, if the dilution is low, and the composition falls between "B" and "A", the microstructure will be hypereutectic, comprising needles of primary $(Cr,Fe)_7C_3$ carbide in a eutectic mixture of austenite (or martensite) and carbide. A hypereutectic microstructure is shown in Figure 2.6(c).

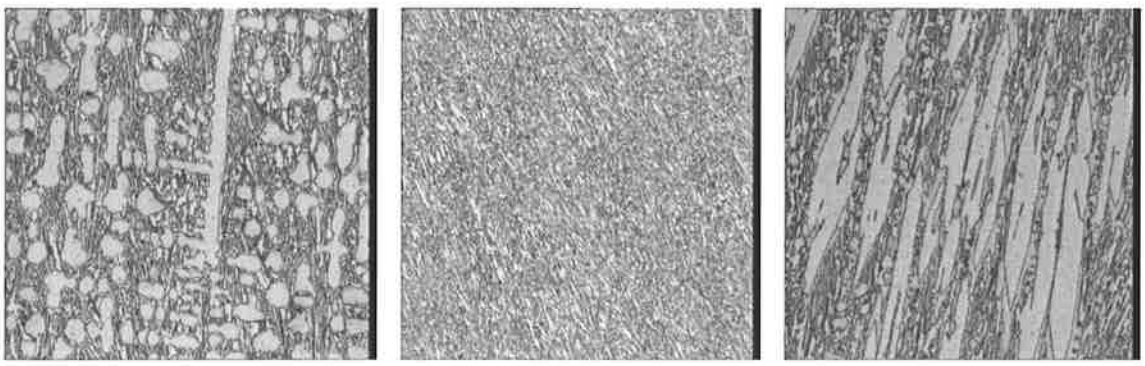

(a) **(b)** **(c)**

Figures 2.6: - Hypoeutectic (a), eutectic (b) and hypereutectic (c) microstructures respectively (after Francis and Jones, 1997).

If, at low levels of dilution, a welding consumable produces a hypereutectic deposit, it is generally referred to as a chromium-carbide-type consumable. These consumables are further classified according to the structure of the matrix constituent in the eutectic. The matrix is usually either austenite, martensite or a combination of the two. All of the welding consumables used in the current work were of the chromium-carbide-type.

Powell (1979) studied hardfacing weld deposits and observed that the primary carbides in hypereutectic deposits were hollow and hexagonal in cross-section. Thus they could appear as either needle-like rods or hexagonal platelets depending on the orientation of their axes relative to the plane of polish. Powell noted that the carbides were usually aligned parallel to the direction of heat flow, which is roughly perpendicular to the base plate. However, he also observed that carbides could nucleate and grow in non-uniform orientations from any undissolved particles of ferrochromium present in the deposit.

There is a microstructural variation in hypereutectic white irons, namely the complex regular structure (Powell *et al.*, 1997). Fast cooling rates, and the presence of either silicon or boron, promote undercooling and a change in carbide morphology from that in a normal hypereutectic deposit to that of an undercooled alloy (Powell *et al.*, 1994). Under these circumstances it is not possible to distinguish primary and eutectic carbides as the morphology is continuous (Powell *et al.*, 1994).

2.6 THE ABRASIVE WEAR OF HIGH-CHROMIUM WHITE IRONS

This section describes abrasive wear and some of the factors affecting the abrasive wear resistance of high-chromium white irons.

2.6.1 Definitions and Types of Abrasive Wear

Czichos (1978) gave the following description of abrasive wear:

"The effect of abrasion occurs in contact situations in which direct physical contact between two surfaces is given where one of the surfaces is considerably harder than the other. The harder surface asperities press into the softer surface with plastic flow of the softer surface occurring around the asperities from the harder surface. When a tangential motion is imposed the harder surface will move, ploughing and removing the softer material."

Abrasion is usually categorised by the type of contact, with the two categories being two-body and three-body abrasion. The former occurs when an abrasive slides along a surface and the latter when the abrading particles are caught between one surface and another (ASM Handbook, 1992).

Avery (1961) further categorised abrasion by describing three distinct types, namely scratching (or low-stress) abrasion, grinding (or high-stress) abrasion and gouging abrasion. Low-stress abrasion generally involves small abrasive particles, low stress levels and no impact. High-stress abrasion involves small to medium-sized abrasive particles, high stress levels, but no impact. Finally, gouging abrasion is associated with large abrasive particles, very high stress levels and impact.

The ASM Handbook (1992) gives a different description of the three categories of abrasion. Low-stress abrasion occurs when the abrasive remains relatively intact, an example being the sanding of wood with sandpaper. High-stress abrasion occurs when the abrasive particles are being crushed, such as in a ball mill where both the grinding

balls and ore are worn down. Finally, gouging abrasion exists when a relatively large abrasive cuts the material without full work hardening occurring, such as is the case where rocks are comminuted in a jaw-crusher.

2.6.2 The Relation Between Abrasive Wear Resistance and Hardness

It is known (Krushchov, 1957; Richardson, 1967; Moore, 1974) that there is a strong correlation between the apparent abrasive wear resistance of a material and its hardness, with a higher hardness resulting in better wear performance. Indeed, high-chromium white irons are widely used to combat abrasive wear due to the presence of hard $(Cr,Fe)_7C_3$ carbides in the microstructure (ASM Handbook, 1993b). It should be noted, however, that hardness does not always provide a reliable indication of the abrasive wear performance of a material, a fact that was well demonstrated by Cookson (1982). It is also known that abrasive wear resistance is not an intrinsic property of a material as it depends on the wear system (Czichos, 1977).

2.6.3 The Influence of Carbide Volume Fraction on Abrasive Wear Performance

Carbide volume fractions play an important role in determining the abrasion resistance of a white iron. Sare (1979), for example, reported that the low-stress abrasion resistance of white cast irons is principally controlled by the carbide volume fraction. There are two volume fractions used in the literature. The first will be referred to as the total carbide volume fraction *(TCVF)*, which embraces both eutectic and primary carbides. The second is the primary carbide volume fraction *(PCVF)*, which is relevant only for hypereutectic deposits. The *PCVF* distinguishes the large needle-like primary carbides from the finer eutectic carbides.

Rense *et al.* (1983) conducted one of the few studies that examined the relationship between the total carbide volume fraction and the abrasive wear performance of weld deposits. These workers performed dry-sand/rubber-wheel abrasion tests on their samples. (This test is considered to be representative of low-stress abrasion.) It was found that the abrasion resistance improved rapidly with increasing total carbide volume fraction and with increasing heat input. The correlation with heat input was thought to be related to the coarseness of the microstructure.

Yellup and Smoker (1995) performed pin-abrasion tests on their weld deposits using the method described by Muscara and Sinnott (1972). This test is considered to fall in the category of high-stress abrasion. Yellup and Smoker found that, for hypoeutectic deposits, the wear rate improved as the volume fraction of eutectic carbides increased. The improvement in wear performance was much greater, however, in hypereutctic deposits when the volume fraction of primary carbides was increased.

Zum Gahr and Eldis (1980) performed pin-abrasion tests on samples taken from high-chromium white iron castings. They cast thirteen different alloys with total carbide volume fractions ranging from 7 to 45%. When 150-mesh garnet was used as the abrasive, the wear rate decreased monotonically with increasing *TCVF*. However, when silicon carbide was used as the abrasive, higher carbide volume fractions produced higher wear rates. Zum Gahr and Eldis argued that higher carbide volume fractions lead to better abrasion resistance provided that the abrading particles are softer than the M_7C_3 carbides. This generally applies when garnet and quartz are the abradants. If, however, the abrading particles are harder than the M_7C_3 carbides, as is the case with silicon carbide particles, higher carbide volume fractions may result in little benefit or even a

reduction in abrasion resistance. It was argued that silicon carbide particles were able to penetrate and crack the M_7C_3 carbides, resulting in spalling of the sample. Zum Gahr and Eldis' data are plotted in Figure 2.7.

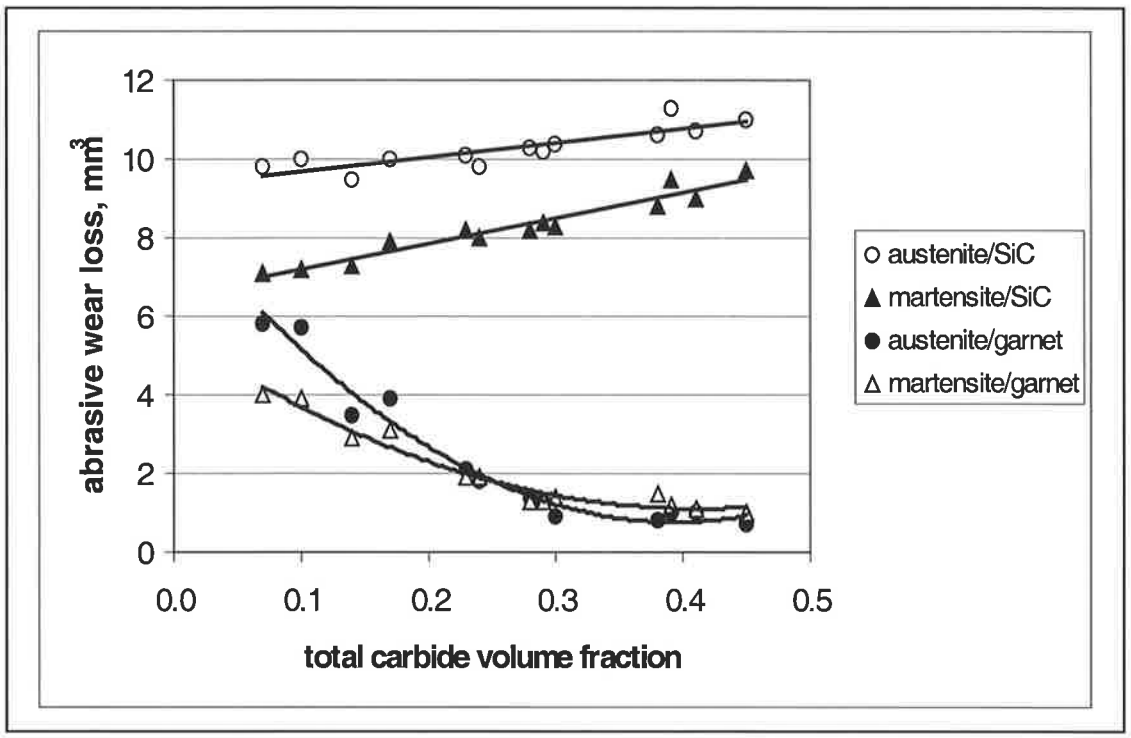

Figure 2.7: - Abrasive wear loss as a function of the total carbide volume fraction (after Zum Gahr and Eldis, 1980). The abrasive materials were 180-grit silicon carbide and 150-grit garnet. The matrices were either predominantly austenitic or predominantly martensitic.

According to Gundlach and Parks (1978), quartz and garnet are representative of the abrasives most commonly encountered in service in the minerals processing industry. It is expected, therefore, that high-chromium white irons with high carbide volume fractions will generally provide excellent resistance to low- and high-stress abrasion in many industrial applications. There are, however, instances in which high carbide volume fractions do not provide optimum wear resistance. Zum Gahr and Doane (1980) and Fulcher *et al.* (1983) provide examples in which the optimum wear performance is achieved at intermediate carbide volume fractions, near the eutectic composition. In

these cases the alloys with high carbide volume fractions wear at faster rates due to spalling of the primary carbide needles (Fulcher *et al.*, 1983). There are other factors that also play a role in determining the abrasion resistance of a material, such as the mean free path and the average distance between carbide particles (Sare, 1979). The orientation of the carbide needles has also been shown to be significant (Dogan and Hawk, 1995).

2.6.4 The Influence of Matrix Structure on Abrasive Wear Performance

Very few studies have specifically investigated the influence of matrix structure on the abrasive wear performance of hardfacing weld deposits. However, some workers have studied the role played by the matrix in white iron castings (Sare, 1979; Zum Gahr and Doane, 1980). These studies have found that the matrix plays an important role in supporting the M_7C_3 carbides, with the carbides being the dominant influence on the abrasion resistance of the alloy. Austenitic matrices were found to provide a higher fracture toughness and result in a higher resistance to spalling. Sare (1979) found that an austenitic matrix also led to improved abrasion resistance. Zum Gahr and Doane (1980), however, and Zum Gahr and Eldis (1980) found that martensitic matrices provided better resistance to abrasive wear and that, if only a moderate fracture toughness were required, martensitic matrices were the preferred choice.

2.6.5 Check Cracking in Hardfacing Overlays

Open-arc hardfacing involves the joining of two dissimilar materials. High-chromium white iron overlays have a different coefficient of thermal expansion to steels and, due to their limited ductility, usually develop check cracks (Farmer, 1974). It is generally believed in the Australian hardfacing industry that coarser check crack distributions,

which result when a high heat input is employed, are deleterious to wear performance (Gorman, 1997). Larger check cracks are believed to increase the likelihood of spalling. This belief has also emerged elsewhere, as evidenced by the filing of a patent covering the use of low heat input welding techniques as a method of achieving a fine check crack distribution (Ashida *et al.*, 1994). The patent covers heat inputs in the range 0.2 to 0.6 kJ/mm. There do not, however, appear to be any quantitative studies in the literature dealing specifically with the effects of check cracking on the abrasive wear performance of hardfacing overlays.

2.6.6 A Quantitative Approach to the Abrasive Wear of Composite Materials

Zum Gahr (1987) presented a quantitative approach to the abrasive wear of composite materials. He pointed out that wear resistance was known not to be a material property, since it depends on the characteristics of the wear system (Czichos, 1977). However, it was demonstrated that there are identifiable upper and lower limits for the abrasive wear rates of a composite if the wear rates of each constituent are known.

Zum Gahr considered a composite material to comprise a matrix phase and a reinforcing phase. The upper and lower bounds for wear rates are then obtained from linear and inverse rules of mixtures. For a given wear system, if the wear rates of the matrix phase and reinforcing phase are W_1 and W_2, then the wear resistances are W_1^{-1} and W_2^{-1} respectively. If both phases in the composite wear simultaneously then the wear resistance of the composite, W_c^{-1}, is given by the linear rule of mixtures, *i.e.*:

$$W_c^{-1} = \frac{1}{\frac{v_1}{W_1^{-1}} + \frac{v_2}{W_2^{-1}}} \quad \ldots\ldots\ldots \quad (2.13)$$

where v_1 and v_2 are the volume fractions of the matrix and reinforcing phases respectively. Conversely, if each phase wears sequentially the wear resistance of the composite material is described by an inverse rule of mixtures, *i.e.*:

$$W_c^{-1} = v_1 W_1^{-1} + v_2 W_2^{-1} \quad \ldots\ldots \quad (2.14)$$

Zum Gahr tested his own pin-abrasion data (described in Zum Gahr and Eldis (1980)), and observed that the wear rates fell between his predicted upper and lower limits. His results are represented graphically in Figure 2.8.

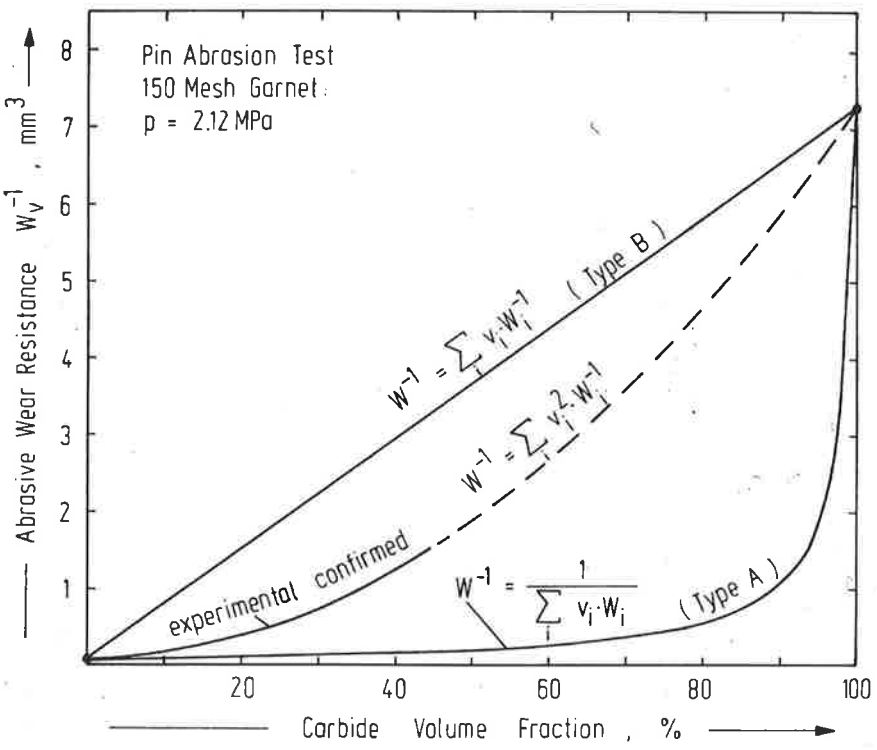

Figure 2.8: - A graphical representation of the upper and lower limits for abrasive wear of composite materials after Zum Gahr (1987). Type A systems involve simultaneous wear only, whereas Type B systems correspond to sequential wear. The intermediate curve corresponds to the data described in Zum Gahr and Eldis (1980). p is the contact pressure at the interface between the pin and the abrasive cloth.

2.7 THE RATIONALE FOR THE CURRENT WORK

There are many publications in the literature dealing with microstructure/wear relationships for high-chromium white irons. These works include two recent Ph.D theses (Stevenson, 1995; Tabrett, 1997), the first of which dealt with microstructures in hardfacing weld deposits. By comparison, few publications deal with the relationship between welding parameters and microstructure. Stevenson, in his conclusions and suggestions for further work, stated that the effect of welding parameters had not been studied. It was intended that the current work address this issue.

It was seen in section 2.2 that there are apparent discrepancies between the findings of various dilution studies but, with some analysis, it was possible to identify consistent trends. An interesting point arises, however, in that most of the published work relates to single-bead deposits. Unfortunately, many (if not most) hardfacing applications require complete surface coverage, *i.e.* a multi-pass overlay. It is not yet clear whether the trends observed in section 2.2 also apply to multi-pass overlays. This issue needs to be clarified and any differences between the two types of deposits need to be identified.

The prediction of parameters such as single-bead width, height and penetration is a necessary step in the development of welding procedures. It was seen in section 2.3 that there are many influences on these parameters and that the prediction of weld bead geometry is not a trivial task. All of the methods described in the literature are empirical approaches and, unfortunately, the resulting expressions are cumbersome. There is a great need to examine the possibility of first-principles analyses, as they may result in a unified approach to a wide range of materials and properties.

Very few workers have investigated the relationship between the microstructure of a weld deposit and its wear performance. There is a need to establish whether or not the trends that have been identified by Zum Gahr and other workers (see Zum Gahr and Eldis, 1980) for white iron castings also apply to weld deposits. The wear performance of weld deposits will ultimately dictate guidelines that may be developed for the deposition of optimum high-chromium white iron overlays.

3

GEOMETRY, DILUTION AND COMPOSITION OF SINGLE-BEAD DEPOSITS

3.1 INTRODUCTION

The first phase of experiments involved single-bead deposits. It was intended that these experiments would reveal the major influences on the geometry and composition of single beads. The chapter commences with a description of the experimental procedure, and each subsequent section focuses on the factors affecting a particular feature of the deposit. For single-bead deposits, the features of major interest are the bead width, penetration, height, dilution and composition. Throughout, down-hand deposition is used, as this is the preferred mode of operation in industry.

3.2 EXPERIMENTAL TECHNIQUE

Two welding consumables were used for the single-bead experiments. The first, consumable A, was a 2.4mm diameter chromium-carbide-type alloy-cored electrode. The second, consumable B, was also a chromium-carbide-type electrode, but 2.8mm in diameter. Both of these consumables were found to produce single-bead deposits with predominantly austenitic matrices. The approximate compositions of both consumables are listed in Table 3.1. The concentrations of carbon and sulphur were obtained from combustion carbon and sulphur analyses whereas the concentrations of all other elements were obtained using optical emission spectroscopy.

Consumable	*Cr*	*C*	*Mn*	*Ni*	*Si*	*B*	*S*	*Fe*
A	*25.1*	*6.55*	*1.2*	*0.3*	*0.6*	*0.2*	*0.02*	*bal.*
B	*26.7*	*5.93*	*0.4*	*0.2*	*0.9*	*-*	*0.02*	*bal.*

Table 3.1: - The approximate compositions of the consumables used in the current work. All concentrations are given in wt.%.

3.2.1 Experimental Program for Consumable A.

Sixty-four single beads 150mm long were deposited on to mild steel substrates 10mm thick, 200mm long and 50mm wide. In each case a 100mm long run-on plate was used. The power supply was a DC transformer-rectifier type with a 400 A capacity at 100% duty cycle. The power supply was connected to a wire feeder that fed the consumable through a water-cooled cable and gun. The gun was fixed and the steel plate sample was translated underneath it on a motorised X-Y table with a calibrated speed controller.

The experimental design comprised four travel speed settings, (150, 250, 350 and 450mm/min), four voltage settings (25, 28, 31 and 34V) and four current settings (250, 300, 350 and 400A). The work distance was 40mm and the polarity was direct-current, electrode-positive (DCEP). Although no information was provided regarding appropriate settings for travel speed, the welding currents and voltages were selected in such a way that they spanned the range recommended by the manufacturer.

The welding current and voltage were set on test pieces of steel prior to each experiment. Voltages were measured between the work piece and the contact tip, not at the wire feed unit. A CSIRO welding monitor (Dick, 1991) was used to display instantaneous values

for welding current and voltage and to log the data for each run. The monitor takes 5000 measurements of these parameters for each second of the welding run. It then averages these and displays one value per second of operation.

In addition, a further 8 single beads were deposited to investigate preheat temperatures to 300°C and work distances ranging between 30 and 60mm. Sixteen samples were also repeated using direct-current, electrode-negative (DCEN) polarity for comparison.

3.2.2 Experimental Program for Consumable B

Fifteen single beads 250mm long were deposited on to mild steel substrates 25mm thick, 50mm wide and 350mm long. Voltages ranged from 25 to 31V, currents from 200 to 400A and travel speeds from 400 to 800mm/min. In these experiments the work distances were also varied from 15 to 40mm. DCEP polarity was used in all cases.

3.2.3 Analysis of Samples for Consumable A

Three slices were cut from each sample. Each slice was approximately 10mm in thickness. One face of each slice was surface ground and etched with 5% Nital. The prepared section was then placed on an optical projector with a 10:1 magnification ratio and the bead profile was traced on to high quality tracing paper. This traced profile was then transferred to a digitiser pad where cross-sectional areas and hence dilutions were determined. Other parameters were also measured, including bead width, penetration and height.

3.2.4 Analysis of Samples for Consumable B

The height and width of each bead were measured using digital vernier callipers.

3.3 THE EFFECTS OF WELDING PARAMETERS ON BEAD WIDTH

3.3.1 A First-Principles Approach

The theoretical analysis of Christensen *et al.* (1965) proves to be a useful tool in estimating the width of a deposit. This work derived non-dimensional solutions for bead width and other parameters of interest in terms of a dimensionless operating parameter, n, given by:

$$n = \eta_a \frac{V_a I S}{4\pi\alpha' k' (T_c - T_o)} \quad \cdots\cdots\cdots (3.1)$$

where:

η_a = arc efficiency,
V_a = arc voltage,
I = welding current,
S = travel speed,
α' = thermal diffusivity of the base material,
k' = thermal conductivity of the base material,
T_c = chosen reference temperature, and
T_o = initial substrate temperature.

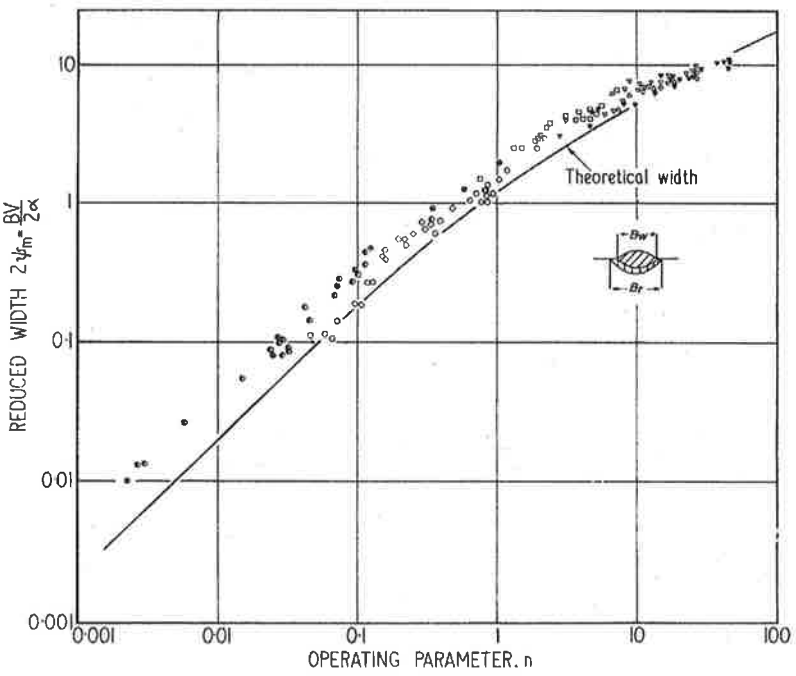

Figure 3.1: - The analytical solution for bead width proposed by Christensen *et al.* (1965).

The chosen reference temperature can be taken to be the melting point for the substrate material in order to predict the fusion line position and hence the bead width. If the thermal properties are assumed to remain constant then, for a given material, the value of n is determined by the arc voltage, current and travel speed.

Christensen's non-dimensional solution for bead width is a complicated and implicit function in n. However, although there were discrepancies, the solution was found to achieve reasonable agreement with experiment over a range of n values spanning four orders of magnitude. Open-arc hardfacing occurs over a much smaller range of n values. A lower limit for n in open-arc hardfacing may correspond to the condition where:

V_a = 24V,
I = 200A, and
S = 300mm/min.

An upper limit may correspond to:

V_a = 34V,
I = 400A, and
S = 900mm/min.

If the arc efficiency is assumed to remain relatively constant and representative thermal property values are available, it is possible to estimate the range of n values over which open-arc hardfacing occurs. The above-mentioned conditions would result in the lower limit for n being approximately 5 and the upper limit being approximately 50.

The form of Christensen's solution for bead width is:

$$\frac{w\,S}{2\,\alpha'} = F(n) \quad \cdots\cdots\cdots (3.2)$$

where w is the bead width and $F(\ )$ denotes a function.

If the substrate material is mild steel then, for the range of n values corresponding to open-arc hardfacing, equation 3.2 may be approximately represented by the following expression:

$$\frac{w\,S}{2\,\alpha'} = a_1 + a_2 n \quad \cdots\cdots\cdots \quad (3.3)$$

where a_1 and a_2 are constant coefficients.

Now, n is given by equation 3.1. For a given combination of substrate material and welding consumable the only variables that change are the arc voltage, V_a, current, I, and travel speed, S. Thus substituting equation 3.1 into 3.3 and combining constant terms provides the following expression for the bead width, with C_1 and C_2 being constants.

$$w = \frac{C_1}{S} + C_2 V_a I$$

Christensen's analysis suggests that it is the arc voltage, not the contact tip-to-work voltage, that is responsible for generating the heat that is transferred to the weld pool. In the case of the consumable electrode processes this may not be strictly correct. The voltage drop along the welding wire, between the contact tip and the arc, preheats the electrode and increases its enthalpy. This increased enthalpy is then added to the weld pool as the globules are transferred across the arc zone. Thus it would seem reasonable, for flux-cored arc welding, to use the contact tip-to-work voltage in place of the arc voltage, so that:

$$w = \frac{C_1}{S} + C_2 V I \cdots\cdots\cdots (3.4)$$

Even though the substitution of contact tip-to-work voltage for arc voltage seems reasonable, it is essentially an adjustment of convenience. The contact tip-to-work voltage is a much easier parameter to measure (and set) than the arc voltage. It is important to note, however, that adapting Christensen's solution to open-arc hardfacing is not likely to predict the resulting bead widths directly from first principles. The intention was to use their first-principles analysis as a starting point and adapt it to arrive at an expression that has an appropriate form.

The theory developed by Christensen *et al.* suggests that the values of C_1 and C_2 are dependent only on the thermal properties of the substrate material. However, in reality the deposition characteristics of the welding consumable will play a role, as they affect the deposition rate and hence the rate at which the enthalpy associated with metal transfer is added to the weld pool. Least-squares best-fit values for C_1 and C_2 were obtained for both consumables used in the current work. Figure 3.2 shows the measured bead widths plotted against fitted bead widths for consumable A. Figure 3.3 shows a similar fit for consumable B. It can be seen that good fits have been achieved for both welding consumables and that equation 3.4 appears to provide a form of expression suitable for describing bead widths for single beads-on-plate.

The agreement between fitted and measured bead widths appears to be good for all beads except those with widths greater than 20mm (see Figure 3.2). Thus one might expect equation 3.4 to accurately describe bead width data for beads produced under conditions that involve moderate-to-high travel speeds. These conditions generally result in a lower bead width, and a bead profile similar to that shown in Figure 3.4(a). Conversely, wide beads are produced under conditions where the deposition rates are

high and the travel speeds are low, and an example of such a condition is shown in Figure 3.4(b). As the weld pool rolls over unmelted substrate there will be heat transfer from the weld pool to the adjacent solid material. This heat transfer is likely to cause additional melting and result in the bead being wider than equation 3.4 might predict. Another issue also arises, however, in that the beads were deposited on 10mm thick substrates. It is therefore possible that, at low speeds and high heat inputs, there was appreciable bulk heating of the steel bars ahead of the welding arc. Such heating would also contribute to increases in bead width.

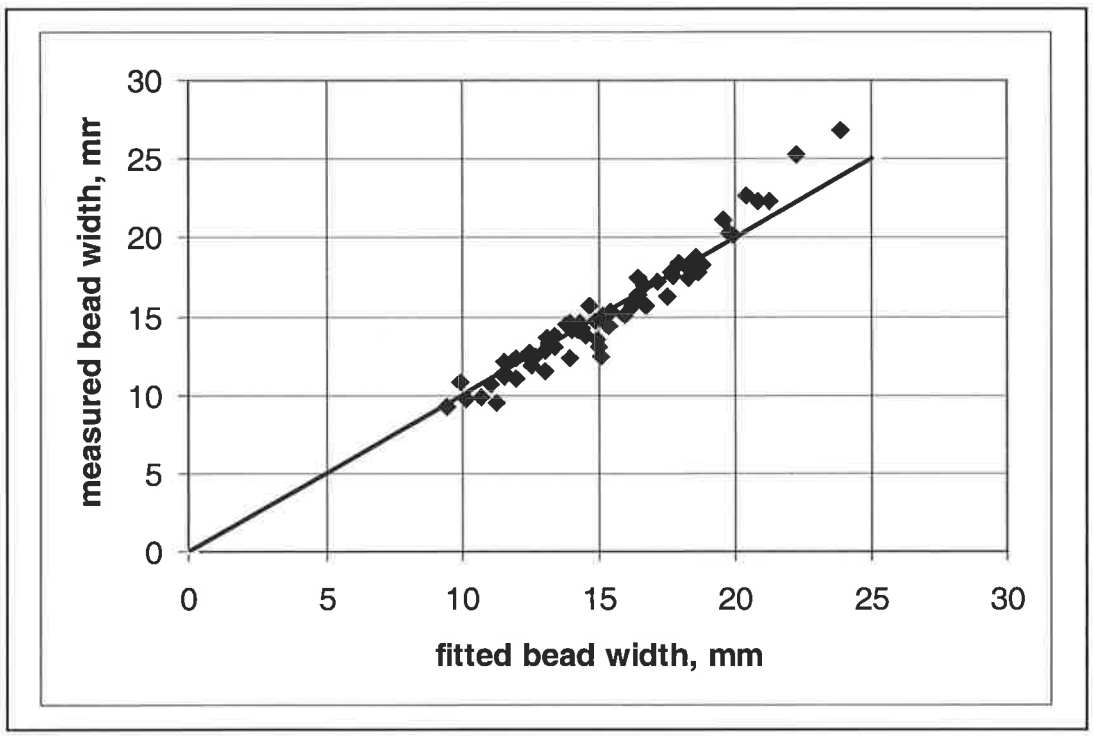

Figure 3.2: - Measured bead width vs the least-squares best fit to equation 3.4 for 64 samples deposited with consumable A (2.4mm diameter).

The form of equation 3.4 implies that the bead width will asymptote to a specific non-zero value as the travel speed is increased. However, this may not necessarily be the case. It must be remembered that equation 3.4 is a first order fit to Christensen's

solution over the range of n values encountered in open-arc hardfacing. It will, however, provide accurate predictions for most practical welding conditions.

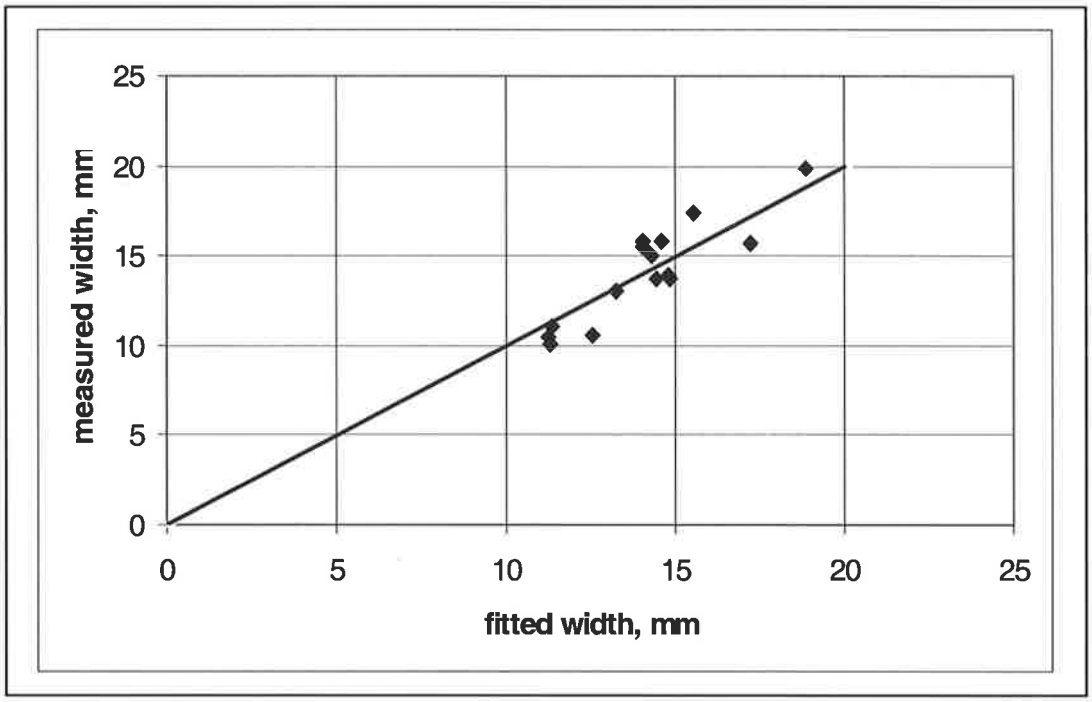

Figure 3.3: - Measured bead width vs the least-squares best fit to equation 3.4 for the 15 samples deposited with consumable B (2.8mm diameter).

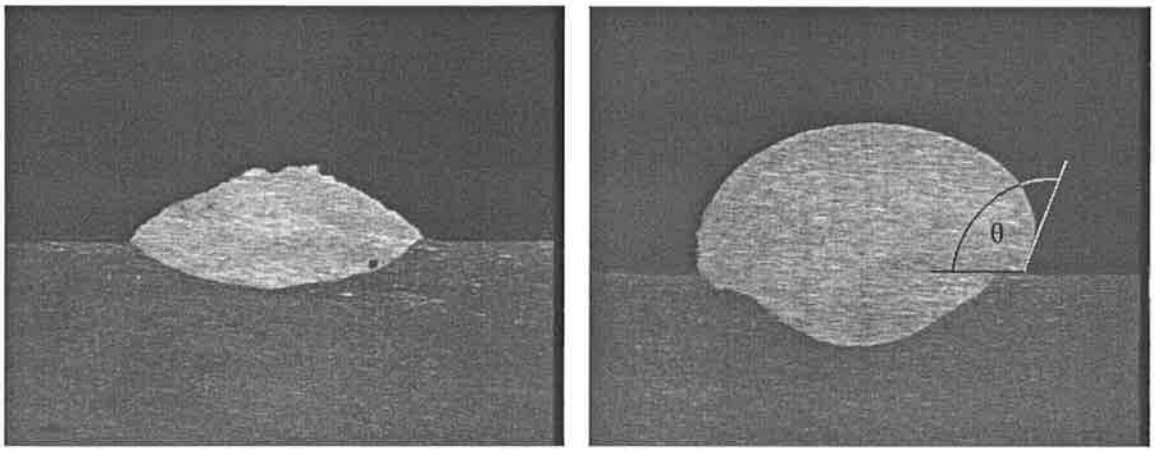

(a) 34V, 250A and 450mm/min (b) 28V, 350A and 250mm/min

Figures 3.4: - An example of the bead profiles that result at moderate-to-high travel speeds is shown in (a). If the deposition rate is high and the travel speed is low, a profile such as that shown in (b) will result. In this case there is a tendency for the weld pool to roll over unmelted substrate and the value of θ will be greater than 90°.

3.3.2 The Effects of Work Distance and Preheat Temperature

Equation 3.4 relates the bead width to the welding voltage, current and travel speed. However, the extent to which the work distance and preheat temperature affect the bead width is not revealed. The variation of bead width with work distance is plotted in Figure 3.5 and the variation with preheat temperature is plotted in Figure 3.6. It can be seen that the bead width is not particularly sensitive to work distance. Increasing the preheat temperature to 300°C does, however, lead to a somewhat greater quantity of substrate being melted and hence a slightly greater bead width.

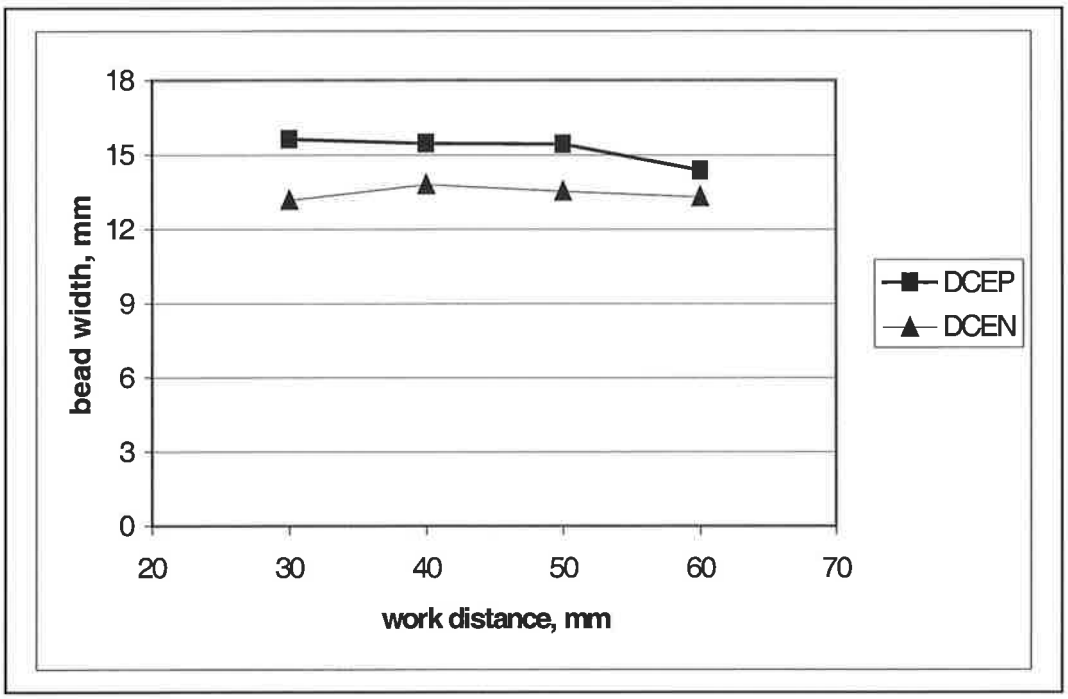

Figure 3.5: - The effect of work distance on the bead width. These samples were deposited with consumable A and the base welding conditions were 31V, 300A, 350mm/min with no preheat.

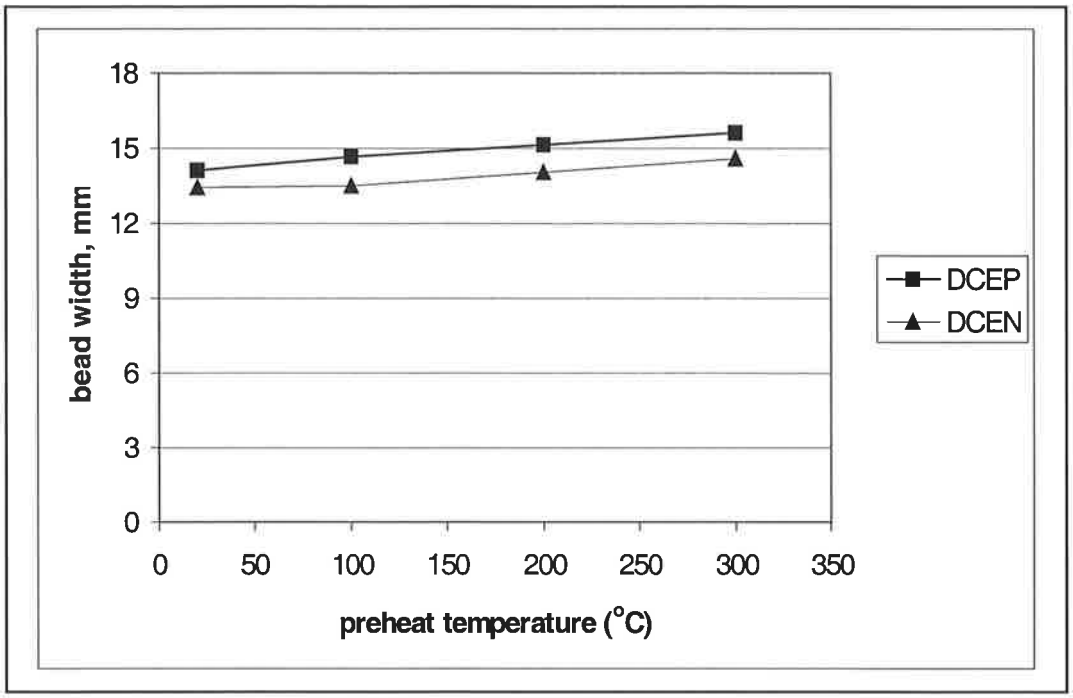

Figure 3.6: - The effect of preheat temperature on the bead width. These samples were deposited with consumable A and the base welding conditions were 31V, 300A, 350mm/min and a 40mm work distance.

3.4 THE EFFECTS OF WELDING PARAMETERS ON PENETRATION

3.4.1 Expressions for Penetration

It is possible to adapt Christensen's model and arrive at an expression for penetration in the same way as it was for bead width:

$$2p = \frac{C_1}{S} + C_2 V I \quad \cdots\cdots\cdots (3.5)$$

Christensen's model predicts that the fusion line will be a semi-circle in the case where a single bead is deposited on a thick plate. If the fusion lines of single-bead deposits were semi-circular, the values of C_1 and C_2 in equation 3.5 would be the same as the values

they assumed in equation 3.4 for bead width. The data for Consumable A have been fitted to equation 3.5 and are plotted in Figure 3.7. The measured data are plotted against values from the least-squares best fit.

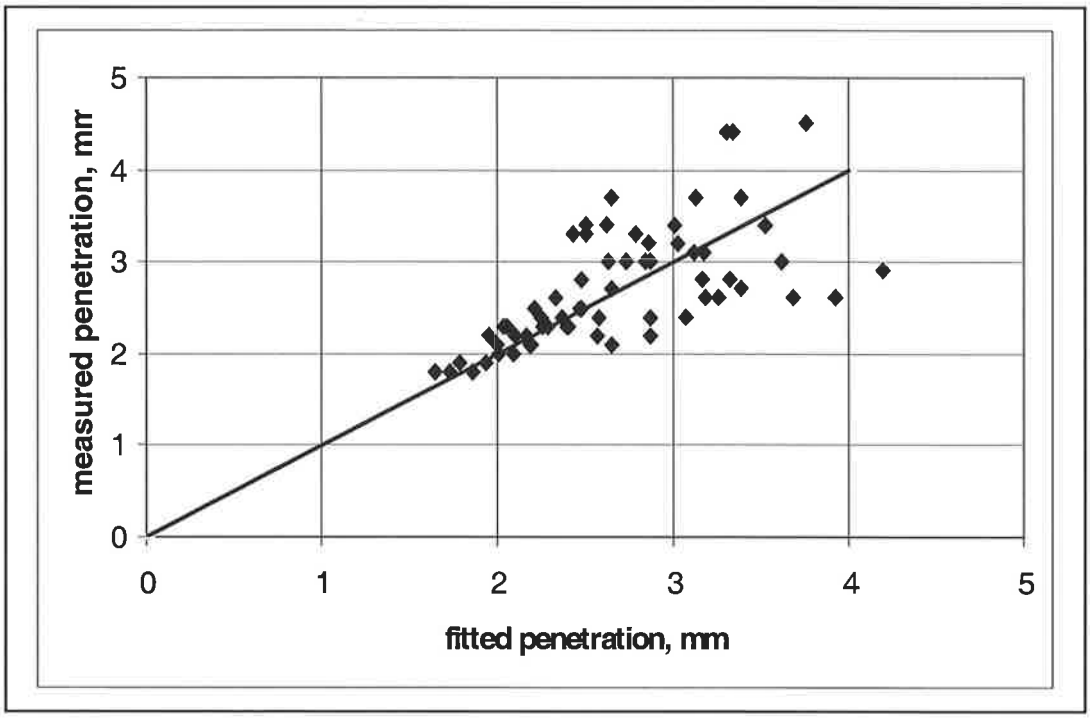

Figure 3.7: - Measured penetration against fitted penetration for consumable A (2.4mm diameter). The data are a least-squares best fit to equation 3.5.

It can be seen that the fit for penetration is poor. There are certain influences on penetration that are not accounted for by the Christensen model. It was seen in section 2.3 that weld pool convection, weld pool depression and the molten droplets play significant roles in determining the shape of the weld pool and hence the penetration. It appears from the plot that an adaption of Christensen's model will provide accurate predictions at low penetrations, but as the arc voltage and current rise the above-mentioned effects become increasingly significant. An empirical term was added to equation 3.5 in an attempt to improve the fit and account for these effects but this attempt met with limited success.

Jackson and Shrubsall (1953) used an empirical approach, attributed to Gunnert, for estimating weld bead penetrations (see section 2.3.6.1). They proposed that penetration data would take the following form:

$$p = K \sqrt[3]{\frac{I^4}{S V^2}} \quad \cdots\cdots\cdots (2.6) \quad \text{(page 22)}$$

where K is a fitted constant term.

Kim, Basu and Siores (1994) fitted their penetration data to an expression of the form:

$$p = 10^{a_1} d^{a_2} G^{a_3} I^{a_4} V^{a_5} \quad \cdots\cdots\cdots (3.6)$$

The data were obtained from gas-metal-arc weld deposits. In equation 3.6, d is the consumable diameter, G is the gas flow rate and a_1, a_2, a_3, a_4, a_5 are fitted constants. In open-arc hardfacing there is no gas flow rate as such, as the electrodes are self-shielding. The travel speed will also play a role in determining the weld bead penetration, but was not included in the expression. A more appropriate form of expression is:

$$p = b_1 V^{b_2} I^{b_3} S^{b_4} \quad \cdots\cdots\cdots (3.7)$$

where b_1, b_2, b_3, b_4 are fitted constants. The penetration data for consumable A were fitted to both expressions 2.6 and 3.7. The fit achieved with equation 3.7 (shown in Figure 3.8) was slightly better than that achieved with equation 2.6. It can be seen that the fit is also better than that achieved with the adapted form of Christensen's model, but that there is still significant spread. The fitted equation is:

$$p = 10^{-4.47} V^{-0.55} I^{0.81} S^{-0.30} \quad \cdots\cdots\cdots (3.8)$$

If the fit for equation 2.6 is expressed in the same form as equation 3.8 it becomes:

$$p = 10^{-5.66} V^{-0.67} I^{1.33} S^{-0.33} \quad \cdots\cdots\cdots (3.9)$$

There are similarities between equations 3.8 and 3.9. Both suggest welding current is the dominant influence on penetration. As the current increases so too does the penetration. Both equations also display close agreement regarding the sensitivity of penetration to arc voltage and travel speed. However, none of the above mentioned equations demonstrate an ability to describe penetration accurately. At best, equation 2.6 can be used as a guide to the relative sensitivities of penetration to each parameter. This equation achieved a fit that was comparable to those of equations 3.5 and 3.7, yet it only requires one constant value to be established. In addition, it has been found useful in estimating submerged-arc weld bead penetrations (Jackson and Shrubsall, 1953).

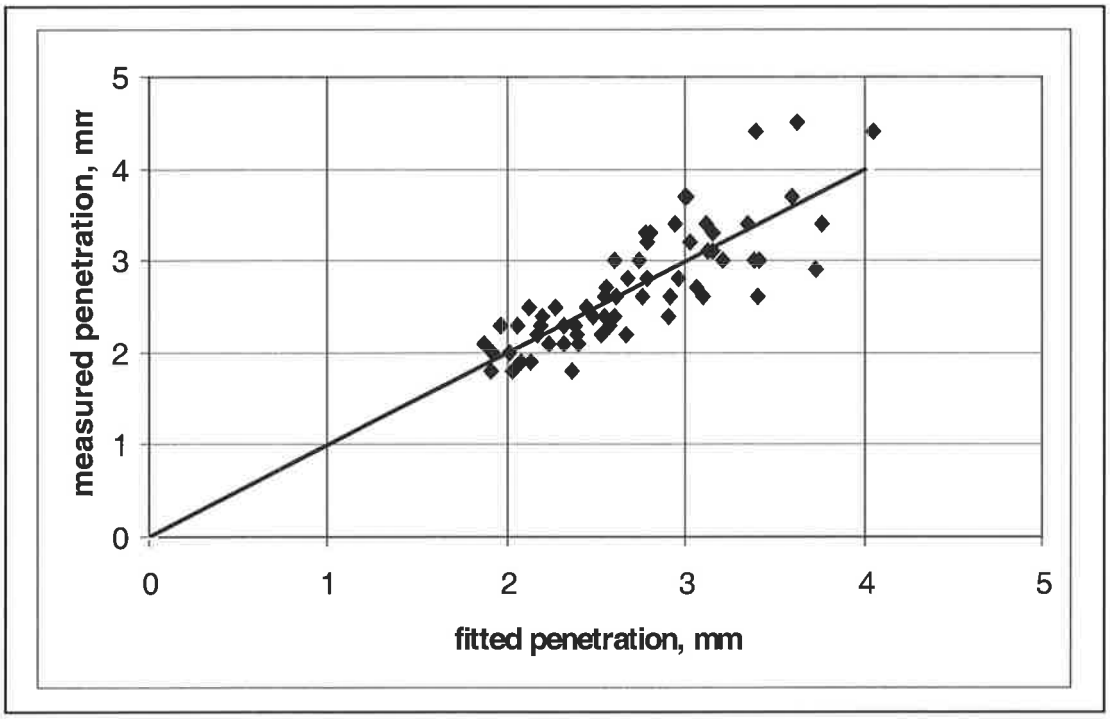

Figure 3.8: - Measured penetrations vs fitted penetrations for consumable A (2.4mm diameter). The fitted penetrations are a least-squares best fit to equation 3.7.

3.4.2 The Effects of Work Distance and Preheat Temperature

The effects of work distance and preheat temperature are shown in Figures 3.9 and 3.10 respectively. It can be seen that there is a significant drop in penetration as the work distance is increased. Kim and Na (1995) proposed that this effect is related to the increase in arc length that occurs when the work distance is increased. These workers suggested that longer arcs cause the distributions of heat, arc pressure and current flux to be expanded, resulting in less penetration. By comparison, there does not appear to be a clear trend in Figure 3.10. This is somewhat unexpected as one might anticipate a trend towards increasing penetration with increasing preheat temperature. As the preheat temperature increases, a greater amount of substrate material will melt. Figure 3.6 showed that increases in preheat temperatures resulted in wider beads, but it appears that higher preheat temperatures may be required before the effect on penetration becomes obvious.

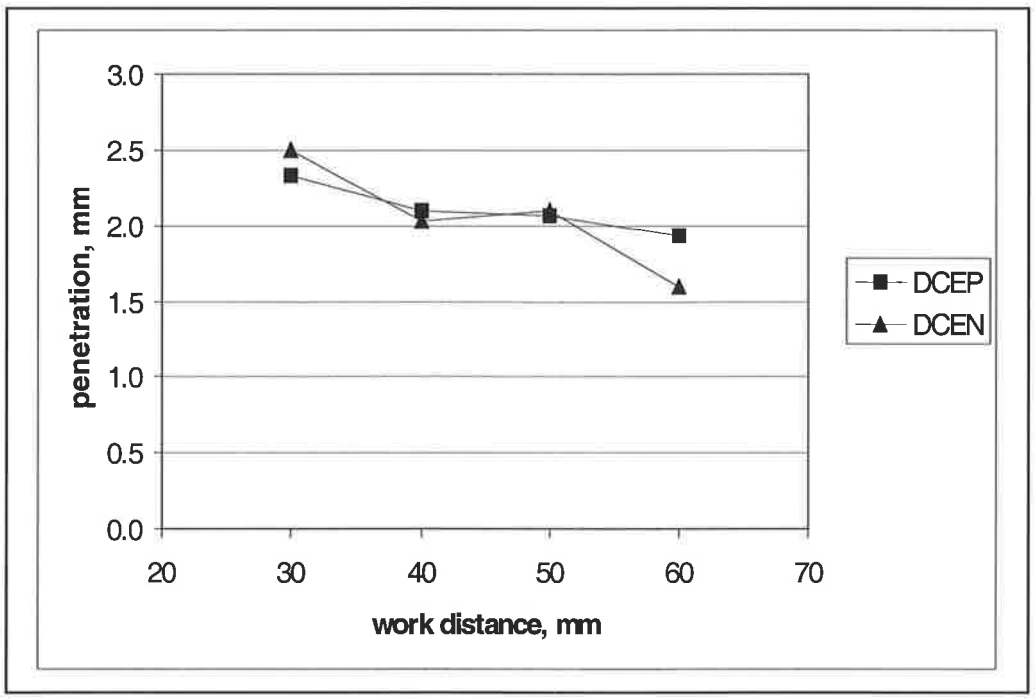

Figure 3.9: - The variation in penetration with work distance. All data points were obtained with consumable A and the base welding conditions were 31V, 300A, 350mm/min and no preheat.

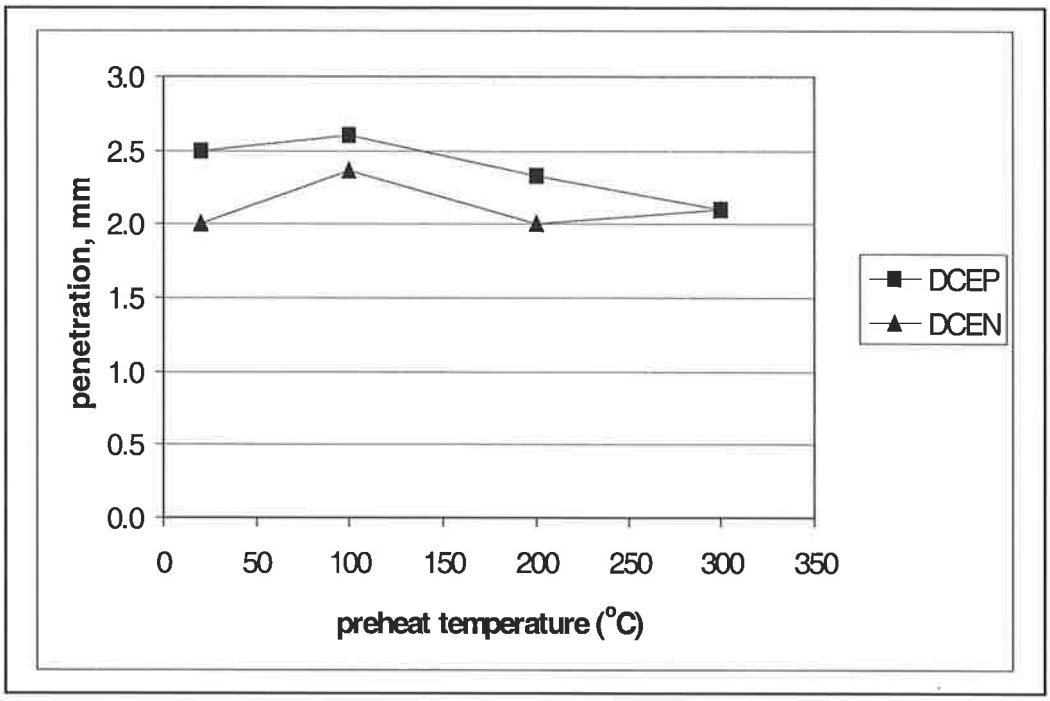

Figure 3.10: - The variation in penetration with preheat temperature. All data points were obtained with consumable A and the base welding conditions were 31V, 300A, 40mm, 350mm/min and no preheat.

3.5 BEAD HEIGHT

3.5.1 An Expression for Bead Height

It was seen in the literature review that little has been published regarding the prediction of bead height directly from the selected welding parameters. Consequently, an approach is outlined here. The approach is based on the assumption that the profile of a bead can be modelled by a parabolic function. This is a reasonable assumption, particularly at moderate-to-high welding speeds. An example of a bead profile that resembles a parabola was given in Figure 3.4(a), where the travel speed was 450mm/min. A schematic representation of the proposed model is given in Figure 3.11.

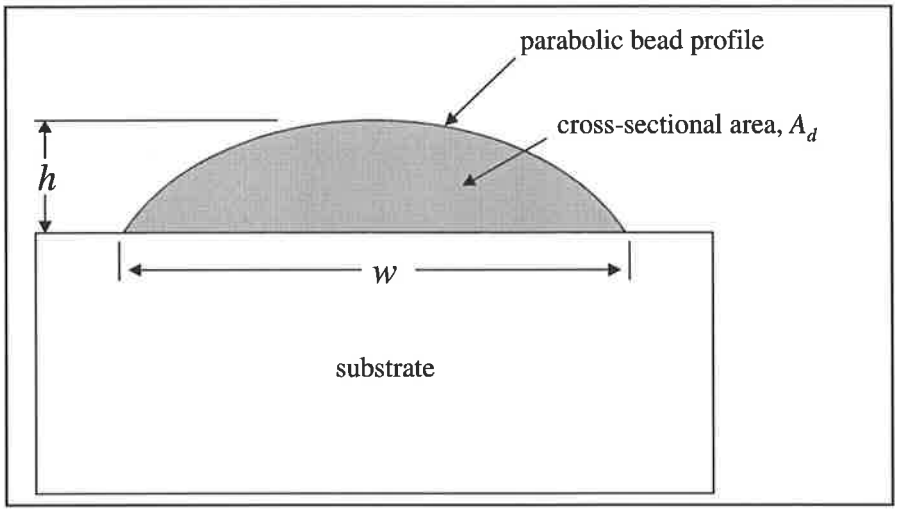

Figure 3.11: - A schematic representation of the parabolic model for a single-bead deposit.

The principle of conservation of mass requires that the area under the parabola is equal to the cross-sectional area of deposited material, A_d. It can be shown by integration that the area under the curve is equal to two thirds of the product of the width, w, and the height, h. It can also be shown that the cross-sectional area of deposited material is equal to the deposition rate divided by the product of density and travel speed, *i.e.*:

$$A_d = \frac{2}{3} hw = \frac{W}{\rho S} \quad \cdots \cdots \cdots \quad (3.10)$$

where h = the peak height of the parabolic function, (bead height)
w = the width of the parabolic function, (bead width)
W = deposition rate,
ρ = density of an all-weld-metal deposit, and
S = travel speed.

It is possible to obtain h explicitly from equation 3.10:

$$h = \frac{3}{2} \frac{W}{\rho S w} \quad \cdots \cdots \cdots \quad (3.11)$$

This expression for bead height is compared with data from three different welding consumables in Figure 3.12. (Data for the third welding consumable, consumable C, are reproduced by kind permission of Mr. B.K. Arnold of CSIRO Manufacturing Science and Technology. Consumable C was 2.8mm in diameter and had a similar composition to consumables A and B.) Values for w were obtained from measured bead widths and values for W were obtained from measured deposition rates.

It can be seen that if the predicted bead height is 4mm or less one can be confident that the prediction is accurate. This will most likely be the case if the welding condition involves a moderate-to-high travel speed. However, as the height of the beads increases so too do the discrepancies and, if the predicted bead height is greater than 4mm, the error may be large. Large errors are particularly likely if the deposition rate is high and the travel speed is low.

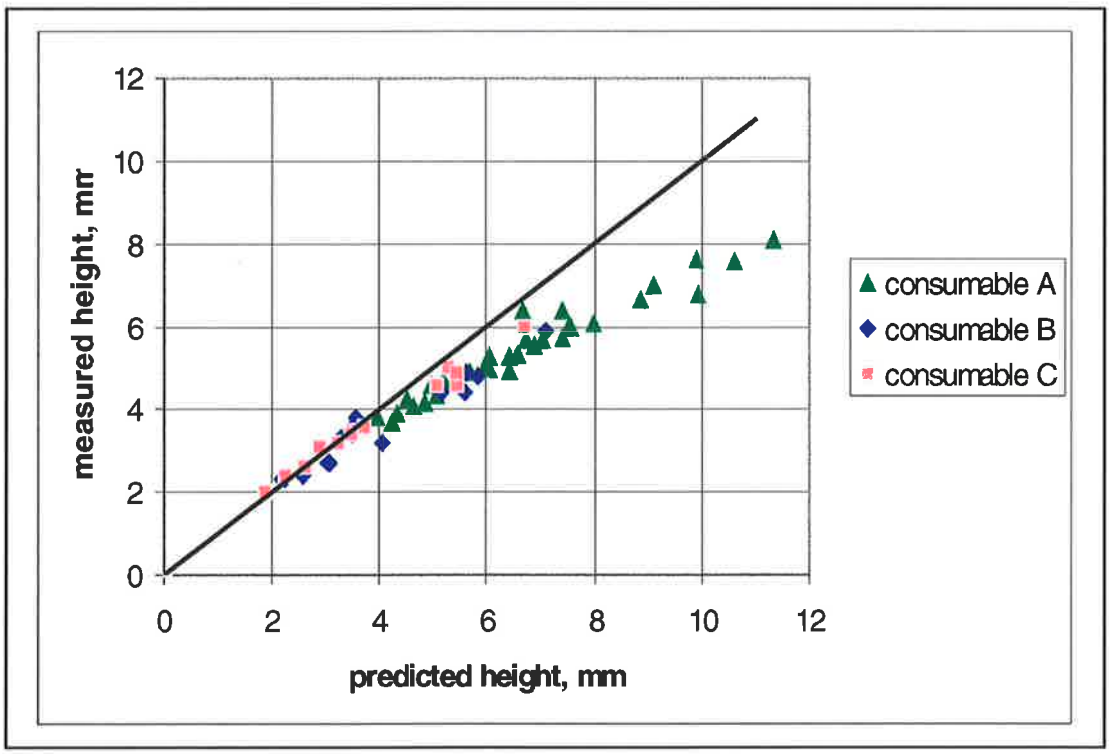

Figure 3.12: - A plot of measured heights for three different welding consumables against the height predicted by equation 3.11. All samples were deposited with DCEP polarity.

The discrepancies between equation 3.11 and measured values are caused by gravity-induced flow of the weld pool. Such flow has occurred in the case of the weld bead shown in Figure 3.4(b). It can be seen that in this case the weld pool has, to some extent, flowed over unmelted substrate. The bead profile deviates significantly from a parabolic profile when gravity-induced flow occurs and consequently the predictions made by equation 3.11 become increasingly inaccurate. Gravity-induced flow occurs to a greater extent as the height of the weld pool increases.

Fortunately, there is a strong correlation between the heights predicted by equation 3.11 and those measured in practice. The nature of the correlation is such that equation 3.11 is amenable to an empirical correction that accounts for this gravity-induced flow. An empirical correction has been included in equation 3.12:

$$h = \frac{3}{2}\frac{W}{\rho S w} - 84.4\left(\frac{3}{2}\frac{W}{\rho S w}\right)^{2.25} \qquad \{h \leq 8 \times 10^{-3}\ \mathrm{m}\} \quad \cdots\cdots (3.12)$$

The height measurements from the three different welding consumables are plotted against the fitted values for equation 3.12 in Figure 3.13.

Equation 3.12 is likely to accurately predict the bead height for many high chromium, high carbon type deposits, as their tendency to flow will be similar. Different consumable types are also likely to fit to an expression of the same form as equation 3.12. However, it is anticipated that the constant and index in the empirical correction term will change as the tendency to flow changes from material to material.

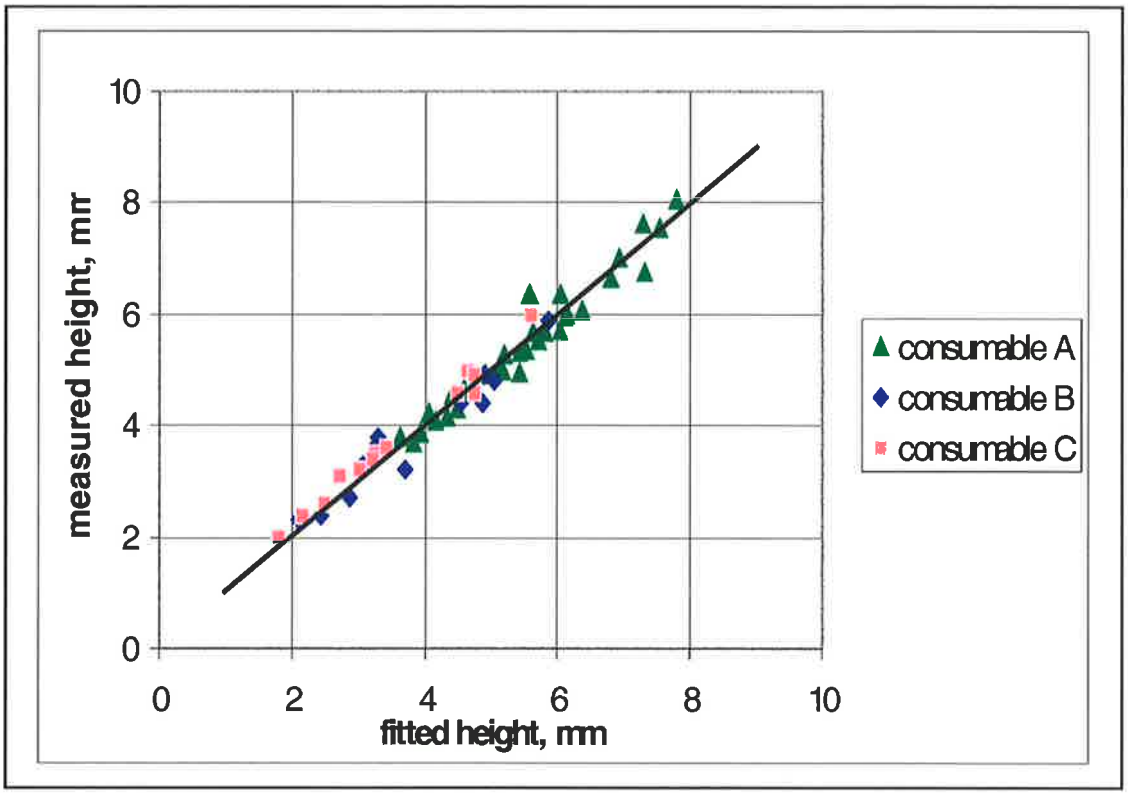

Figure 3.13: - Measured height vs fitted height with the empirical correction in equation 3.12. All samples were deposited with DCEP polarity.

3.5.2 The Effects of Work Distance and Preheat Temperature

The effects of work distance and preheat temperature on bead height are shown in Figures 3.14 and 3.15 respectively. The effect of work distance can be explained by the increase in deposition rate associated with increasing the work distance (see equation 2.4 – page 12). If all other parameters remain constant, the higher deposition rate will result in a higher bead. The effect of preheat temperature can be explained in terms of the associated increase in bead width. As the bead width increases the amount of deposited material has to be distributed across a wider bead, and a reduction in bead height will result.

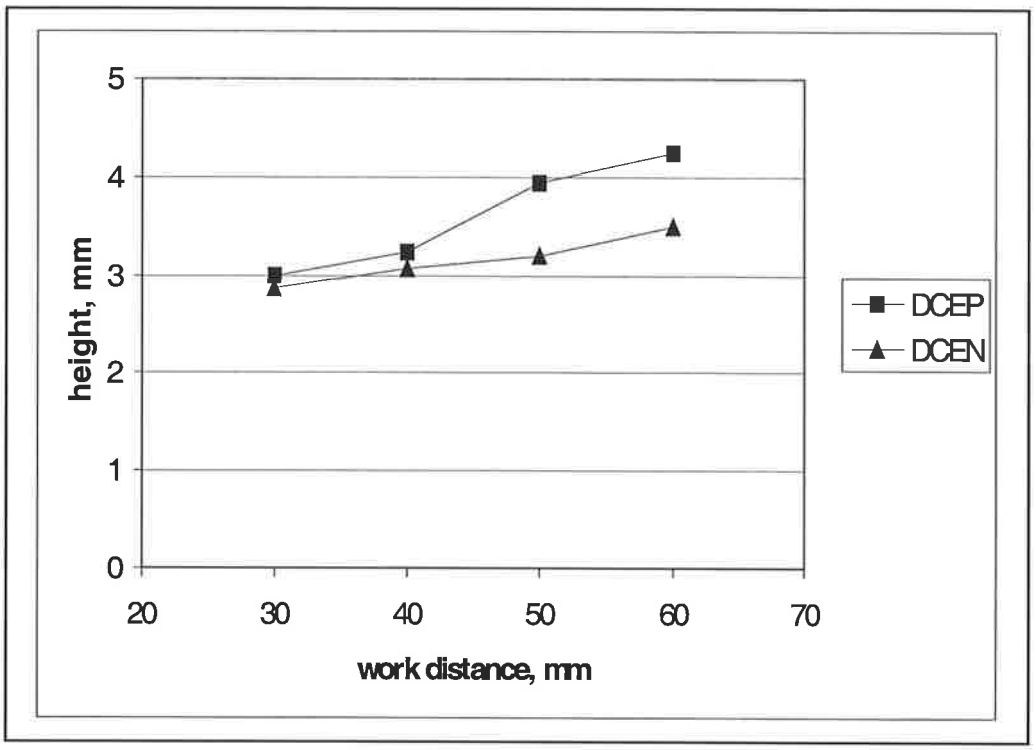

Figure 3.14: - The variation in bead height with work distance. All data points were obtained with consumable A. The base welding conditions were 31V, 300A, 350mm/min and no preheat.

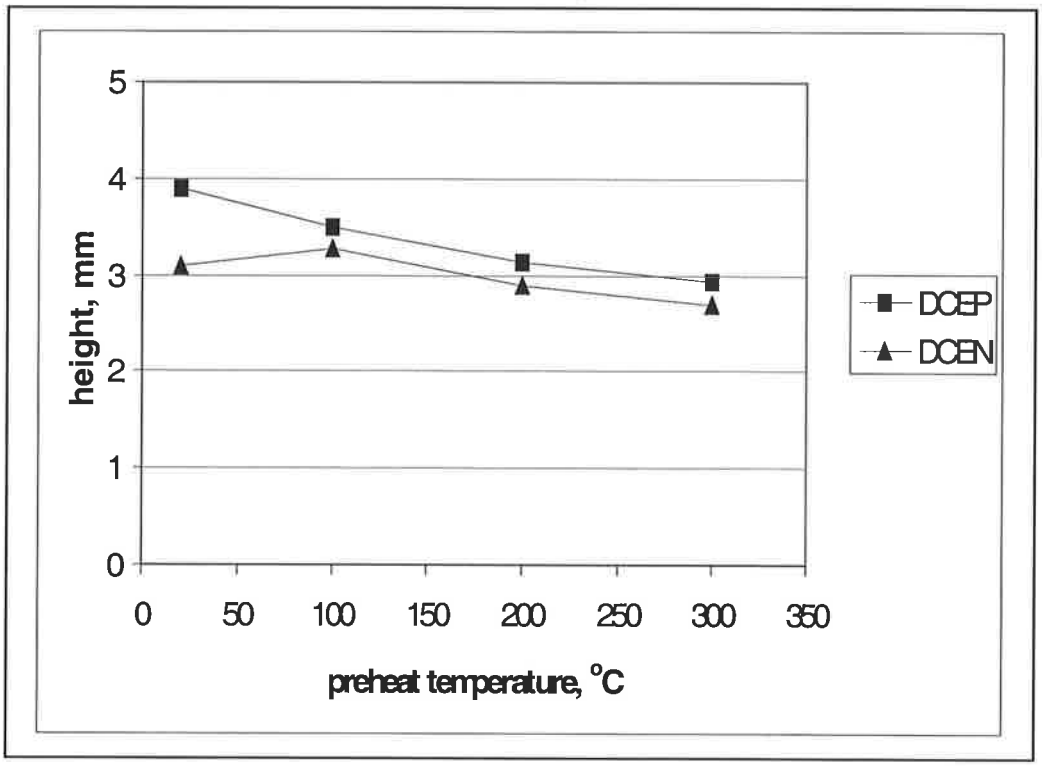

Figure 3.15: - The variation in bead height with preheat temperature. All data points were obtained with consumable A. The base welding conditions were 31V, 300A, 350mm/min and a 40mm work distance.

3.6 DILUTION OF SINGLE-BEAD DEPOSITS

3.6.1 The Bednarz-Deam Model (see Francis *et al.*,1998)

There have been few studies that investigate the effects of welding parameters on the dilution of single-bead deposits. A first-principles approach initiated by Deam (1996) and extended by Bednarz (1996) was discussed in Section 2.2.3. The model resulted in a general expression for the dilution of a single-bead deposit:

$$\frac{D_{sb}}{1-D_{sb}} = \alpha \frac{VI}{W}\left(1+\beta V I S\right) \quad \cdots\cdots\cdots (2.2) \qquad \text{(page 10)}$$

where D_{sb} is the dilution of a single-bead deposit and α and β are constant terms depending on the combination of welding consumable and substrate. Deposition rate data were measured for thirty-two samples deposited with consumable A and, for these samples, the dilution data have been fitted to the Bednarz-Deam model and are plotted in Figure 3.16. Measured values are plotted against fitted values.

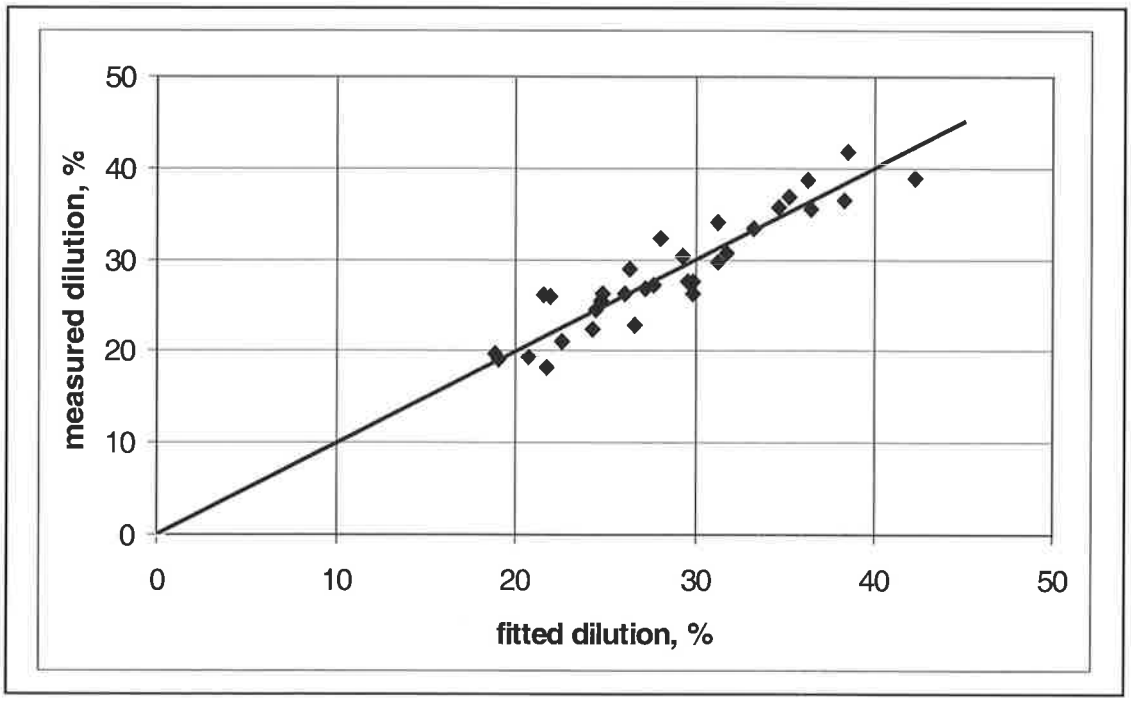

Figure 3.16: - Measured dilution data plotted against fitted values from the Bednarz-Deam model for single-bead dilution. The data were obtained from 32 single beads deposited with consumable A.

The model can be seen to describe the data with acceptable accuracy. An expression similar to equation 2.2 can be derived using equation 3.4 for bead width and equation 3.10 for the cross-sectional area of deposited material in a single-bead deposit. Christensen's model predicts that the fusion line for a single-bead deposit will be a semi-circle.

Thus, the cross-sectional area of melted substrate is:

$$A_{s(sb)} = \frac{1}{2} \times \frac{\pi w^2}{4} = \frac{\pi}{8}\left(\frac{C_1}{S} + C_2 VI\right)^2 \quad \cdots\cdots\cdots (3.14)$$

The cross-sectional area of deposited material is given by:

$$A_d = \frac{W}{\rho S} \quad (\textit{from equation } 3.10)$$

If the area of melted substrate, $A_{s(sb)}$, is divided by the area of deposited material, A_d, it can be shown that:

$$\frac{D_{sb}}{1 - D_{sb}} = b_1 \frac{VI}{W}\left(\frac{b_2}{VIS} + 1 + b_3 VIS\right) \quad \cdots\cdots\cdots (3.15)$$

where b_1, b_2 and b_3 are constant terms relating to the particular combination of substrate and welding consumable. The derivation of equation 3.15 from equation 3.4 for bead width confirms that the Bednarz-Deam model and equation 3.4 are generally consistent with each other.

The single-bead dilution data shown in Figure 3.16 were fitted to equation 3.15. The fit did not improve, however, with the inclusion of the extra parameter.

3.6.2 The Effects of Work Distance and Preheat Temperature

The effects of work distance and preheat temperature on single-bead dilution are shown in Figures 3.17 and 3.18 respectively.

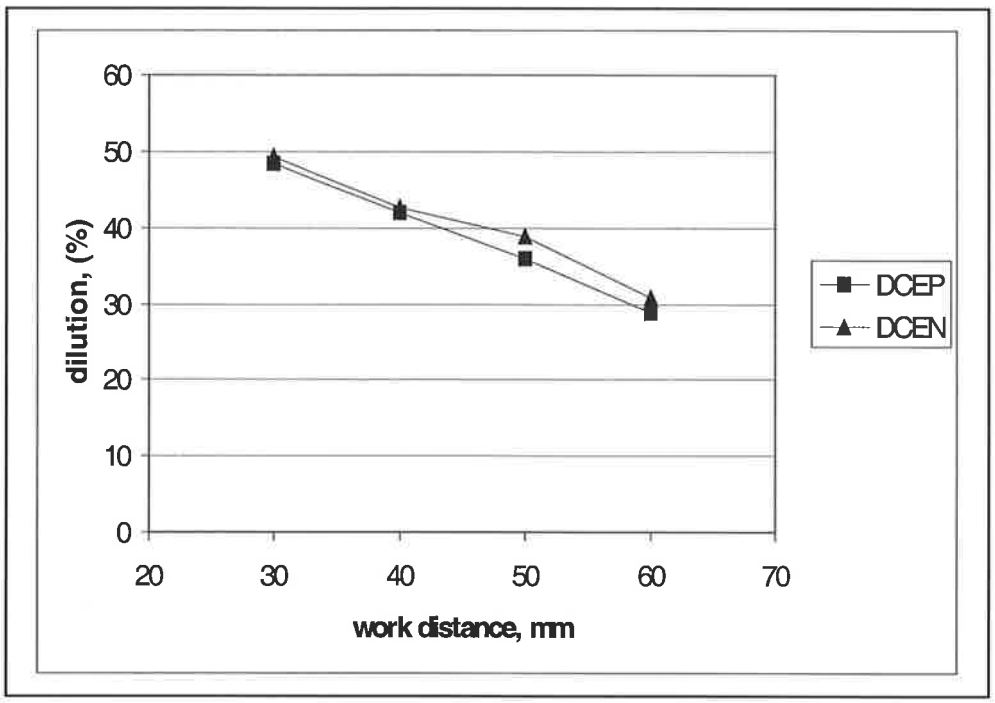

Figure 3.17: - The variation in single-bead dilution with work distance. All data points were obtained with consumable A. The base welding conditions were 31V, 300A, 350mm/min and no preheat.

Increases in work distance result in lower dilutions due to an increase in the deposition rate. However, Thorpe (1980) pointed out that the reduction in arc voltage associated with increasing the work distance may also contribute to reduced dilution. The reduction in arc voltage is caused by an increase in the voltage drop along the electrode between the contact tip and the arc. Increases in preheat temperature raise the dilution through increased melting of substrate material. Figure 3.18 shows, however, that the effect of preheat temperature is small for temperatures below 300°C.

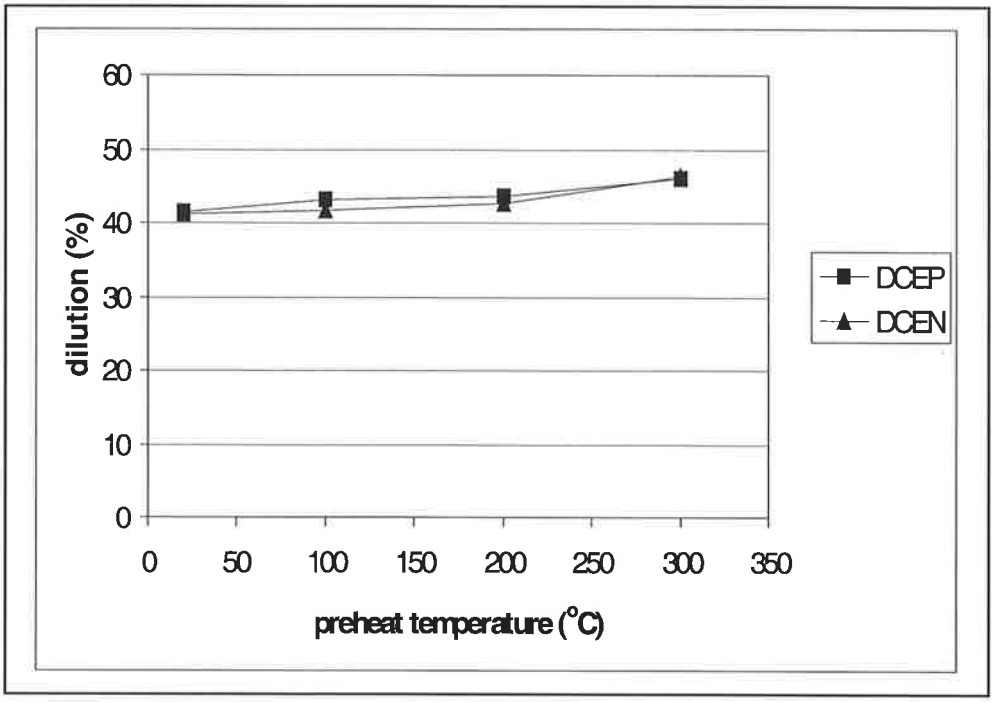

Figure 3.18: - The variation in single-bead dilution with preheat temperature. All data points were obtained with consumable A. The base welding conditions were 31V, 300A, 350mm/min and a 40mm work distance.

3.7 COMPOSITION OF SINGLE-BEAD DEPOSITS

If all of the welding consumable material that was melted was subsequently deposited as weld metal, the composition of a weld bead could be readily estimated from knowledge of the consumable composition and the dilution. Material is lost, however, in the process of welding through vaporisation, flux losses and other events such as spatter. That is to say, the *deposition efficiency* is less than 100%. The deposition efficiency, η_d, is defined as:

$$\eta_d = \frac{mass\ of\ weld\ metal\ deposited}{mass\ of\ welding\ consumable\ melted} \times 100\% \quad \cdots\cdots\cdots (3.16)$$

The deposition efficiencies calculated for consumables A and B are summarised in Table 3.2.

Consumable	Number of measurements	Mean deposition efficiency (%)	Standard Deviation (%)
A	56	95.1	3.8
B	15	97.6	1.4

Table 3.2: - A summary of the results of deposition efficiency measurements.

Given that the measured deposition efficiencies are high one might expect that it is possible to estimate the weld bead composition from the dilution and consumable composition. In order to test this hypothesis, combustion carbon and sulphur analyses were performed on eight weld beads deposited with consumable A. The beads were selected in such a way that they spanned a wide range of welding conditions and dilutions. The measured carbon concentrations were then compared with those predicted by assuming 100% deposition efficiency. The results are shown in Figure 3.19.

It can be seen that the predicted carbon concentrations are higher than the measured values. It is possible that this may be due to a disproportionate loss of carbon as the molten globules travel across the arc zone. An investigation of the factors leading to and affecting element loss is beyond the scope of this work. Consequently, the all-weld-metal composition will be used as a basis for all predictions of overlay composition.

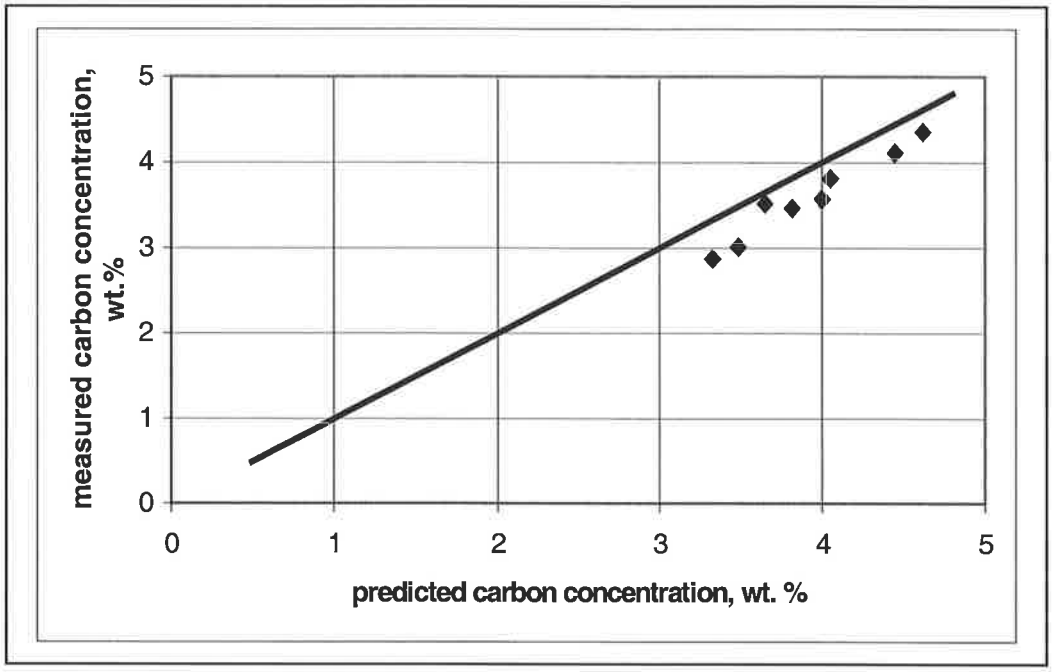

Figure 3.19: - A comparison of measured carbon concentrations for samples deposited with consumable A with those predicted by assuming 100% deposition efficiency.

3.8 CONCLUSIONS

A first-principles expression for bead width was developed. This expression suggests that the bead width increases with increasing welding current and welding voltage and decreases with increasing welding speed. These findings are consistent with those of the previous studies outlined in section 2.3.6.2. Equation 3.4 for the bead width was also found to be consistent with the Bednarz-Deam model for single-bead dilution.

An expression for predicting the height of single beads was also developed. It was based on the assumption that the profile of a single-bead deposit is a parabola. This assumption resulted in accurate predictions of bead height for low beads but, as the height of the beads increased, the predictions became increasingly inaccurate due to gravity-induced flow of the weld pool. However, the correlation between the predicted

bead heights and the measured values was strong and, with an empirical correction term, accurate predictions of bead height can be achieved.

Further work is required to develop a working expression for predicting the penetration of a single-bead deposit. However, the prediction of single-bead penetration is generally not essential in hardfacing operations. It is usually only necessary to predict the area of substrate that is melted in order to estimate the dilution. The first-principles model developed by Bednarz and Deam (see Francis *et al.*, 1998) was found to describe the single-bead dilution data in the current work with sufficient accuracy.

The deposition efficiencies of high chromium, high carbon welding consumables appear to fall in the range of 95 – 98 %, in agreement with the values quoted in the manufacturers' data sheets. The achievement of consistently high deposition efficiencies facilitates the prediction of deposition rate directly from the wire feed rate as set prior to welding. It should be mentioned that there are two methods of controlling deposition rate that find widespread use in the Australian hardfacing industry. The first, and most widely used, is to maintain constant settings for the welding current and work distance. Equation 2.4 (page 12) suggests that, under these circumstances, the deposition rate will remain constant. However, as a contact tip wears, the point at which electrical contact is made (between the tip and the welding consumable) may change. Thus wear of the contact tip may result in an effective change in work distance and hence a change in deposition rate. A more reliable method for controlling the deposition rate is to select and set the correct wire feed rate, accounting for the deposition efficiency. This approach is made easier if the deposition efficiencies are consistent and high.

4

ABRASIVE WEAR RESISTANCE OF HIGH-CHROMIUM WHITE IRONS

4.1 INTRODUCTION

The previous chapter dealt with the factors affecting the geometry, dilution and composition of single-bead deposits. This chapter addresses the relationship between composition, microstructure and the abrasive wear performance of high-chromium white irons. Initial attention is given to methods of predicting the volume fraction of carbides in the deposit. The relationship between carbide volume fraction and hardness is then investigated. Finally, the results of pin-abrasion tests are analysed together with other published data.

4.2 VOLUME FRACTIONS OF CARBIDES

The two major constituents present in the microstructure of iron-chromium-carbon alloys are the matrix constituent and the carbide phase. The matrix constituent is usually martensite or austenite or a combination of both. The structure of the matrix is one feature that affects the wear performance of these materials. Another very important feature is the proportion of the carbide phase present in the deposit.

4.2.1 Estimating the Total Carbide Volume Fraction

Maratray and Usseglio-Nanot (1970) studied high-chromium white iron castings and developed an empirical expression for estimating the total carbide volume fraction, *TCVF*:

$$TCVF \quad (\%) \; = 12.33[C] + 0.55[Cr] - 15.2 \quad \cdots\cdots\cdots\cdots (4.1)$$

where $[C]$ and $[Cr]$ are the concentrations in wt.% of carbon and chromium respectively. This expression does not distinguish between primary and eutectic carbides. Maratray's expression was obtained from a least-squares best fit to data obtained from forty-two different alloys. It produces acceptable estimates over a range of compositions that embraces many practical applications.

4.2.2 An Alternative Approach for Estimating the Total Carbide Volume Fraction

It may be possible to develop an alternative approach for estimating the total volume fraction of carbides in a high-chromium white iron. This possibility arises due to the fact that both eutectic and primary carbides are of the M_7C_3 type (Maratray and Usseglio-Nanot, 1970), where M denotes an atom that may be either iron or chromium. The first step is to estimate the total carbide mass fraction, *TCMF*, using the expression:

$$TCMF \quad = \frac{[C] - [C]_m}{8.7 - [C]_m} \quad \cdots\cdots\cdots (4.2)$$

where $[C]$ is the concentration of carbon in the alloy (in wt.%) and $[C]_m$ is the average carbon concentration in the matrix constituent. The value "8.7" represents an average

value of the carbon concentration in M_7C_3 carbides. This value was calculated assuming that the M comprised 3.5 iron atoms and 3.5 chromium atoms. In reality the composition of M_7C_3 carbides can vary between $(Fe_5,Cr_2)C_3$ and $(Fe_2,Cr_5)C_3$ depending on the chromium-to-carbon ratio in the alloy (Maratray and Usseglio-Nanot, 1970). However, the concentration by weight of carbon in M_7C_3 carbides will not deviate significantly from this calculated value of "8.7%", due to the small difference in the atomic weights of iron and chromium.

Equation 4.2 is an interpolation between the carbon concentrations of the carbide and matrix constituents, giving the mass fraction of carbide in the material. In order to calculate the total carbide volume fraction, *TCVF*, it is necessary to convert the mass fraction into a volume fraction. This is achieved using the expression:

$$TCVF = \frac{TCMF}{TCMF + \frac{\rho_c}{\rho_m}(1 - TCMF)} \quad \cdots\cdots\cdots (4.3)$$

where ρ_c and ρ_m are the densities of the carbide phase and the matrix constituent respectively. A typical value for the ratio of ρ_c to ρ_m would be 0.9 (Maratray and Usseglio-Nanot, 1970).

Table 4.1 lists the predicted total carbide volume fractions according to both Maratray's formula and the above procedure for five different compositions. The five different compositions correspond to those that might be achieved with the same welding consumable but different levels of dilution. The welding consumable is assumed to have a chromium-to-carbon ratio of 5:1 and a total carbon concentration of 5 wt.%.

In calculating the carbide volume fractions in Table 4.1 the carbon concentrations in the matrix constituent were assumed to be 1% by weight. This value was taken to be representative, and was based on the work of Powell and Laird (1992) on high-chromium white iron castings.

Hypothetical Compositions		Predicted Total Carbide Volume Fractions	
Cr (wt.%)	C (wt.%)	Maratray and Usseglio-Nanot	Equations 4.2 and 4.3
12.5	2.5	22.5	21.2
15.0	3.0	30.0	28.1
17.5	3.5	37.6	34.9
20.0	4.0	45.1	41.6
22.5	4.5	52.7	48.2

Table 4.1: - A comparison between carbide volume fractions predicted by Maratray and Usseglio-Nanot (1970) and those predicted by equations 4.2 and 4.3. The matrix carbon concentration was assumed to be 1% by weight.

The major limitation with the above procedure is the unknown carbon concentration in the matrix constituent. Data published by Powell and Laird (1992) showed that, for the cast alloys studied, the matrix constituent was supersaturated with carbon. Cooling rates in hardfacing weld deposits are significantly faster than $0.3Ks^{-1}$; the fastest cooling rate investigated by Powell and Laird. Thus one would also expect the matrix constituent in hardfacing weld deposits to be supersaturated in carbon. Under these circumstances, the equilibrium Fe-Cr-C phase diagram described by Rivlin (1984) is unlikely to provide accurate predictions of matrix carbon concentration.

Another issue arises in that many welding consumables contain small amounts of silicon and boron. Silicon has been shown to reduce matrix carbon concentrations and increase the carbide volume fractions of white iron castings during solid-state cooling (Laird and Powell, 1993). It has been proposed that silicon and boron play a similar role in determining the carbon concentration in the matrix constituent of hardfacing weld deposits (Powell *et al.*, 1997).

Despite the complexity in predicting matrix carbon concentrations, it can be seen that the potential exists to develop an alternative approach to that of Maratray and Usseglio-Nanot, and that such an approach may be more effective in general.

4.2.3 Estimating Primary Carbide Volume Fractions

In some instances the volume fraction of primary carbides is of greater interest than the total volume fraction of carbides. Thorpe (1980) used the lever rule and metastable Fe-Cr-C liquidus surface proposed by Jackson (1970) to estimate the primary carbide volume fractions in his weld deposits, and he pointed out that it is necessary to account for the different density of the carbide phase. The volume fractions measured by Thorpe, however, did not agree with his predictions; results which were not entirely unexpected. While the liquidus surface proposed by Jackson (1970) has emerged as a useful tool in predicting weld deposit microstructures (de Sairre Balsamo *et al.*, 1995), it gives no indication of the changes in matrix chemistry that may occur during solid-state cooling. Such changes may be significant, particularly if silicon is present (Laird and Powell, 1993), and they may affect both the total and primary carbide volume fractions. It should be noted, however, that any changes that may occur during solid-state cooling will not affect whether the structure is hypoeutectic, near eutectic or hypereutectic, and

they do not necessarily detract from the usefulness of Jackson's diagram in predicting deposit microstructure.

Another obstacle associated with estimating the volume fraction of primary carbides is the possibility of forming a complex regular structure (Powell *et al.,* 1997). Fast cooling rates, and the presence of either silicon or boron, promote undercooling and a change in carbide morphology from that in a normal hypereutectic deposit to that of an undercooled alloy (Powell *et al.*, 1994). Under these circumstances it would be difficult, or impossible, to distinguish primary and eutectic carbides as the morphology is continuous (Powell *et al.*, 1994). This is a relatively recent development and may explain why the volume fractions of primary carbides measured by Thorpe did not agree with his predictions.

The variations that occur in the microstructure of hypereutectic deposits are illustrated in Figures 4.1 to 4.3. All of these photographs were taken from the same section of the same sample, which was deposited with consumable A (see section 3.2). A conventional hypereutectic microstructure is shown in Figure 4.1. As observed by Powell (1979), the primary carbide needles are hollow and hexagonal in cross-section. Thus a primary carbide needle may appear as either a needle or a hollow hexagon depending on the orientation of its axis relative to the plane of polish. An example of a complex regular structure is shown in Figure 4.2. When the carbides are viewed in cross-section, it can be seen that they exist in clusters that exhibit three-fold rotational symmetry, and that the size of the carbides is intermediate between primary and eutectic carbides (see Figure 4.1). Powell *et al.* (1994) also showed that, in a casting, the carbides were interlinked.

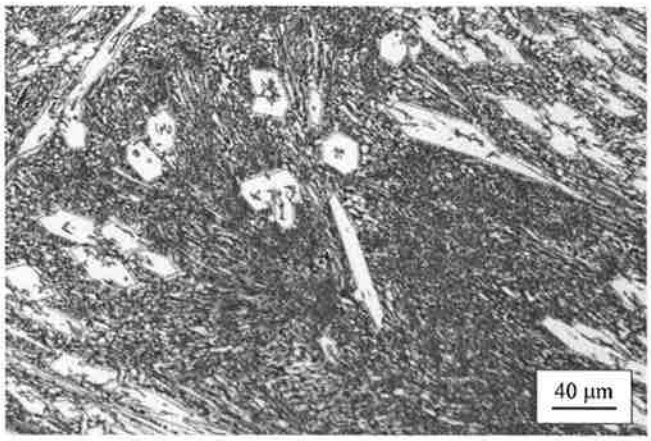

Figure 4.1: - A conventional hypereutectic microstructure. The primary carbides appear as either needles or hollow hexagons.

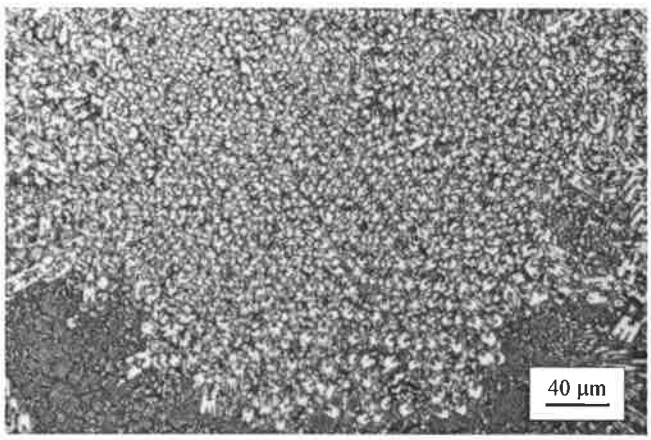

Figure 4.2: - A complex regular microstructure. The carbides appear in clusters exhibiting three-fold rotational symmetry.

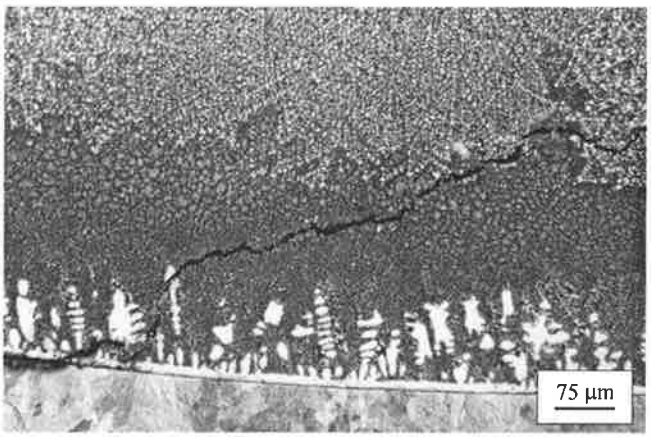

Figure 4.3: - The existence of an unmixed zone. Dendrites of austenite are present near the fusion line despite the bulk microstructure being hypereutectic. A check crack is also present, following the fusion line before deviating into the weld metal.

The complex regular structure was described by Elliot (1983a) as regular over small areas. Elliot (1983b) also pointed out that the structure was most frequently observed in hypereutectic alloys. Finally, Figure 4.3 shows the existence of an unmixed zone, as described by Baeslack and Savage (1979). There are dendrites of austenite near the fusion line despite the composite zone microstructure (see Figure 2.4 – page 26) being hypereutectic. Figure 4.3 also shows a check crack that follows the fusion line before deviating into the weld metal.

4.3 HARDNESS

Tarasov *et al.* (1975) presented an equation for predicting the hardness of high-chromium white iron weld deposits in terms of the proportions of each phase present. These workers proposed that the hardness of a composite material, HD_{com}, is given by:

$$HD_{com} = a_1[TCVF\ (HD_c)b_1 + (1 - TCVF\ )HD_m] \quad \cdots\cdots\cdots (4.4)$$

where a_1 is a coefficient taking dimensionality into account, *TCVF* is the total carbide volume fraction, HD_c is the hardness of the carbide phase, HD_m is the hardness of the matrix constituent and b_1 is a coefficient allowing for the anisotropy of the carbide.

In order to test the applicability of equation 4.4, hardness testing was performed on 32 of the single-bead samples that were deposited with consumable A. The Vickers test was employed using a 30kg load. Three measurements were performed on each sample in an attempt to reduce the level of scatter. In addition, the microhardnesses of the predominantly austenitic matrices and the carbide phase were measured and the results are summarised in Table 4.2. The fineness of the microstructure precluded the

determination of total carbide volume fractions. For each sample, the *TCVF* was estimated from the consumable composition, the measured dilutions and equation 4.1. Finally, the results were plotted against Tarasov's equation in Figure 4.4.

Measurement No.	Austenite (HV 0.01)	Carbide (HV 0.025)	
		a	c
1	405	1301	1234
2	377	1486	1328
3	374	1285	1011
4	392	1277	1017
5	398	991	1201
Average	**389**	**1268**	**1158**

Table 4.2: - A summary of the results of microhardness measurements. The column denoted "a" contains carbide hardnesses measured on a plane that is perpendicular to the long axis of the carbide. The column denoted "c" contains values measured on a plane that is parallel to the long axis. The average hardness of the carbides was assumed to be the arithmetic mean of these values.

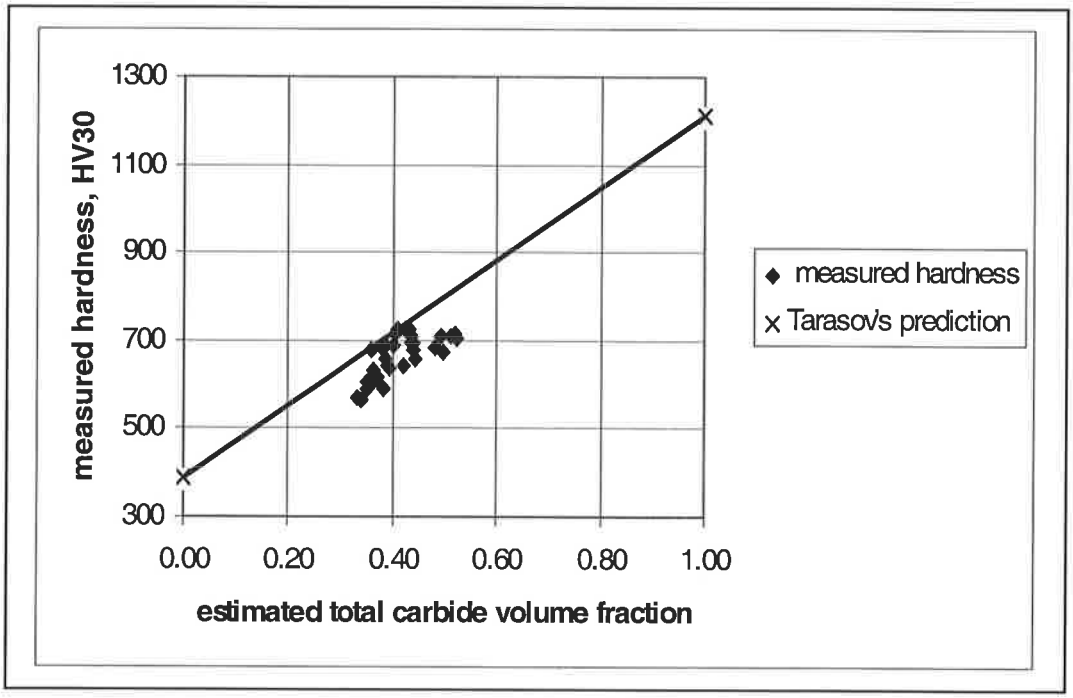

Figure 4.4: - Vickers hardness vs estimated total carbide volume fraction for 32 single-bead samples deposited with consumable A (see section 3.2).

There is considerable scatter in Figure 4.4 which may be attributed, in part, to the anisotropy of the carbides, their random orientations and locations. The data were also examined to establish whether there is a correlation between hardness and heat input, but such a correlation did not emerge. The results in Figure 4.4 suggest that Tarasov's equation overestimates the composite hardness and that hardness may be a non-linear function of carbide volume fraction. However, any conclusions should be drawn cautiously since the carbide volume fractions are estimated values and, furthermore, the estimates were based on the composition of the welding consumable, not the all-weld-metal composition. As was seen in section 3.7, this approach may overestimate the carbon concentration and hence the total carbide volume fraction.

4.4 PIN-ABRASION TESTING

The 32 samples that were selected for hardness testing were also prepared for micro-examination. Each sample was examined and 8 of the 32 were selected for pin-abrasion testing. The pins were selected in such a way that there were 2 hypoeutectic samples, 3 near-eutectic and 3 hypereutectic.

4.4.1 Experimental Technique (Muscara and Sinnot, 1972)

A test pin 6.35mm in diameter was simultaneously rotated about its axis and moved back and forth in a non-overlapping pattern over fresh 120-grit-garnet abrasive cloth under a dead load of 67N. The travel speed was 2540mm/min and the rotation proceeded at 40rpm. The pin was subjected to 29 traverses (approximately 12.9 metres). It was then removed and replaced by a mild steel reference pin which covered the remaining five traverses. After removal, both pins were washed in alcohol in an ultrasonic cleaner, rinsed, hot-air dried and weighed. This procedure was repeated five

times to obtain the average weight loss for one pin. The weight loss for the test pin was then referred to the weight loss for the reference pin.

4.4.2 Results

The results of the pin wear tests are plotted in Figure 4.5 against the carbon concentration in the deposit. The carbon concentrations were obtained using combustion carbon analyses (see section 3.7). The data are marked in the legend as the 2.4mm series.

Mr. B.K. Arnold of CSIRO Manufacturing Science and Technology has kindly permitted the use of his data. Mr. Arnold had prepared 16 pins including 8 from single beads deposited with a 1.6mm diameter consumable, and 8 from single beads deposited with a 2.8mm diameter consumable. Both of these consumables were austenitic high chromium, high carbon type wires. Combustion carbon analyses were also performed on all 16 of these single-bead deposits.

It can be seen that the results obtained from all three welding consumables are consistent with one another. The welding consumables had chromium-to-carbon ratios ranging between 4:1 and 5:1. The eutectic carbon concentration for chromium-to-carbon ratios in this range is approximately 3.5 wt.% according to the metastable Fe-Cr-C liquidus surface of Jackson (1970). The results indicate that hypereutectic deposits (*i.e.* those above 3.5 wt.% carbon) offer the best wear resistance. Furthermore, increasing the carbon concentration (and hence the volume fraction of primary carbides) in hypereutectic deposits will improve the abrasive wear resistance.

It is interesting to note that there appears to be no significant difference in the wear performance of strongly hypoeutectic deposits and those of near-eutectic composition. The data suggest there may be no significant penalty, in this particular test, for increasing the dilution if the deposit is already eutectic or hypoeutectic. Diesburg and Borik (1974) studied white cast irons and found that, as the solidification rate increases, the eutectic carbide structure becomes finer, and this refinement reduces the abrasion resistance of the material. One might expect this effect to be more pronounced in weld deposits where the cooling rates are generally faster than in castings. Rense *et al.* (1983) have conducted one of the few studies investigating the abrasion resistance of weld deposits. Their data are shown in Figure 4.6.

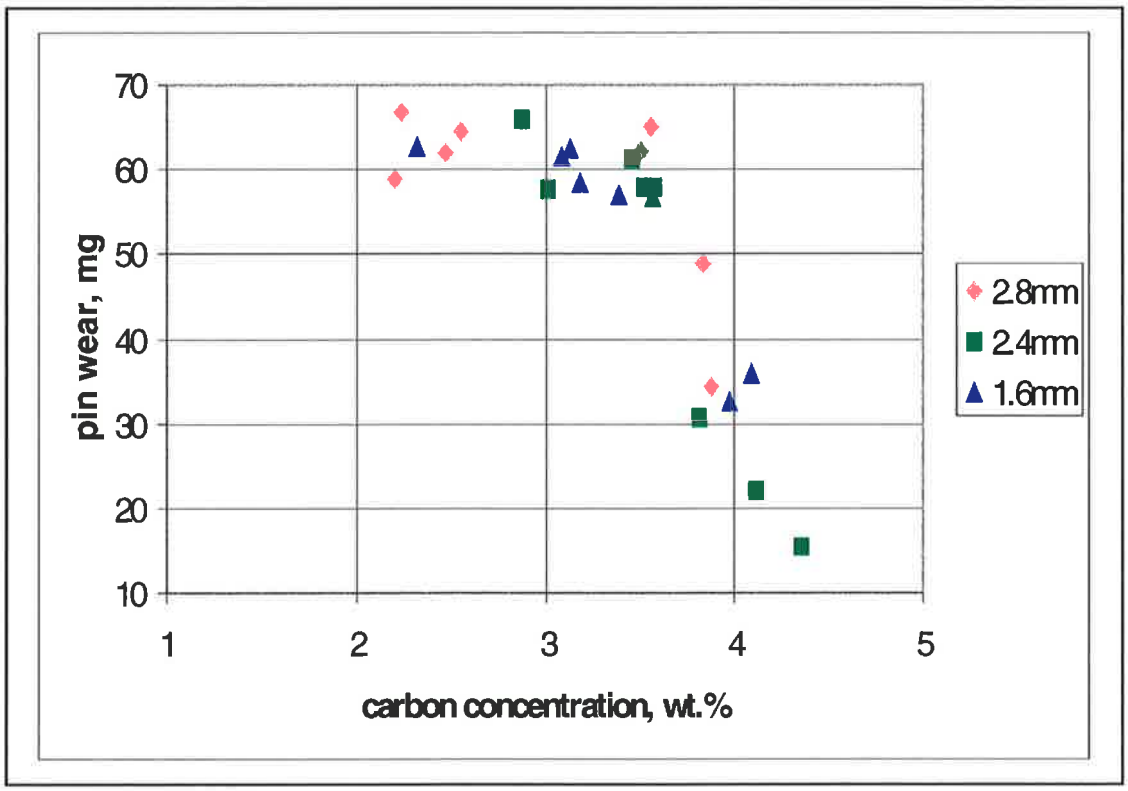

Figure 4.5: - Pin weight loss vs carbon concentration in the weld deposit for three different welding consumables (after Yellup *et al.*, 1996).

Most of Rense's samples would have been hypoeutectic according to the formula of Maratray and Usseglio-Nanot (1970) and the liquidus surface of Jackson (1970). Maratray's equation (equation 4.1) predicts that the eutectic micro-constituent has a carbide volume fraction of approximately 36%.

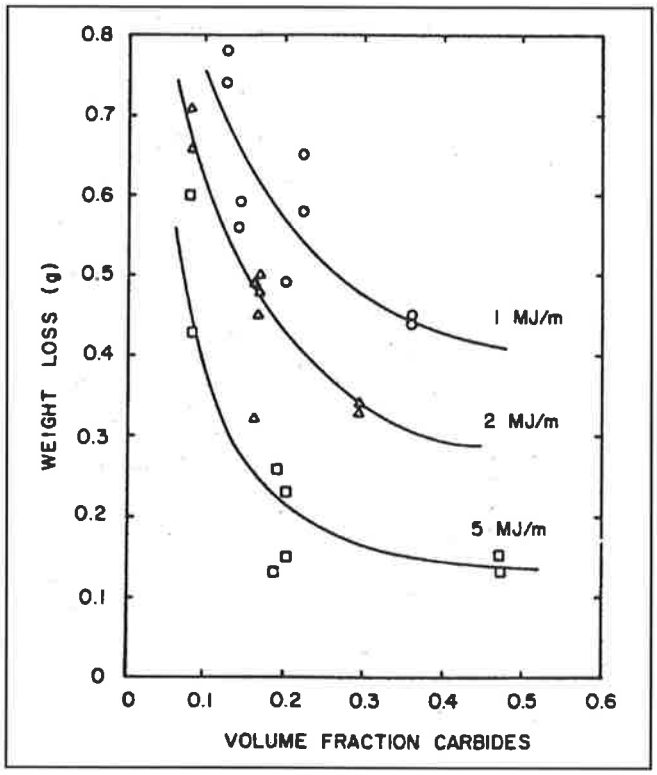

Figure 4.6: - The Dry Sand/Rubber Wheel wear data of Rense, Edwards and Frost (1983). These workers deposited their white-iron overlays in such a way that, in each case, they achieved one of three different heat input conditions; namely 1, 2 or 5kJ/mm.

It can be seen that Rense's data suggest that eutectic carbides offer significant benefits to wear performance. However, the benefits appear to diminish as the heat input is reduced and the solidification rate increases. In fact, the cooling rates observed by these workers would have been considerably slower than those in the current work. Rense *et al.* used

heat inputs ranging from 1 to 5 kJ/mm and, in addition, preheated all of their samples to 200°C. In the current work the heat inputs for the wear-tested samples ranged from 0.7 to 2.8 kJ/mm and none of the samples were preheated. Based on the results of this high-stress abrasion test, one might conclude that the fast cooling rates associated with welding significantly reduce the contribution of the eutectic carbides to the abrasion resistance of the deposit. It would therefore appear to be advantageous, in many applications, to ensure that a hypereutectic microstructure is achieved, so that the larger primary carbides can provide the desired improvements in abrasion resistance.

4.4.3 Analysis of Results

It was seen in section 2.6.6 that Zum Gahr (1987) treated wear resistance as though it were a material property, with it being equal to the reciprocal of the wear rate. For composite materials he applied both linear and inverse rules of mixtures to obtain theoretical upper and lower bounds for wear resistance. He also performed pin-abrasion tests on pins taken from a variety of white iron castings and observed that the wear rates fell between his predicted upper and lower limits.

Zum Gahr found that his pin wear data were adequately described by the following expression for the wear resistance of a composite material, W_c^{-1}:

$$W_c^{-1} = (1 - v)^2 W_m^{-1} + v^2 W_r^{-1}$$

where W_m^{-1} and W_r^{-1} are the wear resistances of the matrix and reinforcement respectively, and v is the volume fraction of the reinforcing phase present in the material. This expression was tested on the data obtained in the current work but the resulting fits were poor. An alternative empirical expression is proposed here:

$$W_c^{-1} = W_m^{-1} + (W_r^{-1} - W_m^{-1})\, v^q \quad \cdots\cdots\cdots (4.5)$$

where q is a fitted parameter. This form of expression ensures that the predicted wear resistance for the composite is intermediate between the wear resistances of the constituent phases for all values of v. When q is equal to unity, equation 4.5 becomes a linear interpolation between the wear resistance of each constituent based on the volume fractions of each present. In principle, q should always be greater than or equal to unity.

High-chromium white irons can be treated as composite materials. However, the wear results plotted in Figure 4.5 reveal an abrupt change in wear rate at the eutectic composition. Consequently, it was decided to separate the weld deposits into two categories, namely hypoeutectic and hypereutectic deposits. With this approach the eutectic micro-constituent is treated as a phase. In hypoeutectic deposits the matrix will comprise dendrites of austenite-martensite and the eutectic micro-constituent will be the reinforcing phase. In hypereutectic deposits the matrix is considered to be the eutectic micro-constituent and the reinforcing phase comprises the primary carbide needles.

The wear results plotted in Figure 4.5 were fitted by using the reciprocal of equation 4.5, *i.e.*:

$$W_c = (W_m^{-1} + (W_r^{-1} - W_m^{-1})\, v^q)^{-1} \quad \cdots\cdots\cdots (4.6)$$

The results are summarised in Table 4.3. The volume fractions of the respective phases were estimated using the Maratray formula (equation 4.1). Equation 4.1 predicts a total carbide volume fraction (*TCVF*) of approximately 36% for the eutectic micro-constituent at all eutectic compositions on the metastable phase diagram of Jackson (1970). Thus,

for hypoeutectic materials it is possible to estimate the *TCVF* and interpolate between 0% and 36% *TCVF* for the volume fraction of the eutectic constituent. Similarly, for the hypereutectic materials it is possible to estimate the *TCVF* and interpolate between 36% and 100% *TCVF* for the volume fraction of primary carbides.

Deposit Type	No. of Samples	W_m (mg)	W_r (mg)	q	Std. Error
hypoeutectic	**14**	**63.3**	**58.1**	**4.68**	**2.8**
hypereutectic	**10**	**60.1**	**3.9**	**1.30**	**7.8**

Table 4.3: - A summary of the results of fitting the pin wear data in Figure 4.5 to equation 4.6. W_m and W_r are the fitted weight losses for 100% matrix and 100% reinforcement respectively. The standard error is the standard error in weight loss in mg.

Table 4.3 suggests that if a high-dilution weld deposit comprising 100% austenite-martensite were to be tested then the pin weight loss would be 63.3mg. Reducing the dilution until the microstructure is 100% eutectic results in little benefit with the resulting weight loss being 58.1mg. However, if it were possible to deposit an overlay comprising 100% primary carbides the predicted weight loss is only 3.9mg. In principle, the fitted wear rate of 100% reinforcement in the hypoeutectic fit should be equal to the fitted wear rate of 100% matrix in the hypereutectic fit, since in both cases these correspond to a 100% eutectic deposit. It can be seen that there is satisfactory agreement (58.1mg compared with 60.1mg).

Figure 4.7 shows the measured weight losses for the hypereutectic samples plotted against the fitted values. Although there is significant scatter in the data, it may be attributed in part to variations between welding consumables. It can be seen that the data obtained from the 2.4mm diameter consumable are centred below the fitted values whereas the data from both the 2.8mm diameter and the 1.6mm diameter consumables are centred above the fitted values. It is possible that, due to small differences in composition, one consumable consistently achieved higher (or lower) values of retained austenite than the others, and this may be reflected in the results of the wear testing.

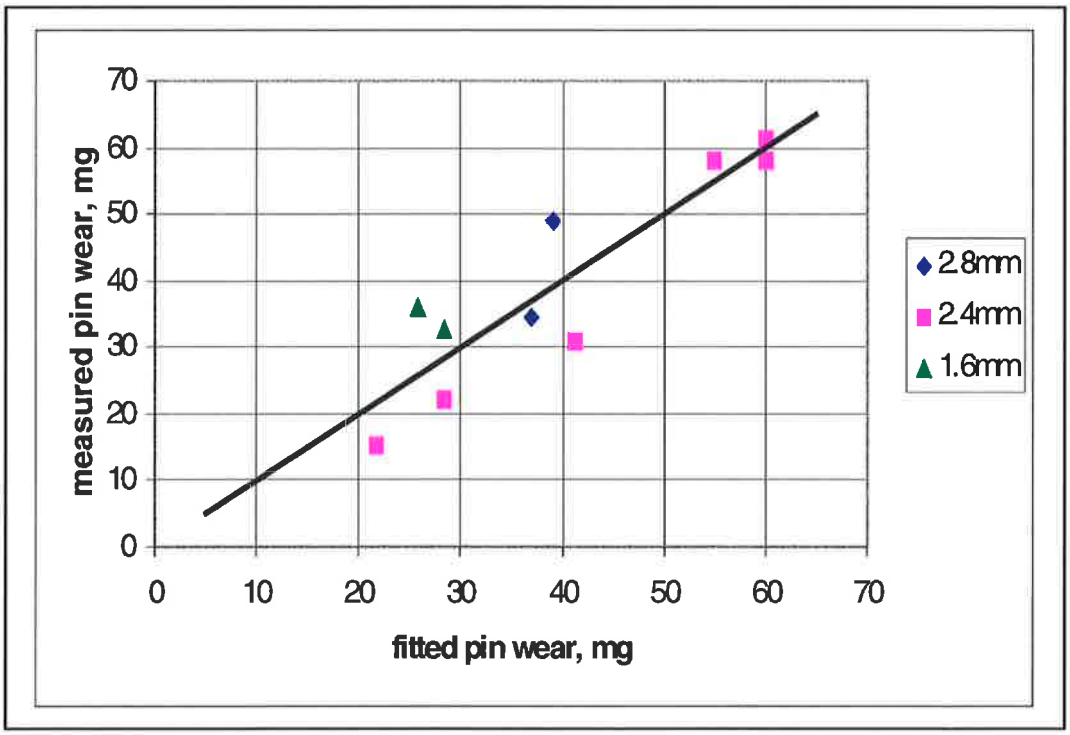

Figure 4.7: - Measured vs fitted weight losses for the hypereutectic samples obtained with three different welding consumables. The standard error for the fit was 7.8mg (see Table 4.3).

The data of Zum Gahr and Eldis (1980) were analysed in order to clarify whether equation 4.5 adequately describes the abrasive wear resistance of a material. (These data were included in Figure 2.7 – page 33). These workers cast thirteen high-chromium

white irons from induction melted heats, with varying carbon and chromium contents. The chemical compositions were tabulated for each heat number, nine of which would have produced hypoeutectic irons according to the metastable liquidus surface of Jackson (1970). The total carbide volume fractions were also measured for each composition. For each of the compositions studied, Zum Gahr and Eldis produced both a sample with a predominantly austenitic matrix and a sample with a predominantly martensitic matrix by varying the heat treatment. Pin-abrasion tests were performed on all samples using either 150-mesh garnet or 180-mesh silicon carbide.

The wear data for the nine hypoeutectic compositions were analysed and fitted to equation 4.6. Fits were obtained for both the austenitic samples and the martensitic samples. The results are summarised in Table 4.4.

Deposit Type	No. of Samples	W_m (mm^3)	W_r (mm^3)	q	Std. Error
austenitic	**9**	**6.09**	**0.81**	**3.35**	**0.22**
martensitic	**9**	**4.10**	**0.95**	**3.17**	**0.07**

Table 4.4: - A summary of the results of fitting the data of Zum Gahr and Eldis (1980) to equation 4.6. W_m and W_r are the fitted volume losses for 100% matrix and 100% reinforcement respectively. In all cases the abrasive was 150-mesh garnet. The standard error is the standard error in volume loss in mm^3.

The volume losses measured by Zum Gahr and Eldis are plotted against the fitted values in Figures 4.8 and 4.9. It can be seen that the fits are both satisfactory. Equation 4.5 appears to adequately describe the abrasive wear performance of high-chromium white irons. The fitted volume loss for the austenite dendrites in Table 4.4 (*i.e.* 6.09mm^3) is

higher than the fitted value for a martensitic matrix (*i.e.* 4.10mm^3), as one would expect. Another interesting point arises, however, in that the wear performance of Zum Gahr and Eldis' hypoeutectic castings is very sensitive to composition. The data in Table 4.4 suggest that a 100% austenitic or martensitic matrix will wear at four to six times the rate of a 100% eutectic casting. This is in contrast to the weld deposit data plotted in Figure 4.5, which show the weight losses to be relatively insensitive to composition below 3.5%C, and once again suggests that fast cooling rates could be deleterious to the wear performance of the eutectic constituent.

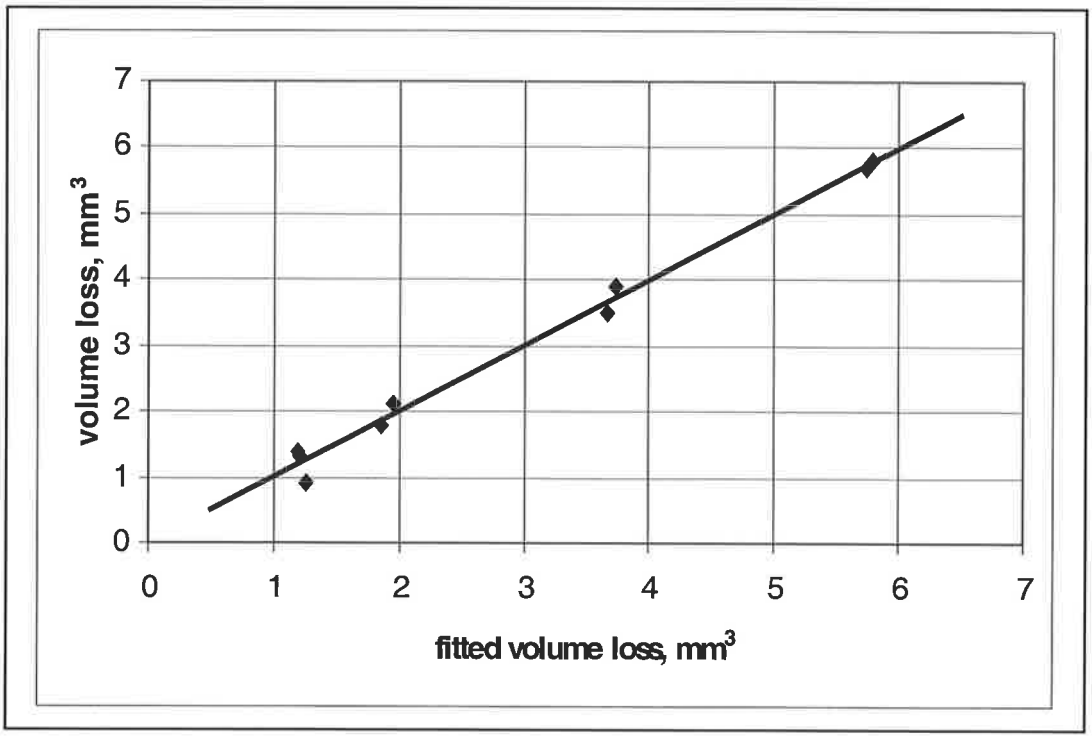

Figure 4.8: - The pin-abrasion data of Zum Gahr and Eldis (1980). The measured values are plotted against the fitted values. These tests were performed on samples with a predominantly austenitic matrix. The abrasive was 150-mesh garnet.

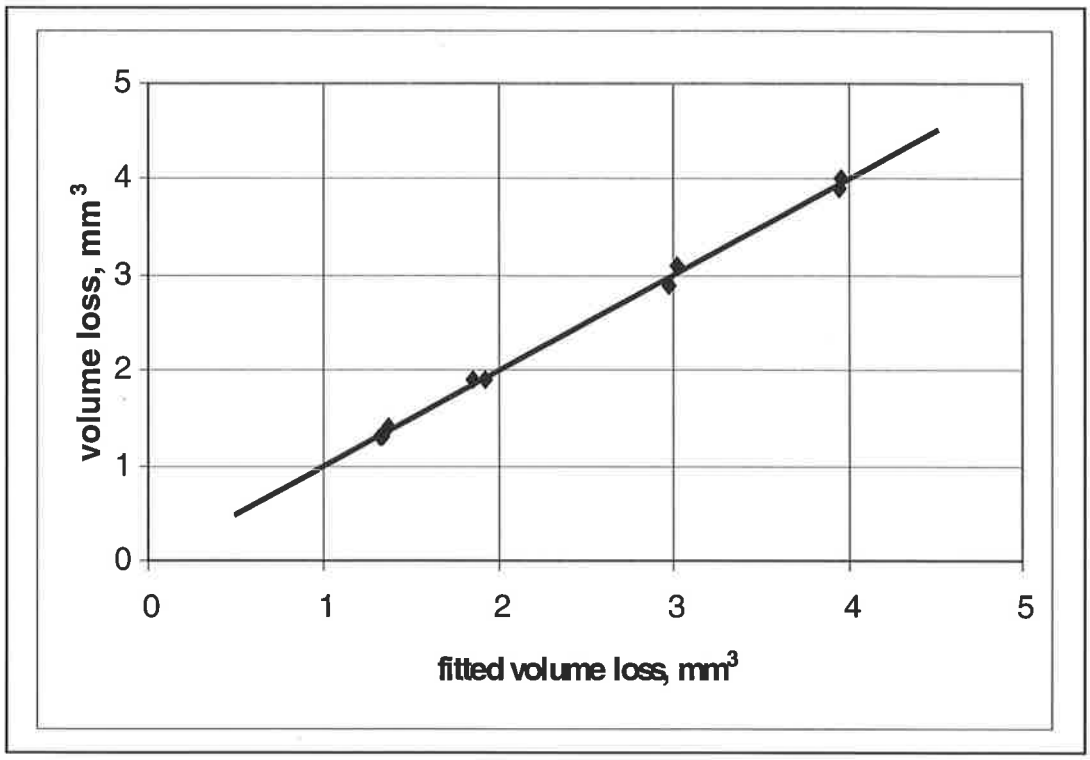

Figure 4.9: - The pin-abrasion data of Zum Gahr and Eldis (1980). The measured values are plotted against the fitted values. These tests were performed on samples with a predominantly martensitic matrix. The abrasive was 150-mesh garnet.

4.5 CONCLUSIONS

Weld deposits rich in primary carbides (*i.e.* low-dilution deposits) offer the best resistance to high-stress abrasion when garnet is the abrasive. Zum Gahr and Eldis (1980) also found that high volume fractions of carbides were beneficial with respect to abrasion resistance, provided that the M_7C_3 carbide was harder than the abrading particles. According to Gundlach and Parks (1978), quartz and garnet are representative of the abrasives most commonly encountered in service in the minerals processing industry. Thus, one would expect low-dilution deposits to provide optimum abrasion resistance in many applications.

The fast cooling rates associated with welding appear to reduce the contribution of the eutectic carbides to the abrasion resistance of the deposit. It would therefore appear to be advantageous to achieve a dilution that is low enough to ensure that primary carbides are present in sufficient quantities for the particular application.

The formula proposed by Maratray and Usseglio-Nanot (1970) is, at present, the most effective approach for estimating total carbide volume fraction. There do not appear to be any procedures for estimating volume fractions of primary carbides. This task is more difficult due to the possibility of forming a complex regular microstructure.

It would appear that the analytical approach to abrasive wear initiated by Zum Gahr (1987), when combined with equation 4.5, describes the abrasive wear of white-iron weld deposits with reasonable accuracy. This approach will predict the wear rates for different overlay compositions in a given wear system provided one has access to previous wear results. (The previous wear results are required to obtain values for the three fitted parameters in equation 4.5.) It should be noted, however, that equation 4.5 is an empirical expression and was not derived from first principles. Nevertheless, it appears to be useful for both weld-deposited and cast white irons. While it is anticipated that equation 4.5 will accurately describe high- and low-stress abrasive wear data, it is believed to be a tool best suited to interpolation, not extrapolation.

5
FIELD TRIALS

5.1 INTRODUCTION

The previous chapter examined the relationship between the microstructure of a single-bead deposit and its abrasive wear performance, as measured under laboratory test conditions. After the laboratory testing was completed a plan was developed for a series of field trials. The aim of the trials was to establish whether there is a correlation between the results of laboratory wear testing and the wear performance observed in the field.

Two trials were initiated. The first involved depositing a range of hardfacing overlays on to a pair of wear plates that were to be put into service at a quartz quarry. The second involved depositing a similar range of overlays on to sets of plates that were to be used in a jaw crusher. In each case, the intention was to test several different microstructures under nominally identical service conditions.

The two dominant influences on the wear performance of an overlay are the geometry of the deposit and its microstructure. In order to isolate the effects of microstructure it is necessary to achieve the same geometry in each deposit, yet still vary the microstructure for each overlay. Such a constraint would require each overlay to have the same height, width and length, but a different penetration so that in each case the dilution would be different. These experiments are believed to be the first of their kind. They presented

many challenges and required very careful selection of welding parameters. The purpose of this chapter is to describe the experiments and their significance.

5.2 THE HEEL PLATES EXPERIMENT

5.2.1 Description of Experiment

Five single-layer overlays were deposited on each of a pair of heel plates for the excavation bucket of a Caterpillar 988F wheel loader. The plate dimensions were 680mm by 254mm and the thickness was 25.4mm. Four different sets of welding parameters were used. The sets of parameters were selected in such a way that they achieved four different microstructures, yet the pad dimensions were nominally identical at 200mm by 60mm and 5 ± 0.5mm high. Table 5.1 summarises the conditions that were used and the microstructures that were achieved.

Figure 5.1 shows a heel plate before it was put into service. The same welding consumable was used for all of the overlays. The consumable will be referred to as consumable B (described in section 3.2). Direct-current-electrode-positive polarity was used in all cases. Preheat temperatures were determined in accordance with the properties of the base steel from published data by WTIA : Technical Note 1 (1996). The preheat temperature required for condition 1 is higher due to the lower heat input.

In order to maintain flatness of the heel plates and to facilitate their subsequent bolting on to the bucket they were restrained by clamping during welding. The clamps were released after cooling. The ends of each pad were then ground so that, for each pad, there was a ramped transition from the substrate to full overlay height. The plates were bolted on to the lower surface of a wheel loader excavation bucket and put into service at

Boral's quartz quarry, Stonyfell, South Australia (see Figure 5.2). The service conditions would best be described as highly abrasive with moderate impact. The plates remained in service for 174 operating hours before they were removed for examination.

Overlay No.	Voltage	Current (A)	Speed (mm/min)	Work Dist. (mm)	Step (mm)	Height (mm)	Preheat (°C)	Microstructure
1	**25**	**230**	**240**	**40**	**8**	**5.0**	**115**	Hypereutectic (hvf)
2	**33**	**410**	**380**	**40**	**10**	**5.0**	**60**	Eutectic
3	**36**	**490**	**270**	**30**	**19**	**4.5**	**60**	Hypoeutectic
4	**33**	**410**	**380**	**40**	**10**	**5.0**	**60**	Eutectic
5	**30**	**370**	**310**	**40**	**10**	**5.5**	**60**	Hypereutectic (lvf)

Table 5.1: - A summary of the heel plate welding conditions. These conditions were selected to achieve specific microstructures and are not necessarily suggested operating conditions. The 'hvf' and 'lvf' refer to high volume fraction and low volume fraction of primary carbides respectively. The average heights were obtained from an additional set of overlays that were deposited on a set of test plates (described in the next section), to avoid cutting the heel plates. Preheats were not used for the test plate overlays but, otherwise, the welding parameters were identical to those listed above.

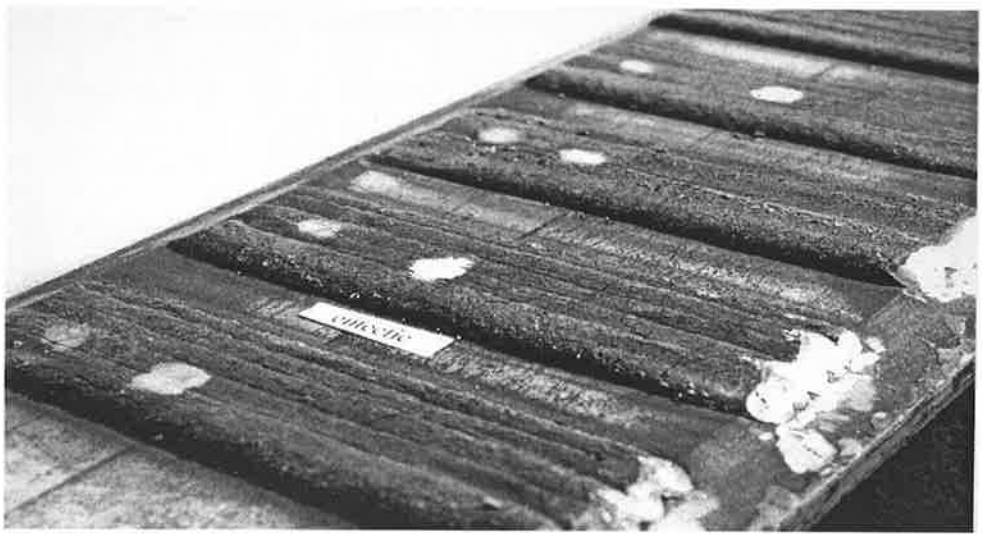

Figure 5.1: - A heel plate before service.

Figure 5.2: - The arrows show the location of the heel plates on the excavation bucket of the Caterpillar 988F wheel loader.

Conditions 2 and 4 in Table 5.1 were identical and served as reference overlays. If the wear pattern on the plates were to be biased to one side this bias should be discernible from a comparison of the reference deposits.

5.2.2 Methodology for Selecting Welding Parameters

The intention with overlay number 1 was to achieve a hypereutectic microstructure with a high volume fraction of primary carbide needles. It was necessary to have a low dilution in order to obtain such a microstructure. Consequently, a low voltage was chosen in accordance with the findings of previous studies (summarised in Table 2.1 – page 10) and the model for single-bead dilution (see sections 2.2.3 and 3.6). A low welding current was also selected in view of the fact that, for a multi-pass overlay of a specified height, it is the average penetration, rather than the single-bead dilution, that

needs to be minimised. (The average dilution of a multi-pass deposit can be determined metallographically from the average height and average penetration of the deposit, as shown in Figure 5.3.) This realisation was one of great importance. It suggested that the optimum conditions for single beads may not necessarily correspond to the optimum conditions for multi-pass overlays. For a single-bead deposit it is the ratio of material deposited to material melted that is critical, and there is usually no restriction on the height of the bead. The height of a multi-pass overlay, however, is usually specified before the overlay is deposited. The average height is directly proportional to the consumable costs and is thus an important constraint. It is a constraint that also makes the philosophy for depositing multi-pass overlays and single beads fundamentally different. This issue is addressed in chapters 6 and 7.

In order of increasing dilution the overlay numbers were 1, 5, 2 (and 4), 3. In each case an increase in dilution was achieved by increasing the welding current and voltage as required. The welding current has a greater influence on average overlay dilution. The average penetration (see section 3.4) and deposition rate (see equation 2.4 – page 12) both increase with increasing current. An increase in penetration will result in a higher average dilution if the overlay height remains unchanged. The deposition rate effects, however, are not as obvious. As the deposition rate increases, the step-over needs to be increased in order to maintain the required overlay height. This results in a reduction in bead overlap and a corresponding shift in arc impingement away from the previous bead toward unmelted substrate, thus increasing dilution.

All of the selected welding conditions were first tested on 25.4mm thick steel substrates. After the test overlays were deposited they were sectioned, polished and etched with

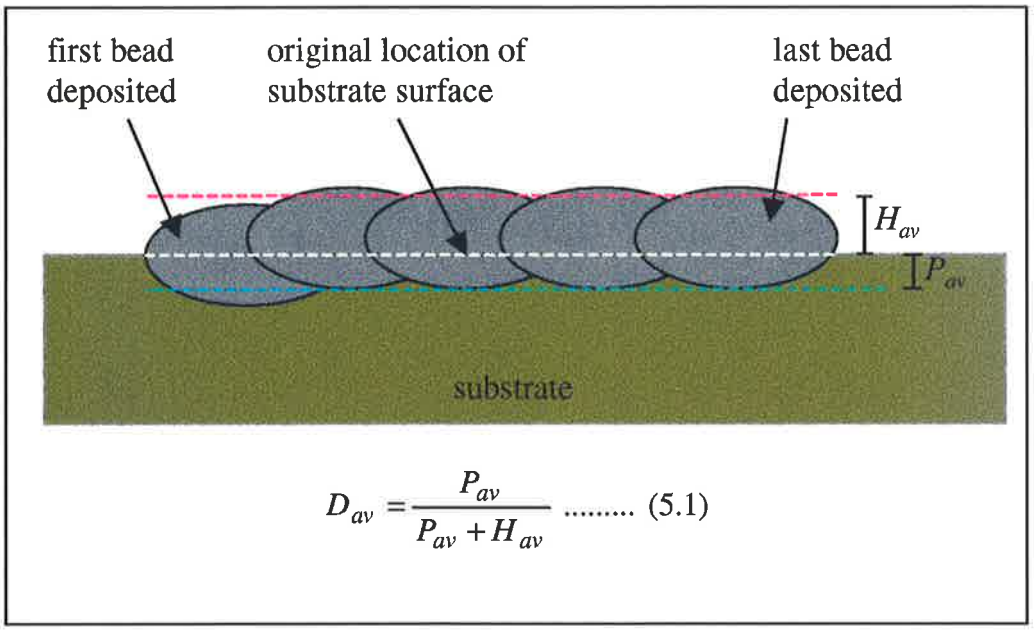

Figure 5.3: - The metallographic measurement of the average dilution of a multi-pass overlay. H_{av} and P_{av} are the average height and penetration for the deposit respectively.

Vilella's reagent so that average dilutions could be measured. The microstructure of each deposit was then examined using an optical microscope. Small adjustments to the welding parameters were required to ensure that, in each case, the desired microstructure was achieved. The tests were then repeated, and the microstructures were once again examined before deposition commenced on the heel plates. The microstructures of the test plates are shown in Figures 5.4.

The complete heel plate deposits were then examined using an in-situ metallographic technique. A small area, approximately 10mm by 10mm, on the surface of each deposit was ground smooth with a grinder and polished with 5μm diamond paste. The prepared surfaces were then placed on an inverted-stage optical microscope. All microstructures were similar to those shown for the test plates in Figures 5.4.

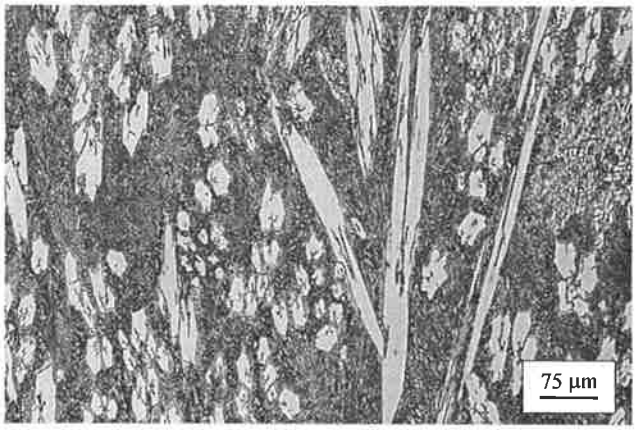

Figure 5.4(a): - A typical micrograph from the test plate for condition 1 in Table 5.1. This structure would be described as a conventional hypereutectic microstructure with a high volume fraction of primary carbides.

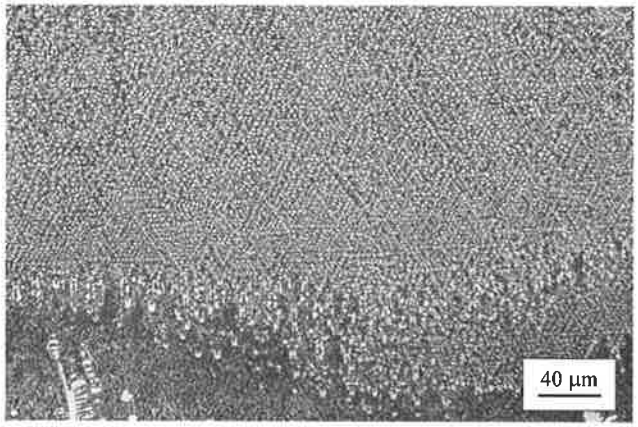

Figure 5.4(b): - The complex regular microstructure (shown above) was also present in the test overlay for condition 1 . Carbides can be seen to appear in clusters exhibiting three-fold rotational symmetry.

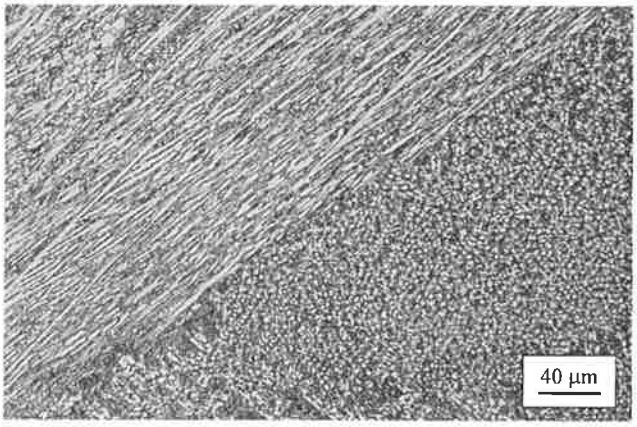

Figure 5.4(c): - This micrograph from test overlay number 1 shows the boundary between two complex regular crystals that have different orientations. The boundary follows a path from the bottom left-hand corner of the micrograph to the top right-hand corner. The carbides in the top left-hand grain generally appear as needles that are approximately parallel to one another. The carbides in the bottom right-hand grain are generally seen in cross-section.

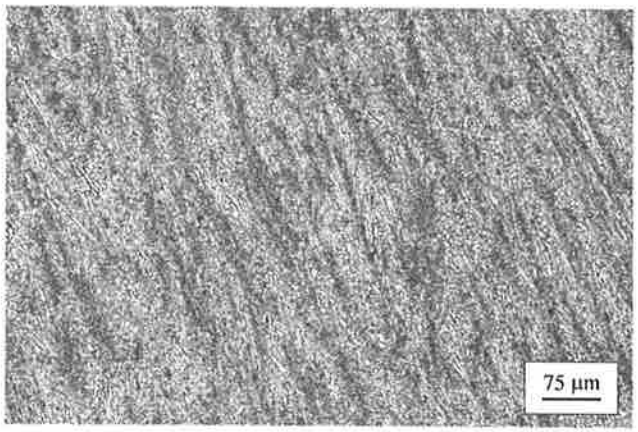

Figure 5.4(d): - A typical micrograph from the test plate for conditions 2 and 4 in Table 5.1. This structure would be described as predominantly eutectic.

Figure 5.4(e): - A typical micrograph from the test plate for condition 3 in Table 5.1. This overlay was hypoeutectic. Dendrites of austenite can be seen in the structure. The dendrites are surrounded by the eutectic constituent.

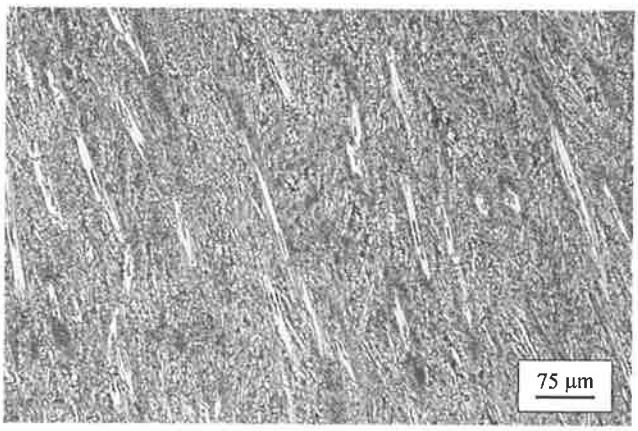

Figure 5.4(f): - A typical micrograph from the test plate for condition 5 in Table 5.1. This overlay was hypereutectic with a low volume fraction of primary carbides.

5.2.3 Achieving the Specified Overlay Height

It was mentioned in the previous section that the average height of an overlay would usually be specified before the overlay is deposited. In practice, the average height of the overlay under steady-state conditions is specified.

Consider the case where an overlay of steady-state height, H_{ss}, is to be deposited on a flat plate of breadth, B, and length, L, with open-arc FCAW. The configuration is shown schematically in Figure 5.5. Let it be assumed that a steady-state condition is achieved before deposition commences on the plate, for example, by the incorporation of a run-on plate.

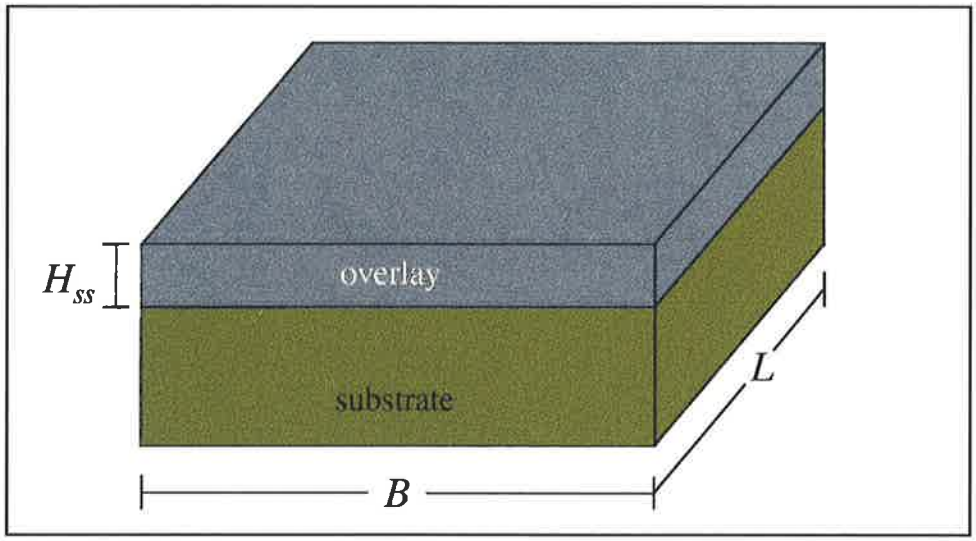

Figure 5.5: - The configuration of an overlay. The steady-state height, H_{ss}, does not include the depth of penetration.

There will be three major influences on the steady-state overlay height, namely:

- The deposition rate, W
- The travel speed, S
- The step-over, δ

The deposition rate, W, is given by:

$$W = \eta_d f m \quad \cdots\cdots\cdots (5.2)$$

where η_d is the deposition efficiency, m is the mass per unit length of the welding consumable and f is the wire feed rate. For the high-chromium high-carbon consumables studied in this work, the deposition efficiencies were high (see section 3.7), with typical values falling between 95 and 98%. It would therefore be reasonable to assume a deposition efficiency of 95% for similar consumables. The mass per unit length of wire, m, is readily obtained from the manufacturers' data sheets or by direct measurement and the wire feed speed is usually set by the operator and recorded on the welding procedure sheet. Thus, all of the information required to estimate the deposition rate is available.

The travel speed is another parameter set by the operator and recorded on the welding procedure sheet. Consequently the step-over, δ, is the only remaining parameter that needs to be determined in order to achieve the correct overlay height, and it can be obtained by applying the principle of conservation of mass.

The total mass added to the plate will be equal to the product of the added volume and the density of an all-weld-metal deposit, ρ. It will also be equal to the product of the deposition rate, W, and the total welding time, t. Thus we have the following relationship:

$$W t = \rho L B H_{ss} \quad \cdots\cdots\cdots (5.3)$$

The total welding time can be expressed in terms of the number of passes required to cover the plate, N, the length of the plate, L, and the welding speed, S.

$$t = N \frac{L}{S} \quad \ldots\ldots\ldots \quad (5.4)$$

Under steady-state conditions the number of passes required to cover the plate, N, is given by dividing the plate width, B, by the step-over, δ, *i.e.*:

$$N = \frac{B}{\delta}$$

Substituting for N in equation 5.4, and then substituting equation 5.4 into 5.3 gives:

$$\delta = \frac{W}{\rho H_{ss} S} \quad \ldots\ldots\ldots \quad (5.5)$$

Equation 5.5 may be used in conjunction with equation 5.2 to determine the step-over that will give the desired steady-state overlay height for a given set of welding parameters. Alternatively, it will predict the steady-state height for a given step-over. This equation gives the correct average height but does not give any indication of the overlay uniformity. Equation 5.5 requires all parameters to be entered in SI units.

5.2.4 Results

Visual examination showed that, whereas all pads revealed some wear, the hypereutectic deposits showed an incidence of metal loss by spalling. Spalling was worst on the deposits that had a high volume fraction of primary carbides, but also occurred on the overlays with low volume fractions. In all cases spalling had initiated at the corner of the overlay deposit. There was no evidence of spalling on the eutectic or hypoeutectic samples.

In order to get an indication of abrasion resistance, volume loss measurements were performed on those areas of each pad that had not spalled. It was found that only small amounts of each pad had been removed by abrasion and that substantially more service time would have been required in order to obtain meaningful abrasive wear data.

Figure 5.6 shows the condition of a heel plate after 174 hours service. Conditions 1 to 5 (in Table 5.1) appear from left to right respectively. It can be seen that the bottom left hand corner of the left-most deposit has completely disappeared. Spalling has also commenced on the right-most deposit, with the top-left and bottom-left corners being removed.

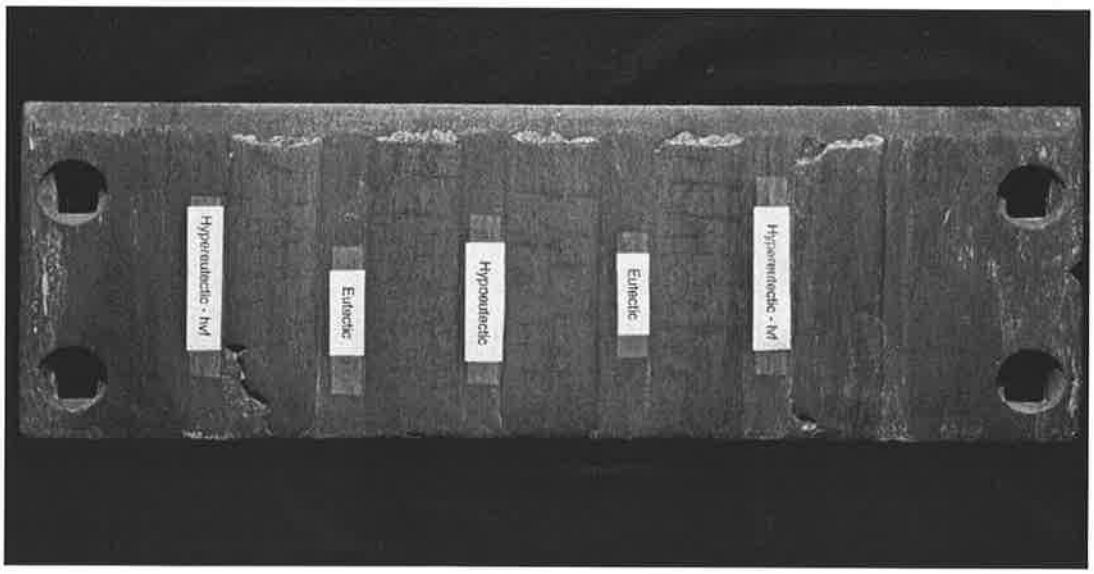

Figure 5.6: - A heel plate after service.

5.3 THE JAW-CRUSHER EXPERIMENT

5.3.1 Description of Experiment

The heel plates experiment was followed by a jaw-crusher experiment. The welding parameters listed in Table 5.1 were once again employed, with the exception of condition 1, which was replace by a welding condition that had a higher overlap in order to reduce dilution. In this instance the overlays were deposited on a set of jaw-crusher plates approximately 220mm long, 75mm wide and 25mm thick. Two different batches of welding consumable were used and, as a result, the microstructures were not identical to those produced in the heel plates experiment. Nevertheless, four different microstructures were produced.

This trial was conducted with the assistance of a project team that had previous experience with jaw crusher tests. The clad plates were tested in the as-deposited surface condition as stationary and moving half jaws in a single-toggle crusher in accordance with the procedure described in ASTM Standard G81-83. Each plate was used to crush 1000kg of quartzite-bearing rock, designated "ANR Ballast", in the size range 25 – 50mm. It was necessary to increase the jaw opening in order to accommodate the size of the rock and to ensure correct operation of the crusher. The same jaw opening was, however, used in all tests and the results were compared to those for a quenched and tempered steel, which served as a reference material. The test strategy was based on the work of Sare and Constantine (1991). The wear mechanism in this type of test is believed to be gouging abrasion.

5.3.2 Results

Table 5.2 summarises the weight losses for each microstructure. The data suggest that the best wear performance, in this particular application, is offered by microstructures that are either near-eutectic or hypereutectic with a low volume fraction of primary carbides. Typical wear surfaces for both stationary and moving jaws are shown in Figures 5.7(a) and 5.7(b) respectively. It can be seen that the low-dilution deposits, *i.e.* those with high primary carbide volume fractions, developed the greatest number of check cracks. These samples were also the most susceptible to accelerated metal loss by spalling.

Microstructure	Weight Loss, g (Stationary Jaw)	Weight Loss, g (Moving Jaw)
Hypoeutectic	17	12
Eutectic to near-eutectic	15	11
Hypereutectic – lvf	16	9
Hypereutectic – hvf	23	13
Reference material	50	36

Table 5.2: - The average weight losses in grams for each type of microstructure in the jaw-crusher tests. "lvf" and "hvf" refer to low volume fraction and high volume fraction of primary carbides respectively.

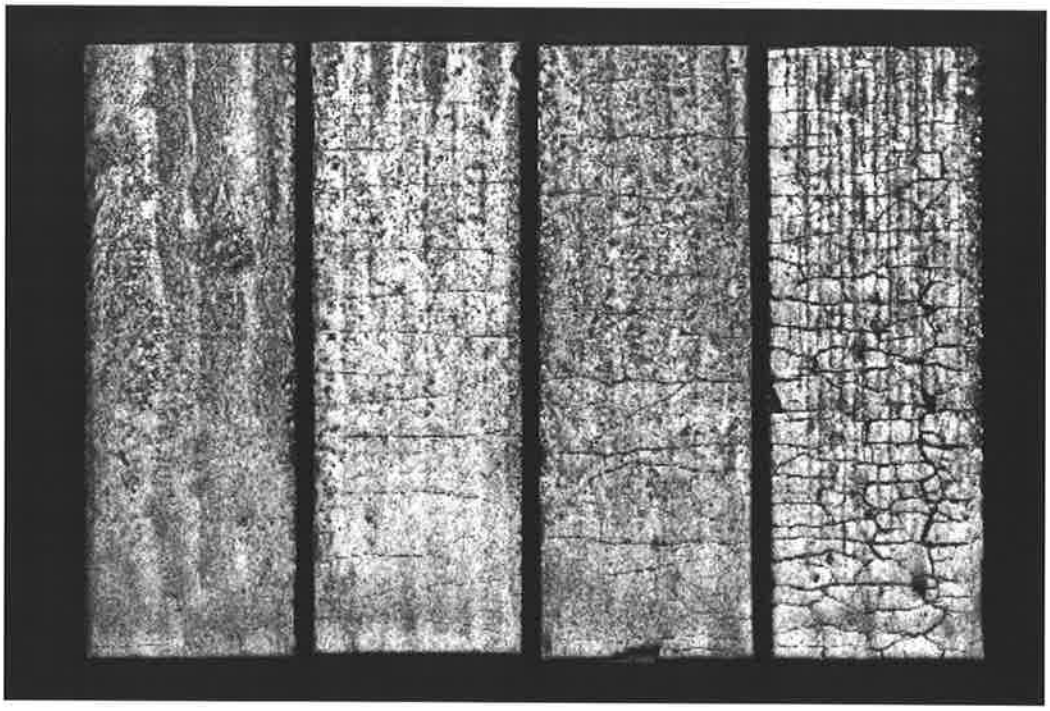

Figure 5.7(a): - The stationary jaw-crusher plates after crushing 1000kg of quartzite-bearing rock. The microstructures of the plates were, from left to right, hypoeutectic, eutectic to near-eutectic, hypereutectic (lvf) and hypereutectic (hvf).

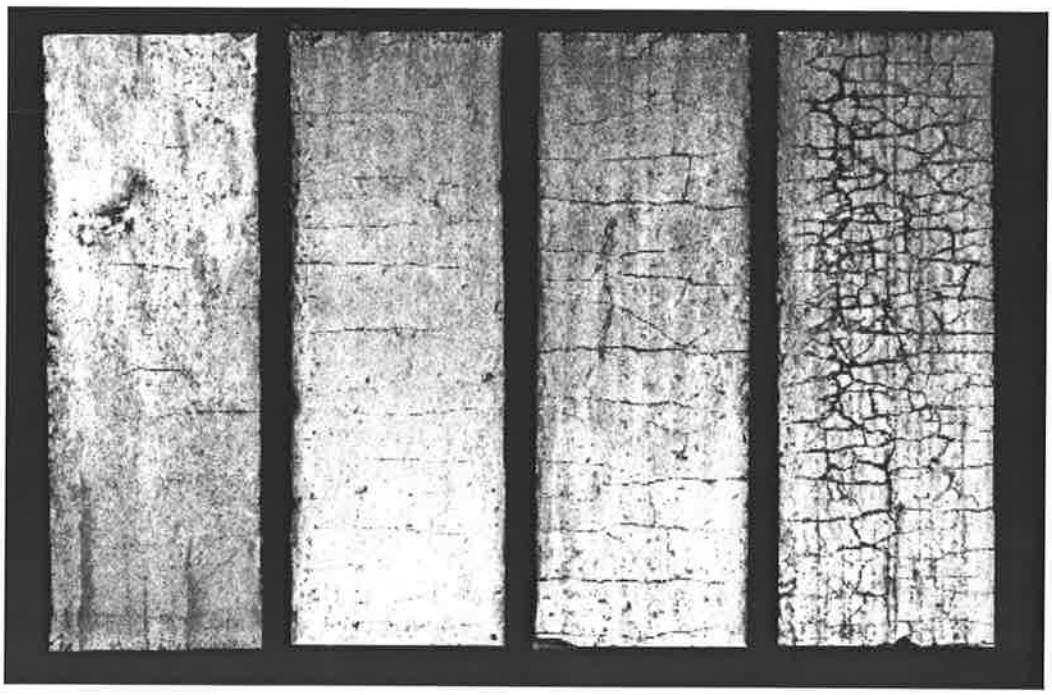

Figure 5.7(b): - The moving jaw-crusher plates after crushing 1000kg of quartzite-bearing rock. The microstructures of the plates were, from left to right, hypoeutectic, eutectic to near-eutectic, hypereutectic (lvf) and hypereutectic (hvf).

5.4 DISCUSSION

The heel plate and jaw-crusher experiments both demonstrated that the selection of welding parameters does affect the wear performance of an overlay. In each case, four overlay types were deposited on to the same substrate material with the same type of welding consumable. The geometry of each deposit was nearly identical but four different microstructures were produced. In both experiments there were differences in the wear performance of each deposit type, and they were observed in the form of spalling tendency.

The wear results revealed that the single-layer hypereutectic deposits exhibit a much greater spalling tendency than higher dilution deposits. The overlays with high volume fractions of primary carbides were most susceptible to this form of metal loss. This is possibly related to the reduction in fracture toughness that is likely to occur as the primary carbide volume fraction increases. Berns and Fischer (1986) studied hardfacing weld deposits and found that their fracture toughness data were adequately described by an energy model proposed by Chermant and Osterstock (1976). The model claims that the matrix is the most important factor in influencing the fracture toughness. Berns and Fischer treated the eutectic constituent as the matrix and found that, as the eutectic areas became smaller, so too did the fracture toughness. The eutectic areas and the resulting fracture toughness are likely to decrease significantly as the primary carbide volume fraction increases.

Hutchings (1992) described the role that material hardness and fracture toughness play in determining the apparent abrasion resistance of a material. He described how abrasive wear may occur by mechanisms dominated either by plastic deformation or

brittle fracture. If plastic deformation was dominant, the hardness of the counterface was said to be an important factor in determining its wear resistance. If, however, brittle fracture was dominant then the fracture toughness was said to be more important than the hardness. Based on the description given by Hutchings, one might expect that high-chromium white irons will generally provide excellent resistance to low-stress abrasion. In low-stress abrasion the hardness of the overlay is likely to be more important than its fracture toughness. However, as the applied stresses and the level of impact increase, so too will the importance of the fracture toughness of the overlay. Under conditions of high-stress abrasion the wear performance of a white iron deposit will also depend on such factors as the applied stresses, the hardness and size of the abrading materials, and whether these particles can penetrate and crack the carbides in the overlay. If the stresses are not too high, and if the carbides are harder than the abrading particles, then a low-dilution white-iron overlay may still perform very well. (This was seen in the results of pin-abrasion testing in chapter 4.) Under conditions of gouging abrasion, however, the levels of impact that are present are likely to ensure that the fracture toughness of the overlay is more important than its hardness. Consequently, low-dilution deposits are likely to wear at faster rates than deposits with higher dilutions, and this was seen in the heel plates and jaw-crusher experiments.

The fact that optimum wear performance was not provided by minimising dilution suggests that high-chromium white iron welding consumables were not the best selection for these applications. Articles by Menon (1996) and Zollinger *et al.* (1998) suggest that white-iron overlays are ideally suited to combat low-stress abrasion but are generally not recommended for use in conditions involving either high stresses or impact.

While the level of impact in these experiments may have been sufficient to expose the low fracture toughness of white-iron weld deposits, there are other possible explanations for the results. For example, the residual stresses in single-layer hypereutectic deposits are likely to be higher than the residual stresses in hypoeutectic overlays. One would expect that as the dilution decreases (and the differences in composition between the substrate and overlay increase) the residual stresses will increase. Thus the results may not be a characteristic solely of the wear performance of a hypereutectic microstructure, but rather a characteristic of the residual stresses that arise when there is an abrupt change in composition between two very dissimilar materials. If a hypereutectic layer had been deposited on to a high-dilution buffering layer, the reduction in residual stresses may have brought about a very different result.

Another issue arises in that the presence of the complex regular microstructure (shown in Figures 5.4) may have contributed to the poor wear performance of the strongly hypereutectic deposits. Very little is known about the mechanical properties of this structure.

The most important event in carrying out these experiments was the realisation that optimum conditions for the deposition of single beads may not correspond to the optimum conditions for multi-pass overlays. If the objective is to minimise dilution then, for single beads, this is equivalent to minimising the ratio of substrate melted to material deposited. For multi-pass overlays, however, the objective is to minimise the average penetration subject to the constraint that the average height of the overlay is fixed or specified. There is, therefore, a great need to build on the understanding of single-bead deposits by investigating the factors affecting the dilution of overlapping beads.

6
AN ANALYSIS OF MULTI-PASS OVERLAYS

6.1 INTRODUCTION

The mechanisms that affect dilution in multi-pass overlays are more complex than those affecting the dilution of single-bead deposits. As was seen in section 2.2.1, the dilution of a single bead is defined by two quantities: the volume of material that is deposited and the volume of substrate that is melted. In a multi-pass overlay, however, a bead is generally formed by the melting and mixing of three materials, namely:

- the welding consumable,
- the substrate material, and
- the previous bead.

The purpose of this chapter is to develop a model of dilution for multi-pass overlays.

6.2 DEVELOPMENT OF A MODEL

6.2.1 Definition of Variables

It is helpful to consider a bead in a multi-pass overlay in terms of three area fractions. The area fractions of a bead in a multi-pass overlay are represented schematically in Figure 6.1. The first, denoted k, refers to the area fraction of the bead contributed by material deposited in that pass. The second, denoted λ, represents the area fraction of the bead contributed by material from the previous bead. The third fraction is the

contribution of new substrate material. Since the three fractions must sum to unity, the substrate fraction can be expressed in terms of k and λ as follows:

$$substrate\ \ fraction \quad = \quad 1 - k - \lambda \quad ..... \quad (6.1)$$

As k and λ are fractions they must also satisfy the following inequality:

$$k + \lambda \leq 1 \quad ..... \quad (6.2)$$

In equation 6.2 equality occurs if no substrate material is melted. Such an event may occur if one bead is deposited directly on top of another.

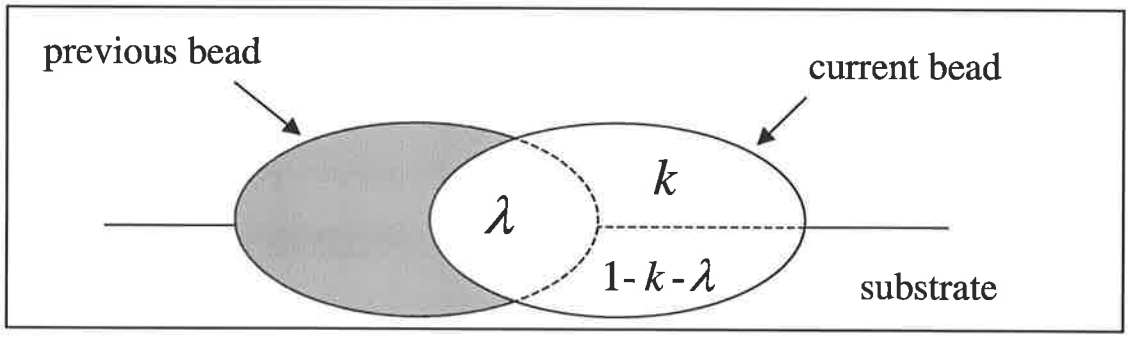

Figure 6.1: - Schematic representation of a bead in a multi-pass overlay.

It is worth noting that for a single-bead deposit $\lambda = 0$ as there is no previous bead present. In this case k assumes a value equal to the complement of the single-bead dilution, D_{sb}, *i.e.*:

$$k = 1 - D_{sb} \quad ..... \quad (6.3) \quad (\text{single - bead deposit})$$

6.2.2. Definition of Problem

Consider the case where the following ***conditions*** apply:

1) A single-layer overlay is deposited with the welding parameters being identical for each pass.
2) The all-weld-metal composition and the base material composition are different.
3) The inter-pass temperature is the same for each pass.

In addition, the following simplifying ***assumptions*** will be made:

1) Each bead in the overlay is perfectly homogeneous.
2) The total cross-sectional area of material melted is the same for each bead in the overlay and equal to that for a single-bead deposit.
3) k remains unchanged from the first bead and λ remains unchanged from the second bead until a steady-state condition is reached.

6.2.3. Analysis

If these conditions apply then the concentration of alloying element x in the first bead, denoted $[x]_1$, will be given by:

$$[x]_1 = k[x]_{awm} + (1 - k)[x]_{bm} \quad \ldots\ldots\ldots \quad (6.4)$$

where $[x]_{awm}$ = concentration of element x in an all-weld-metal deposit, and

$[x]_{bm}$ = concentration of element x in the base material.

Equation 6.4 describes the special case of a single-bead deposit where $\lambda = 0$ and equation 6.3 applies. Consider now the deposition of a second overlapping bead. The concentration of element x in this bead will be given by:

$$[x]_2 = k[x]_{awm} + \lambda[x]_1 + (1 - k - \lambda)[x]_{bm} \quad \ldots\ldots\ldots \quad (6.5)$$

Substituting equation 6.4 into equation 6.5 and rearranging gives:

$$[x]_2 = [x]_{awm}(k + \lambda k) + [x]_{bm}(1 - k - \lambda k)$$

A similar approach may be adopted for the third bead to give:

$$[x]_3 = [x]_{awm}(k + \lambda k + \lambda^2 k) + [x]_{bm}(1 - k - \lambda k - \lambda^2 k)$$

It can be shown that, if the above conditions and assumptions apply, the concentration of element x in the N^{th} bead of an overlay, $[x]_N$, will be given by:

$$[x]_N = [x]_{bm} + k([x]_{awm} - [x]_{bm}) \sum_{j=0}^{N-1} \lambda^j \quad \ldots\ldots\ldots \quad (6.6)$$

This equation will provide an estimate of the concentration of any element in any bead in the overlay, from the first bead deposited through to the steady-state condition. The sum in equation 6.6 is a geometric series and, as N becomes large, the sum converges to a limiting value, *i.e.*:

$$\sum_{j=0}^{\infty} \lambda^j = \frac{1}{1 - \lambda} \quad \ldots\ldots\ldots \quad (6.7)$$

Consequently, an expression can be written for the steady-state concentration of any element, $[x]_{ss}$, in the overlay:

$$[x]_{ss} = [x]_{bm} + \frac{k}{1-\lambda}\left([x]_{awm} - [x]_{bm}\right) \quad \ldots\ldots\ldots \quad (6.8)$$

Equations 6.6 and 6.8 will reveal a great deal of information about single-layer overlays provided values can be obtained for k and λ. A value for k can be obtained by combining equation 6.3 with the model for single-bead dilution (see equation 2.2 – page 10) proposed by Bednarz (1996) and reported in Francis *et al.* (1998). An estimate for λ, the area fraction of overlap, is more difficult to obtain. It is helpful, however, to consider how λ may vary as a function of the bead overlap, ϕ. Bead overlap is normally defined in terms of the single-bead width, w, and the step-over or offset between adjacent weld beads, δ. The bead overlap is given by:

$$\phi = 1 - \frac{\delta}{w} \quad , \quad 0 \leq \phi \leq 1 \quad \ldots\ldots\ldots \quad (6.9)$$

If the step-over is equal to the bead width then the overlap, ϕ, is zero. It can be appreciated that if the overlap is equal to zero there can be no area fraction of overlap. Thus one boundary condition for $\lambda = \lambda(\phi)$ becomes:

$$\lambda(0) = 0 \quad \ldots\ldots\ldots \quad (6.10)$$

If the step-over is zero, the overlap, ϕ, is equal to unity. This condition is equivalent to depositing one bead directly on top of its predecessor. One would not expect any

additional or new substrate to be melted under these circumstances. Consequently, the substrate fraction, defined by equation 6.1 is equal to zero at 100% overlap, *i.e.*:

$$1 - k - \lambda = 0$$

This relationship can be rearranged to provide the other boundary condition for $\lambda = \lambda(\phi)$.

$$\lambda(1) = 1 - k \quad \ldots\ldots\ldots \quad (6.11)$$

Equations 6.10 and 6.11 provide the end conditions for the unknown function $\lambda = \lambda(\phi)$. A first order approximation to the function is a straight line between the two end points, *i.e.*:

$$\lambda = \phi(1 - k) \quad \ldots\ldots\ldots \quad (6.12)$$

Equation 6.12 satisfies both end-conditions and, together with equations 6.3, 6.6 and 6.8, provides a simple model for multi-pass overlays.

6.3 STEADY-STATE DILUTION FOR λ LINEAR WITH ϕ

One parameter of interest is the predicted steady-state dilution. Consider an overlay in which N beads have been deposited. The average dilution of the overlay can be written in terms of the total material that is deposited and the total material that is melted. If assumptions 2 and 3 apply, the average dilution, D_{av}, can be written as:

$$D_{av} = \frac{A(1-k) + A(N-1)(1-k-\lambda)}{NkA + A(1-k) + A(N-1)(1-k-\lambda)}$$

where A is the total cross-sectional area of a bead, and is assumed to be the same for all beads in the overlay. As N becomes large this expression approaches the value:

$$D_{av} = \frac{1 - k - \lambda}{1 - \lambda} \quad \ldots\ldots\ldots \quad (6.13)$$

which is an estimate for the steady-state dilution of an overlay. A physical interpretation of this result can be derived by referring to Figure 6.1 (page 107). The numerator of equation 6.13 refers to the substrate fraction, *i.e.* the fraction of the bead contributed by new or previously unmelted substrate. The denominator represents the entire bead minus the component contributed by overlap with the previous bead. Thus equation 6.13 states that the steady-state dilution of an overlay is independent of how much of the previous bead is melted. All that matters is the ratio of material deposited in each pass to the amount of new substrate melted under steady conditions.

6.4 RATE OF CONVERGENCE FOR λ LINEAR WITH ϕ

Consider the deposition of a multi-pass overlay. Let the welding consumable produce an all-weld-metal deposit containing 25wt.% chromium and let the base material be a mild steel containing no chromium. Suppose that the welding conditions are such that a single-bead deposit would have a dilution, D_{sb}, of 50% and that the overlap, ϕ, is also 50%. Thus k will have a value of 0.5 (the complement of the single-bead dilution) and λ will assume a value of 0.25 as required by equation 6.12. Equation 6.6 predicts the chromium concentrations for each bead in the overlay, and the first few results are plotted in Figure 6.2. It can be seen that the chromium concentrations will first assume the value for a single-bead deposit (bead no. 1) and then converge to the steady-state

value, given by equation 6.8, of 16.7%. The steady-state dilution, given by equation 6.13, is 33%.

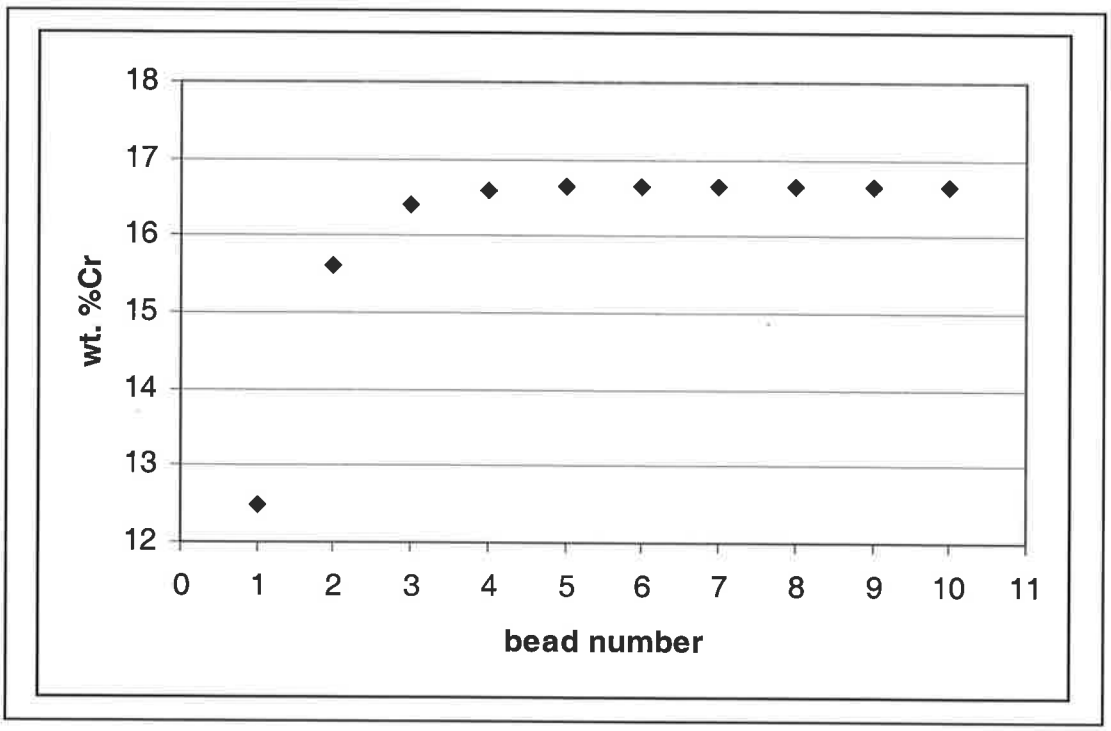

Figure 6.2: - An example of a convergence pattern for chromium concentration as predicted by the k-λ model. The chromium concentration in an all-weld-metal deposit was assumed to be 25wt.%, while the substrate was assumed to be chromium-free. It was assumed that the welding conditions would produce a single-bead deposit with 50% dilution. The overlap was also assumed to be 50%.

The form of equation 6.6 suggests that the rate at which the composition converges is independent of k and dependent only on λ. In practical situations λ will vary between 0 and 0.5; λ will be equal to zero when the overlap is zero and, at the other extreme, λ = 0.5 corresponds to one 50%-dilution single bead being deposited directly on top of another. Figure 6.3 shows the convergence trend for low, moderate and high values of λ. Equation 6.8 predicts steady-state chromium concentrations of 12.6%, 16.7% and 25% for λ = 0.01, 0.25 and 0.5 respectively. In all cases it was assumed that k = 0.5 and

that the welding consumable would produce an all-weld-metal deposit containing 25wt.% chromium. It can be seen that when $k + \lambda = 1$, as is the case here when $\lambda = 0.5$, the overlay composition will converge to the all-weld-metal composition.

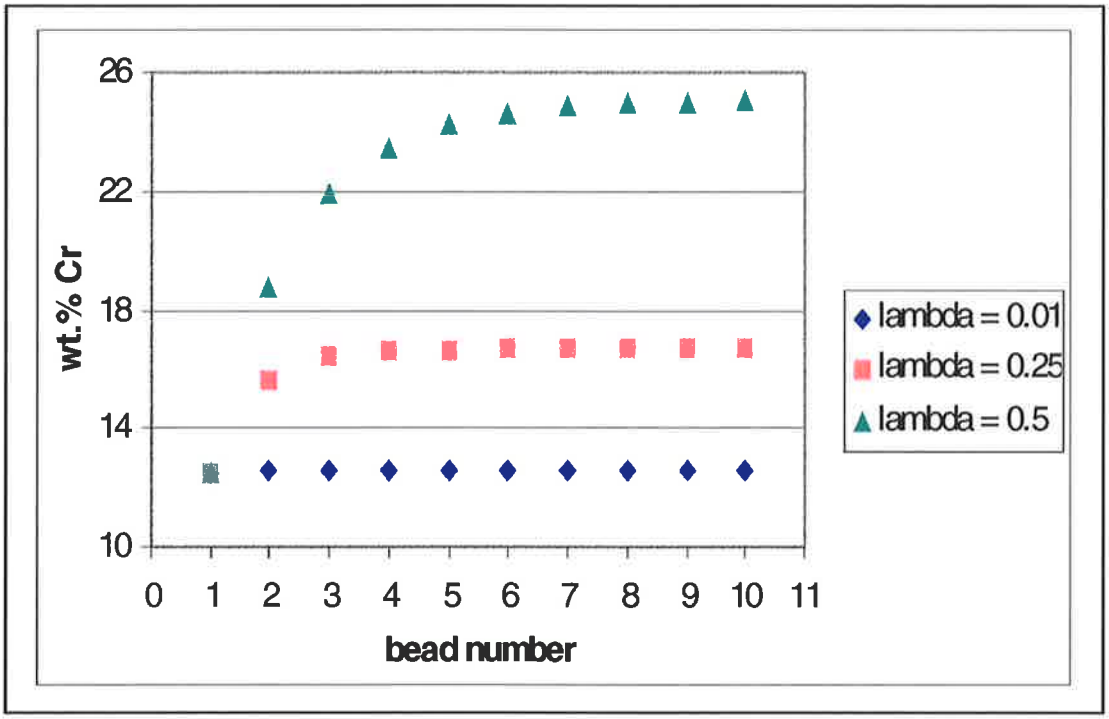

Figure 6.3: - Chromium concentration vs bead number for three different values of λ. The rate of convergence appears to decrease as λ increases. The chromium concentration in an all-weld-metal deposit was assumed to be 25wt.%. The substrate was assumed to contain no chromium. It was assumed that the welding conditions would produce a single-bead deposit with 50% dilution.

Let it be assumed that a steady-state condition has effectively been reached when the composition has reached a value 95% of the way from the single-bead composition to the steady-state composition. That is to say if:

$$\lambda + \lambda^2 + \lambda^3 \ldots\ldots \geq 0.95\left[\frac{1}{1-\lambda} - 1\right] \quad \ldots\ldots \quad (6.14)$$

then a steady state is assumed to have been reached (see equations 6.6 and 6.7). It can be seen from Table 6.1 that when $\lambda = 0.01$ convergence occurs after only two beads have been deposited. At the other extreme, it is necessary to deposit six beads in order to achieve convergence when $\lambda = 0.5$. To a first order approximation λ is directly proportional to bead overlap. Consequently, this model suggests that at low overlaps convergence occurs almost immediately but, as the overlap increases, more beads need to be deposited for convergence to occur.

λ	Value At Which Convergence Is Deemed To Have Been Achieved (see ineq. 6.14)	Value of Sum					
		Bead 1	Bead 2	Bead 3	Bead 4	Bead 5	Bead 6
0.01	0.010	0.000	0.010	0.010	0.010	0.010	0.010
0.25	0.317	0.000	0.250	0.313	0.328	0.332	0.333
0.40	0.633	0.000	0.400	0.560	0.624	0.650	0.660
0.50	0.950	0.000	0.500	0.750	0.875	0.938	0.969

Table 6.1: - The value of the sum $1 + \lambda + \lambda^2 + \lambda^3 + \ldots\ldots - 1$ is given as a function of bead number for various λ. The value at which the sum is deemed to have reached a steady state is also given for comparison.

An explanation for the effect of λ on the rate of convergence is given here. The first bead in a multi-pass overlay is unique in that it is deposited in the same manner as a single-bead deposit. It will have a higher dilution than all other beads in the overlay

since, in the first pass, the welding consumable is diluted by substrate material alone. All other beads overlap with their predecessors. The first bead, however, influences subsequent beads in the overlay because part of the first bead is melted and mixed into the second bead. Part of the second bead is then melted and mixed into the third bead *etc*. Each bead in the overlay is thus mixed, to some extent, with the first (high-dilution) bead. In fact, under the conditions described in section 6.2.2, the fraction of the first bead mixed into the N^{th} bead in the overlay will be λ^{N-1}. It can be seen that, as λ decreases, the influence of the first bead will decay more rapidly, resulting in faster convergence to the steady-state condition.

6.5 A SPREADSHEET FOR PREDICTING DILUTION IN MULTI-PASS OVERLAYS

It is possible, using the theory developed in sections 6.2 to 6.4, to establish a link between the selected welding parameters and the composition of an overlay. In the Australian hardfacing industry, 2.8mm diameter electrodes are preferred together with the direct-current, electrode-positive (DCEP) configuration. The larger consumable diameter facilitates a higher deposition rate and, due to the desirable metal transfer characteristics, most consumables are designed for DCEP operation. As for single-bead deposits, down-hand deposition is the preferred mode of operation and, consequently, this analysis applies to this configuration. This leaves voltage, V, current, I, work distance, l, and travel speed, S at the discretion of the operator. Once these variables have been selected the step-over, δ, is immediately defined in that the specified overlay height has been pre-determined by the end-user. There will be only one step-over that achieves the specified overlay height and that can be determined using equation 5.5 (page 98).

For a given combination of voltage, current, work distance and travel speed it is possible to estimate the single-bead dilution using equation 2.2 (page 10). If the conditions and assumptions described in section 6.2.2 apply, the calculated single-bead dilution can be used to estimate k, the deposited fraction of the bead. All that remains is to estimate λ.

A first approximation to λ is obtainable from equation 6.12 in terms of k, already known, and the overlap, ϕ. The bead overlap is a function of the bead width and the step-over. The step-over is obtained from equation 5.5 (page 98) and the bead width from equation 3.4 (page 44) so that λ can also be estimated. A summary of the algorithm is presented here. The relevant equation numbers are included in parentheses.

SUMMARY OF ALGORITHM

1. *Select V, I, l, S and desired steady state overlay height,* H_{ss}.
2. *Calculate W from* $W = aI + bII^2$ (2.4)
3. *Calculate* δ *from* $\delta = \dfrac{W}{\rho H_{ss} S}$ (5.5)
4. *Estimate w from* $w = \dfrac{C_1}{S} + C_2 VI$ (3.4)
5. *Estimate* ϕ *from* $\phi = 1 - \dfrac{\delta}{w}$ (6.9)
6. *Calculate* D_{sb} *from* $\dfrac{D_{sb}}{1 - D_{sb}} = \alpha \dfrac{VI}{W}(1 + \beta VIS)$ (2.2)
7. *Calculate k from* $k = 1 - D_{sb}$ (6.3)
8. *Estimate* λ *from* $\lambda = \phi(1 - k)$ (6.12)
9. *Calculate % Cr etc. at steady state from equation* (6.8), *i.e.*:

$$[x]_{ss} = [x]_{bm} + \frac{k}{1 - \lambda}\left([x]_{awm} - [x]_{bm}\right)$$

Thus for any combination of V, I, l and S it is possible to predict the resulting overlay composition. The predicted composition will not, however, indicate whether the selected parameters are optimal. (In many instances minimum dilution is the objective

and the optimal settings would be those that give minimum dilution or the richest overlay composition.) Consequently, it becomes necessary to compare a range of settings in order to identify conditions that are near-optimal. When this need is combined with the complexity of the algorithm the problem becomes amenable to a spreadsheet program. In a spreadsheet it is possible to change the input parameters and receive instant output. In addition, several sets of conditions can be entered and compared simultaneously. If the user wishes, a matrix of conditions can be entered and the data set can be ranked in order from the richest to leanest overlay (lowest to highest dilution) for the height specified. Optimum conditions are then readily identified. An example of the original spreadsheet program arising from the current work is shown in Figure 6.4. This spreadsheet was generated for consumable B (see section 3.2).

voltage	current	speed (m/s)	work dist (m)	width (m)	D_{sb}	k	step (m)	overlap	λ	hr/m^2	%Cr
28	400	0.0150	0.04	0.011	0.51	0.49	0.0038	0.66	0.34	4.89	20.62
30	350	0.0067	0.04	0.014	0.52	0.48	0.0070	0.50	0.26	5.91	18.16
32	350	0.0100	0.03	0.013	0.57	0.43	0.0042	0.68	0.39	6.59	19.62
26	250	0.0050	0.02	0.010	0.55	0.45	0.0049	0.50	0.27	11.26	17.39

Figure 6.4: - The first spreadsheet for 5mm high overlays. It was assumed that an all-weld-metal deposit would contain 25 wt.% chromium. The base material was assumed to be chromium-free.

It can be seen that the spreadsheet has a column headed "hr/m^2". This column contains an estimate of the minimum time required to cover a square metre of the substrate material and is based only on the estimated deposition rate. It also highlights the fact that the deposition time affects labour costs and will influence the selection of parameters.

6.5.1 Generating a Spreadsheet.

It is only possible to generate a spreadsheet for a particular welding consumable if it has been properly characterised. There are two deposition rate constants (a and b), two parameters for single-bead dilution (α and β) and two for bead width (C_1 and C_2), all of which must be known for the consumable. Consequently, it is necessary to deposit at least two single beads-on-plate and to measure the width, dilution and deposition rate for each deposited bead. Each bead must be deposited under different welding conditions. Once these data are obtained it is necessary to fit the results to the respective equations to obtain values for the required constants. The spreadsheet can be constructed as soon as these data are available.

Historically, the spreadsheet was put to immediate use. However inconsistencies were found, and they led to the following detailed examination.

6.6 COMPARISON WITH EXPERIMENTS

Eight overlays were deposited on mild steel substrates. The substrates were 25mm thick, and typically 75mm wide and 350mm long. Each overlay contained between six and twelve beads depending on the rate of convergence to a steady state. The nominal steady-state heights of the overlays ranged from 2 to 6mm. For each overlay, a matching single bead was deposited so that data were available for the single-bead dilution and width.

The general aim was to cover a diverse set of operating conditions within a manageable number of samples. At a height of 4mm, both low and high overlap conditions were used. These two overlays were deposited at ambient temperature and then again with an inter-pass temperature of 400°C. Two different welding consumables were used

throughout the experiments, although in both cases they were high-chromium, high-carbon type electrodes.

The contact tip-to-work voltage and current were recorded for every pass with the CSIRO welding monitor (Dick, 1991) described in section 3.2. The wire feed rates were recorded with a hand-held wire feed meter. Inter-pass temperatures were recorded by inserting K-type thermocouples into drilled holes in the substrate. The holes were drilled from the reverse side to a depth of 20mm, so that the measurement points were within 5mm of the substrate surface. Another value for inter-pass temperature was obtained by measuring surface temperature with a K-type surface temperature probe. The values obtained from surface measurement were found to agree well with those measured below the substrate surface, although the surface temperature was usually slightly lower due to faster cooling. A summary of the deposition conditions is given in Table 6.2.

Each overlay and single bead was sectioned so that a slice approximately 10mm in thickness was produced. These slices were surface ground and etched with 10% Nital so that the interfaces between the steel substrate and the deposit would be clearly revealed. For the single-bead deposits dilutions were measured by first placing the sample on an optical projector with 10:1 magnification. Each profile was then traced with high quality tracing paper. The profiles were then carefully cut out and weighed so that the dilutions could be determined from the ratio of the weights. For the larger overlay samples, the slices were scanned and recorded in a *TIFF* file format. Magnified images could then be printed and the penetrations measured. The average penetrations were typically measured across four beads in the deposit, from the fifth-last bead to the penultimate

bead. This ensured that the steady-state penetration, not the transient penetration, was measured.

Experimental Plan								
Sample No	Sample Type	WFS (m/min)	Volts	Amps	WD (mm)	Speed (mm/min)	Step-over (mm)	IP Temp (°C)
A	2mm pad	2.26	28.0	380	20	900	6.0	Room
B	3mm pad	2.86	28.2	330	40	730	6.0	Room
C	4mm pad	2.67	28.4	360	30	400	8.0	Room
D	4mm pad	2.77	28.3	360	30	400	8.0	400
E	4mm pad	2.74	28.1	380	30	800	4.0	Room
F	4mm pad	2.74	28.1	370	30	800	4.0	400
G	5mm pad	3.13	27.8	370	30	550	5.0	Room
H	6mm pad	3.81	29.9	440	40	400	8.0	Room

Table 6.2: - The experimental plan for eight overlay samples. Two 2.8mm diameter consumables, equivalent to consumables A and B (see section 3.2), were used to deposit these overlays. Inter-pass temperatures are quoted to the nearest 25°C.

In some instances the currents and voltages for corresponding single-bead and overlay deposits differed. For example, as a welding power source warms up, higher currents can sometimes be drawn even if the settings remain unchanged. Such an effect could introduce errors to the predictions of the k-λ model. (The model requires values for the single-bead dilution under welding conditions that are identical to those used in the corresponding multi-pass overlay.) To allow for this type of effect all of the measured single-bead widths and dilutions were normalised to the average current, voltage and deposition rate readings for the corresponding multi-pass overlay. The normalised single-bead dilutions, D_n, were obtained by adapting the Bednarz-Deam model (see equation 2.2 – page 10), reported in Francis *et al.* (1998), and were given by:

$$\frac{D_n}{1 - D_n} = \frac{\alpha \dfrac{V_{ov} I_{ov}}{W_{ov}} \left(1 + \beta V_{ov} I_{ov} S\right)}{\alpha \dfrac{V_{sb} I_{sb}}{W_{sb}} \left(1 + \beta V_{sb} I_{sb} S\right)} \times \frac{D_{sb}}{1 - D_{sb}}$$

where the subscript *ov* denotes an average value of the parameter in the overlay and the subscript *sb* denotes an average value for the matching single-bead deposit. The normalised bead widths, w_n, were obtained using a similar procedure with equation 3.4:

$$w_n = \frac{\dfrac{C_1}{S} + C_2 V_{ov} I_{ov}}{\dfrac{C_1}{S} + C_2 V_{sb} I_{sb}} \times w_{sb}$$

A summary of the results is given in Table 6.3. Equation 6.13 (page 112) was used to predict the steady-state dilution. The steady-state penetration can be estimated if both the steady-state dilution and height are known. Penetration was used as the basis for all comparisons as it is the most sensitive indicator of the accuracy of a model.

Sample	Height, mm	Overlap	Inter-pass Temperature, (°C)	D_n	Predicted λ (linear)	Penetration, mm	
						Predicted	Measured
A	2.0	0.48	Room	0.59	0.28	1.5	2.0
B	3.0	0.44	Room	0.48	0.21	1.5	1.5
C	4.3	0.50	Room	0.49	0.24	2.1	1.8
D	4.1	0.55	400	0.55	0.30	2.2	2.1
E	4.3	0.65	Room	0.49	0.32	1.4	0.9
F	4.3	0.69	400	0.59	0.40	1.9	1.3
G	5.2	0.62	Room	0.49	0.30	1.9	1.3
H	6.1	0.52	Room	0.45	0.24	2.4	1.7

Table 6.3: - A summary of results for the *k*-λ model. The penetration refers to the average penetration of the overlay under steady-state conditions.

It is evident, from the results in Table 6.3, that a closer examination is required. The penetration is underestimated for the 2mm overlay and overestimated for overlays 5-6mm in height. The apparent dependence of average penetration on overlay height leads to the conclusion that the influence of overlay geometry may need investigation.

6.7 AN EMPIRICAL CORRECTION

A section through the 2mm high overlay sample was examined. One of the features of the penetration profile of a 2mm overlay can be seen in Figure 6.5. Eight beads were deposited in this overlay and the figure shows that there are also eight peaks in the penetration profile. It appears that as each subsequent bead is deposited a new peak in the penetration profile is created. For higher overlays this feature is often not present (see Figure 6.6). Thus, as a 2mm overlay is deposited, the melting front at the bottom of the weld pool must punch through the fusion line of the previous bead to create its own peak. Figure 6.7 illustrates how this punch-through effect results in more substrate being melted than equation 6.12 predicts and, therefore, how λ may be overestimated. The effect is pronounced when a thin overlay is deposited and the overlap is moderate to low. (It should be noted that low overlaps are generally required when depositing thin layers to ensure that the specified overlay height is not exceeded.)

For higher overlays the punch-through effect is generally not observed and in fact λ tends to be underestimated. In order to deposit a high overlay it is usually necessary to have a moderate-to-high overlap so that sufficient build-up of material is achieved. The combination of a high overlay and high bead overlap generally ensures that the current path between the tip of the electrode and the previous bead is somewhat shorter than the

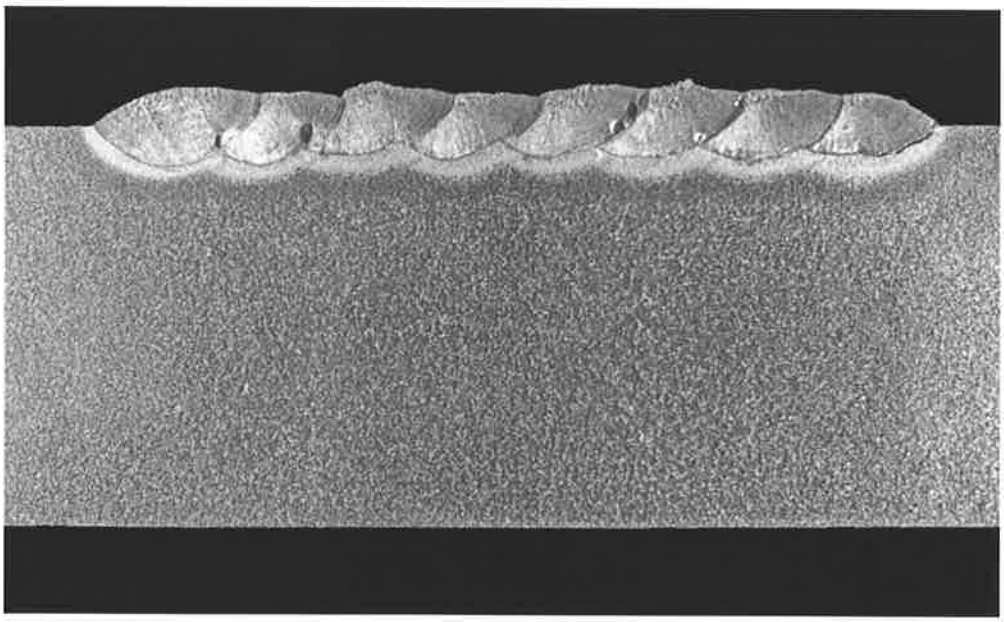

Figure 6.5: - The penetration profile for a 2mm overlay (sample A in Tables 6.2 and 6.3). As each subsequent bead is deposited a new peak in the penetration profile is created. Deposition proceeded from right to left.

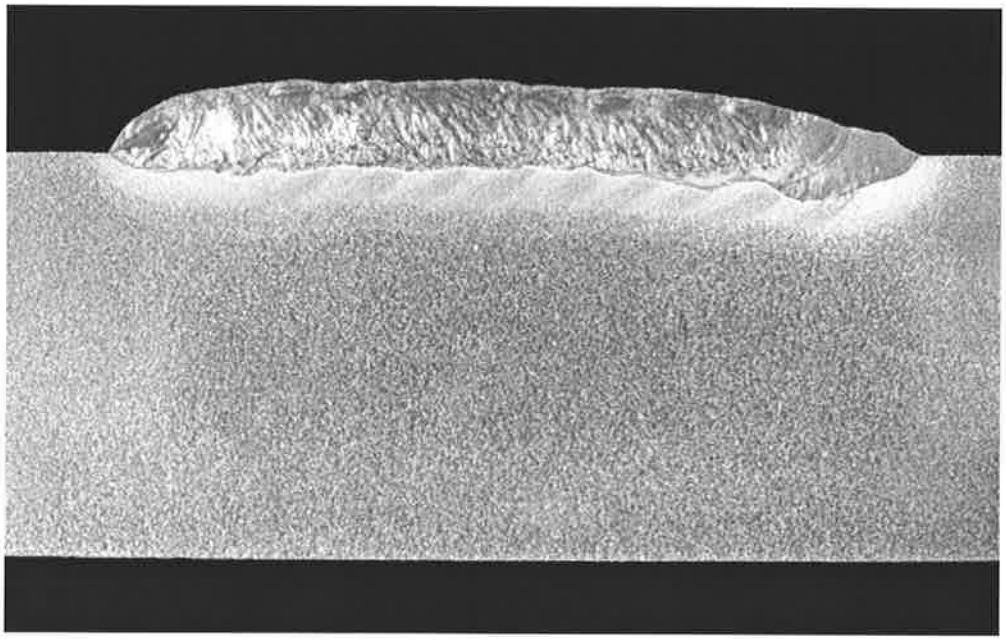

Figure 6.6: - The penetration profile for a 4mm overlay with high bead overlap (sample E in Tables 6.2 and 6.3). In this case the individual penetration peaks are not clearly visible. Deposition proceeded from right to left, and it can be seen that the penetration of the first bead is higher than the steady-state penetration of the overlay.

path between the electrode and the substrate. Arc impingement and melting are thus biased toward the previous bead, causing λ to assume a value that is higher than equation 6.12 predicts.

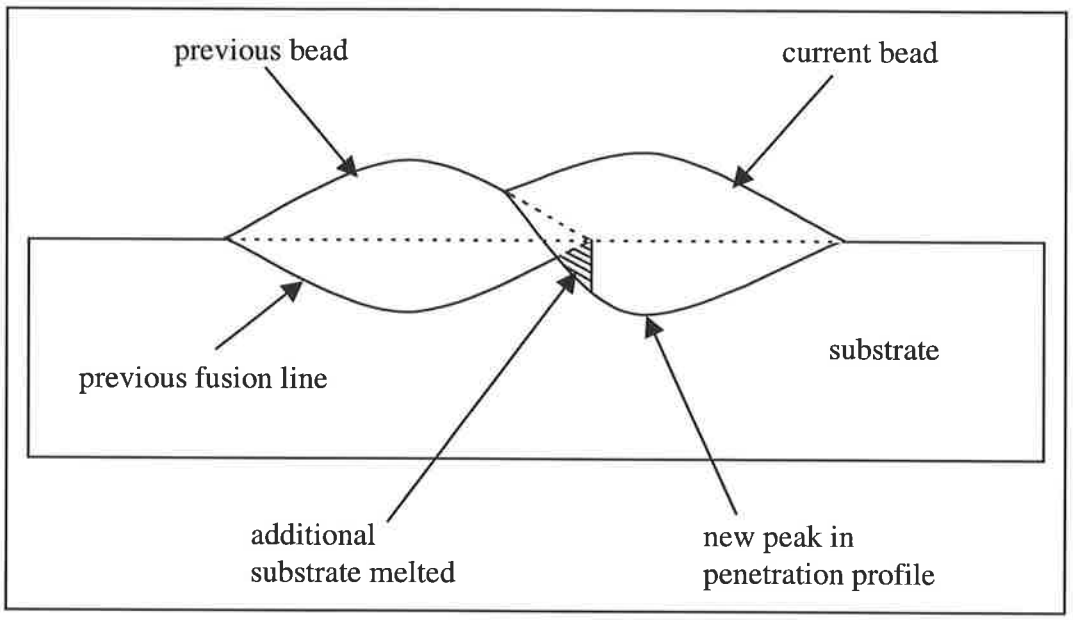

Figure 6.7: - Schematic representation of the punch-through effect in thin overlays. The fusion line of the current bead has "punched through" the fusion line of the previous bead to melt additional substrate material and create a new peak in the penetration profile. Deposition is proceeding from left to right.

Having identified how λ may deviate from the values predicted by equation 6.12 it becomes possible to identify a suitable empirical correction. Equation 6.12 is a first order approximation; a straight line between two known end-points. Since the end-points are known to be correct, the correction must be such that it does not change the value of λ at the end-points. The general form for such a correction is presented here:

$$\lambda = \phi(1-k) + a_1\phi(1-\phi)(H_{ss} - a_2)(1-k)$$

where H_{ss} is the steady-state overlay height in millimetres and a_1 and a_2 are fitted constants. The correction term is a quadratic function in ϕ that maintains the end-point conditions. The (H_{ss} - a_2) component introduces a transition height (a_2) below which λ is lower than the value predicted by equation 6.12 and above which it is higher. The least-squares best fit to the data in Table 6.3 is:

$$\lambda = \phi(1-k) + 0.254\,\phi(1-\phi)(H_{ss} - 3.23)(1 - k) \ldots\ldots \quad (6.15)$$

Thus the fitted transition height is 3.23mm. The experimental data are compared to the fitted results in Table 6.4. The fit for λ is a least-squares best fit based on the error in steady-state penetration. It can be seen that there is a significant reduction in the discrepancies between the measured and predicted penetrations. The empirical correction reduces the inaccuracy that is seen at the extremes of the height range, and achieves an acceptable level of accuracy over the range of 2–6mm. Most single-layer overlays deposited in practice would fall in the range of 2–6mm.

It should be remembered that the analyses described in sections 6.2 to 6.5 were based on the assumption that λ will have the same value for all beads in a multi-pass overlay. The height of a multi-pass overlay, however, changes from that of a single-bead deposit (*i.e.* the first bead) to the steady-state height. It would therefore appear that λ will assume an initial value (corresponding to the second bead in the overlay) and then converge to a steady-state value as subsequent beads are deposited. Equation 6.15 is a least-squares best fit to the steady-state value of λ and it is anticipated that, with the inclusion of the empirical correction, the k-λ model will accurately predict the steady-state dilution for a

wide range of welding conditions. It is expected that the analyses described in earlier sections will serve as useful illustrations, and that the observed trends will still apply.

Sample	Height, (mm)	Overlap	Inter-pass Temperature, (°C)	D_{sb}	λ (linear)	λ (fitted)	Penetration, mm	
							Predicted	Measured
A	2.0	0.48	Room	0.59	0.28	0.24	1.7	2.0
B	3.0	0.44	Room	0.48	0.21	0.21	1.6	1.5
C	4.3	0.50	Room	0.49	0.24	0.28	1.8	1.8
D	4.1	0.55	400	0.55	0.30	0.33	2.0	2.1
E	4.3	0.65	Room	0.49	0.32	0.35	1.2	0.9
F	4.3	0.69	400	0.59	0.40	0.44	1.5	1.3
G	5.2	0.62	Room	0.49	0.30	0.36	1.3	1.3
H	6.1	0.52	Room	0.45	0.24	0.32	1.5	1.7

Table 6.4: - Results from the k-λ model after an empirical correction was incorporated. The linear values of λ were obtained from equation 6.12 (page 111). The fitted values of λ were obtained from a least-squares best fit to equation 6.15.

6.8 REFINEMENT OF THE MODEL

In sections 6.2 to 6.6 the variables k and λ were assumed to remain constant, for a given set of welding conditions, from the first and second beads respectively until a steady-state condition was reached. In the previous section, however, it was suggested that λ could change as the overlay converges to the steady-state condition. In the transient region the composition of each successive bead will be different and so will be the thermal properties. Consequently k (which is dependent on thermal properties) may change too.

One parameter that is unlikely to vary significantly is the cross-sectional area of material deposited in each bead. In section 6.3 it was found that this parameter and the quantity of additional substrate melted per pass, under steady conditions, define the steady-state dilution. Thus, the k-λ model revealed that analysing the beads in terms of their contributing area fractions was a valid approach, but also demonstrated that the choice of variables may not have been optimal. An analysis of multi-pass overlays is now presented in terms of the parameters that determine the steady-state dilution.

6.8.1 A New Variable, γ

Consider the case where a multi-pass overlay is being deposited. Each bead is deposited with identical welding parameters and a steady-state condition has been reached. With each pass a certain repeating cross-sectional area of substrate material is being melted. Let that repeating area be denoted by $A_{s(ov)}$ (see Figure 6.8). Consider also the deposition of a single bead with the same welding parameters. For the single bead a greater area of substrate, $A_{s(sb)}$, will be melted.

Let γ be defined by the following relationship:

$$\gamma = \frac{A_{s(ov)}}{A_{s(sb)}} \quad \ldots\ldots \quad (6.16)$$

Thus γ is the area of substrate melted per pass in an overlay under steady-state conditions, as a fraction of that melted in a matching single bead. This definition for γ will be seen to be very useful.

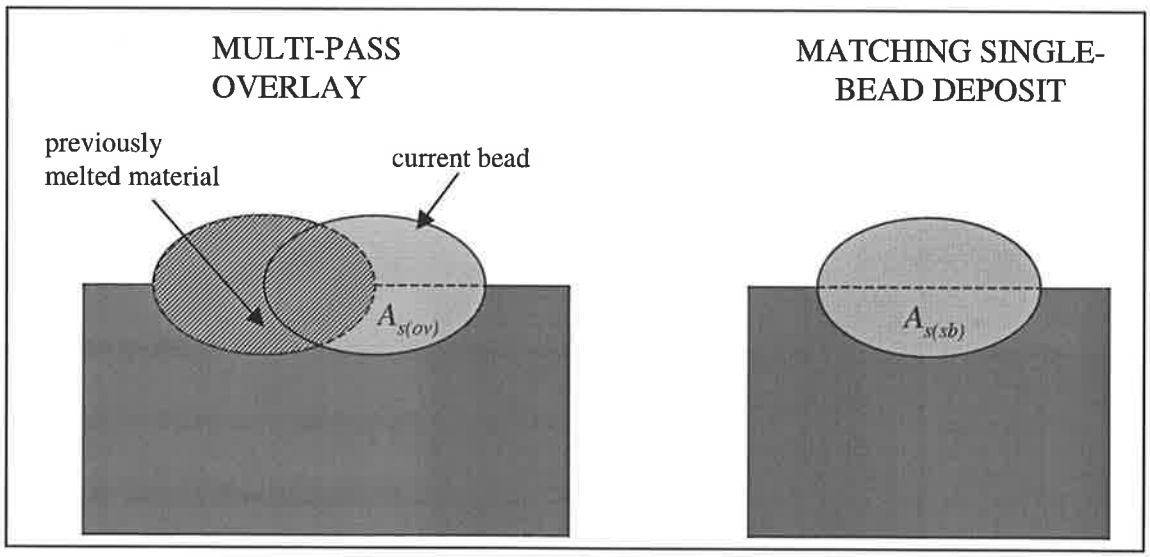

Figure 6.8: - A schematic representation of the repeating area of substrate, $A_{s(ov)}$, that is melted in each pass under steady-state conditions. $A_{s(sb)}$ represents the area of substrate that would be melted if a single bead were to be deposited under identical welding conditions.

6.8.2 Dilution of an Overlay

The cross-sectional area of material deposited in a single bead, A_d, is given by:

$$A_d = \frac{W}{\rho S} = A\left(1 - D_{sb}\right) \quad \ldots\ldots\ldots \quad (6.17)$$

where: W = deposition rate,

ρ = density of an all-weld-metal deposit,

S = travel speed,

A = cross-sectional area of the entire bead, and

D_{sb} = single-bead dilution $\quad (0 < D_{sb} < 1)$

Rearranging gives the total cross-sectional area of the bead:

$$A = \frac{W}{\rho S} \frac{1}{\left(1 - D_{sb}\right)}$$

For a single bead the area of melted substrate, $A_{s(sb)}$, is given by the product of the total bead area and the single-bead dilution:

$$A_{s(sb)} = \frac{W}{\rho S}\frac{D_{sb}}{1 - D_{sb}} \quad \cdots\cdots\cdots (6.18)$$

Now, using the definition for γ an expression can be written for the repeating area of substrate melted, $A_{s(ov)}$, under steady-state conditions in a multi-pass overlay:

$$A_{s(ov)} = \frac{W}{\rho S}\gamma\frac{D_{sb}}{1 - D_{sb}}$$

This area is repeated every step-over, δ, and dividing the repeating area by the step-over will give the average penetration of an overlay under steady-state conditions, P_{ss}:

$$P_{ss} = \left(\frac{W}{\rho S \delta}\right)\gamma\frac{D_{sb}}{1 - D_{sb}} \quad \cdots\cdots\cdots (6.19)$$

If the term in brackets is compared with equation 5.5 it can be seen that this term is equivalent to the steady-state overlay height. Thus, equation 6.19 can be rewritten:

$$P_{ss} = H_{ss}\,\gamma\frac{D_{sb}}{1 - D_{sb}} \quad \cdots\cdots\cdots (6.20)$$

Equation 6.20 can then be substituted into equation 5.1 (page 93), together with the steady-state overlay height, H_{ss}, to provide the steady-state dilution of an overlay, D_{ov}:

$$D_{ov} = \frac{\gamma D_{sb}}{\gamma D_{sb} + 1 - D_{sb}} \quad \cdots\cdots (6.21)$$

Unfortunately, γ is a complicated function of thermal properties, geometry and other parameters such as inter-pass temperature. The challenge in analysing single-layer multi-pass overlays is to identify a working approximation for the function for γ.

The end-points for the function were considered. When the overlap is zero each weld pass will melt an amount of substrate that is equal to the amount melted in a single-bead deposit, *i.e.*:

$$\gamma(0) = 1$$

However, when the overlap is 100% one would not expect any new substrate material to be melted:

$$\gamma(1) = 0$$

Thus, a first-order approximation to the function for γ is:

$$\gamma = 1 - \phi$$

An empirical correction was incorporated in the same way as for λ. The general form chosen for the correction was:

$$\gamma = 1 - \phi - \mathrm{b}_1 \phi (1 - \phi)(H_{ss} - \mathrm{b}_2)$$

where H_{ss} is the steady-state overlay height in millimetres and b_1 and b_2 are fitted constant terms. The least-squares best fit to the results for the eight overlays described in Table 6.3 was:

$$\gamma = 1 - \phi - 0.254\, \phi (1 - \phi)(H_{ss} - 3.23) \quad \ldots\ldots \quad (6.22)$$

It can be seen that, with this form of expression for γ, the model is mathematically equivalent to the k-λ model. However, the overlay dilution is now stated in terms of a variable that has fundamental significance.

6.9 SUMMARY

A model has been developed for open-arc weld deposition of high-chromium white iron overlays. The model is based on the definition of two new variables, and the concept that a bead in a multi-pass overlay should be thought of in terms of its contributing fractions. The first variable is the area fraction of deposited material, k, and the second is the area fraction of overlap, λ.

In deriving the k-λ model is was assumed that:

- any differences between the thermal and physical properties of the overlay and base material could be ignored, and that
- k would remain unchanged from the first bead and λ would remain unchanged from the second bead until a steady-state condition was reached.

A corollary of the latter assumption is that k and λ are independent of the height of the overlay. (k and λ were assumed to remain constant despite the requirement that the overlay height change from that of a single-bead deposit to the steady-state overlay height.) Comparisons with experiments, however, revealed that λ does vary with the overlay height. An empirical correction was successful in allowing the model to predict the steady-state dilution of an overlay with reasonable accuracy. The model adequately describes the data for two different high-chromium, high-carbon welding consumables

and it is anticipated that it will generally describe the data for similar consumables. The model may also be applicable to other alloy systems.

An algorithm for determining the steady-state overlay composition for a given set of welding parameters has been outlined. A spreadsheet for predicting overlay compositions is also described. The spreadsheet allows any combination of welding parameters to be compared and near-optimum conditions can now be readily identified. The spreadsheet has been developed and distributed to many interested parties in the Australian hardfacing industry. The current format of the spreadsheet and examples of the output it produces are included in Appendix 1.

The model suggests that, as the overlap increases, more beads need to be deposited before a steady-state condition is reached. It also reveals that the steady-state dilution is independent of the amount of the previous bead that is melted, and dependent only on the steady-state mixing ratio of material deposited to new substrate melted in each pass. Consequently, the model has been redefined in terms of a single new variable γ; a variable that has fundamental significance.

7

A GEOMETRIC SOLUTION FOR MULTI-PASS OVERLAYS

7.1 INTRODUCTION

In the previous chapter it was seen that, by making an empirical correction for geometric effects, significant improvements could be made to the k-λ model. It may therefore be possible to achieve further improvements by developing a model that reconstructs the geometry of an overlay.

A new model is developed here. It is based on the assumption that both the bead profile and the fusion line can be modelled by parabolic functions. A parabola is a sensible choice as it has already been found to give accurate representations of single-bead profiles at moderate-to-high travel speeds (see section 3.5). Figure 2.3 (page 19) also showed that the profile of the fusion line, as calculated for a distributed source of heat in the absence of weld pool convection, is approximately parabolic. Another advantage of the parabolic function is that it is mathematically convenient. There are only two independent coefficients to be determined, and the integration of a parabolic function is straightforward.

7.2 THE STEADY-STATE BEAD PROFILE

The overlays and single beads that were deposited for the k-λ model (see section 6.6) were closely examined. An interesting observation was made in that, when depositing

each multi-pass overlay, the bead width did not change significantly from that of the matching single-bead deposit. The bead width in each overlay was measured on a straight line from the toe of the last bead to the point on the previous bead surface where melting commenced (see Figure 7.1). The beads were generally much wider than they were high and, in each overlay, the difference between the measured bead width and the projected bead width was found to be small. (The projected bead width is the width of a bead in the overlay projected down on to the plane of the substrate surface.) In order to simplify the analysis it will be assumed that, when depositing a multi-pass overlay, the projected bead width remains constant and equal to the single-bead width.

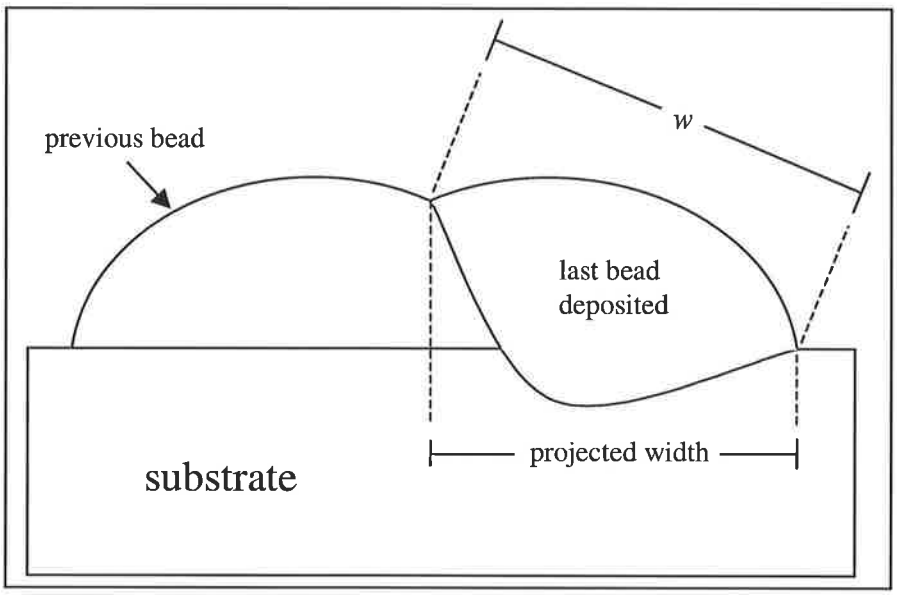

Figure 7.1: - The measurement of the true bead width, *w*, and the projected bead width for a bead in a multi-pass overlay.

Two constraints are needed to define a parabolic function. One has been provided by assuming that the projected bead width remains unchanged. The other constraint is provided by the principle of conservation of mass. Each time a bead is deposited the

correct area, A_d, must be added to the cross-sectional area of the overlay. Figure 7.2 is a schematic representation of the basis for the analysis.

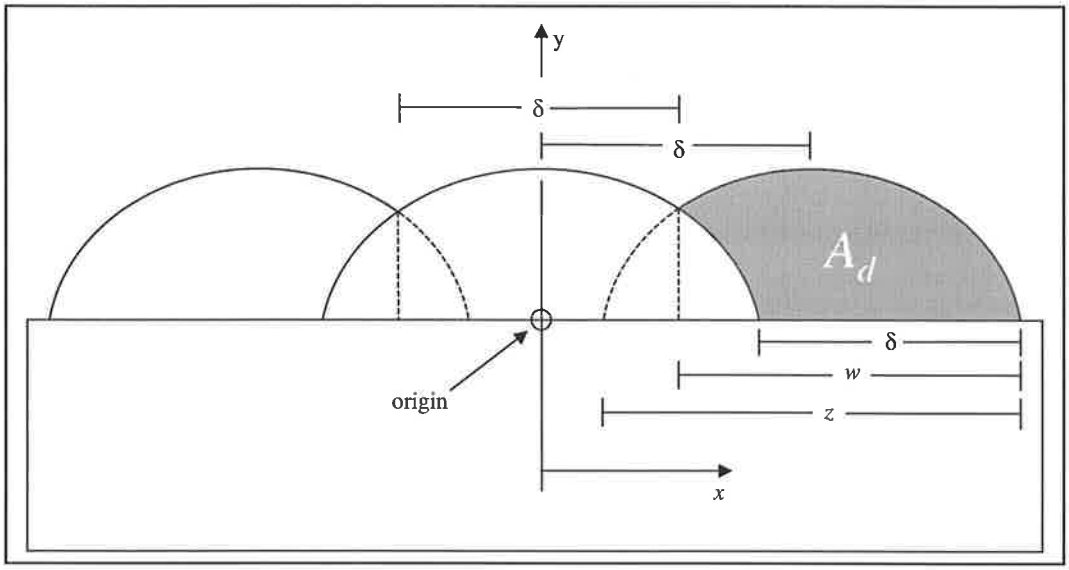

Figure 7.2: - Coordinate system for bead profile analysis. Note that the projected bead width is assumed to be equal to the single-bead width, w.

By observing the symmetry, the effective width of each parabola, z, can be seen to be given by:

$$z = \delta + 2(w - \delta)$$
$$\Rightarrow \quad z = 2w - \delta \qquad \cdots\cdots \quad (7.1)$$

The central parabola in Figure 7.2 will be a function of the form:

$$y(x) = H_p - a_1 x^2 \qquad \cdots\cdots \quad (7.2)$$

where H_p is the peak height of the parabola and a_1 is a constant coefficient.

It is known that:

$$y\left(\frac{z}{2}\right) = 0$$

$$\Rightarrow \; y\left(w - \frac{\delta}{2}\right) = 0 \quad \textit{from equation} \quad 7.1$$

$$\Rightarrow \; H_p - a_1\left(w - \frac{\delta}{2}\right)^2 = 0$$

Rearranging gives:

$$a_1 = \frac{4H_p}{(2w - \delta)^2} \quad \cdots\cdots\cdots \quad (7.3)$$

Substituting equation 7.3 into 7.2 gives:

$$y(x) = H_p - \frac{4H_p}{(2w - \delta)^2}x^2 \quad \cdots\cdots\cdots \quad (7.4)$$

The projected bead width constraint has now been satisfied. All that remains is to satisfy conservation of mass. If the symmetries in Figure 7.2 are closely examined it can be seen that the shaded area represented by A_d is mathematically equivalent to the following:

$$A_d = \int_{-\frac{\delta}{2}}^{\frac{\delta}{2}} H_p - \frac{4H_p}{(2w - \delta)^2}x^2 \,.\, dx$$

..... and once again by symmetry:

$$A_d = 2\int_{0}^{\frac{\delta}{2}} H_p - \frac{4H_p}{(2w - \delta)^2}x^2 \,.\, dx$$

Now, the cross-sectional area of deposited material will be the same as that for a matching single bead. Thus, A_d can be replaced according to equation 6.17 (page 129) to give:

$$\frac{W}{\rho S} = 2\int_0^{\frac{\delta}{2}} H_p - \frac{4H_p}{(2w-\delta)^2}x^2 . dx \quad \cdots\cdots\cdots (7.5)$$

where W is the deposition rate, ρ is the density of an all-weld-metal deposit and S is the travel speed. Equation 7.5 can be solved to obtain the peak height of a parabola, H_p, explicitly:

$$H_p = \left(\frac{W}{\rho S}\right)\left(\frac{12w^2 - 12\delta w + 3\delta^2}{12\delta w^2 - 12\delta^2 w + 2\delta^3}\right) \quad \cdots\cdots\cdots (7.6)$$

Substituting equation 7.6 into equation 7.4 gives the expression for the steady-state bead profile:

$$y(x) = \left(\frac{W}{\rho S}\right)\left(\frac{12w^2 - 12\delta w + 3\delta^2}{12\delta w^2 - 12\delta^2 w + 2\delta^3}\right)\left(1 - \frac{4x^2}{(2w-\delta)^2}\right) \quad \cdots\cdots\cdots (7.7)$$

The wire feed rate (*i.e.* deposition rate), travel speed and step-over are generally known and recorded on the welding procedure sheet with other welding parameters. The density of an all-weld-metal deposit is a material property. The bead width, w, is obtainable from either direct measurement or knowledge of the welding parameters and equation 3.4 (page 44).

7.3 PEAK-TO-VALLEY RIPPLE

The peak-to-valley ripple is a parameter of great interest to the hardfacing industry. It refers to the variation in the height of an overlay from the peak of a bead to the adjacent trough. It is a measure of the smoothness of an overlay and is believed to affect the wear performance in certain applications (Wittke, 1990).

An estimate for the peak-to-valley ripple, R, is readily obtainable from equation 7.7 by using the following approach:

$$R = \textit{peak height} - \textit{trough height}$$

$$R = y(0) - y\left(\frac{\delta}{2}\right)$$

$$R = \left(\frac{W}{\rho S}\right)\left(\frac{12w^2 - 12\delta w + 3\delta^2}{12\delta w^2 - 12\delta^2 w + 2\delta^3}\right)\left(\frac{\delta^2}{(2w-\delta)^2}\right) \quad \cdots\cdots\cdots (7.8)$$

This expression for peak-to-valley ripple can be used as a check on equation 7.7. For the equation to be correct it must predict the correct ripple at each end-point, *i.e.* at 0% and 100% overlap. Zero overlap corresponds to the case where the step-over, δ, is equal to the bead width, w. In this case there will be a series of single beads side-by-side and the ripple will be equal to the single-bead height. Substituting $\delta = w$ into equation 7.8 reveals that:

$$R = \frac{3}{2}\frac{W}{\rho S w} \quad \textit{at } 0\% \textit{ overlap}$$

This result is in agreement with equation 3.11 (page 55) and the predicted single-bead height.

Although 100% overlap is not possible in reality, the ripple must converge to zero as the step-over approaches zero. If equation 7.8 is examined it can be seen that the ripple is undefined when $\delta = 0$. This is reassuring as it is physically impossible to deposit a single-layer overlay when $\delta = 0$. In order to check the limiting value of the ripple as δ approaches zero, it is convenient to combine the two terms in δ in equation 7.8 as follows:

$$R = \left(\frac{W}{\rho S}\right)\left(\frac{12\delta^2 w^2 - 12\delta^3 w + 3\delta^4}{48\delta w^4 - 96\delta^2 w^3 + 68\delta^3 w^2 - 20\delta^4 w + 2\delta^5}\right)$$

As δ approaches zero the lower order terms in δ survive. The lowest order term in δ is a term in the denominator, δ to the power of unity. This term will dominate as δ approaches zero and consequently the quotient will converge to zero rather than diverge. This limit can be verified by applying l'Hôpital's rule for limiting values of quotients in which the numerator and denominator converge to zero simultaneously.

Equations 7.7 and 7.8 have the correct end-point values and will provide a model for the steady-state bead profile in a multi-pass overlay. Mathematically, bead overlap may assume a value between zero and 100%. In practice, however, overlaps between 40 and 60% are recommended (Gorman, 1997). Overlaps below 40% may result in a high peak-to-valley ripple, whereas overlaps above 60% may reduce penetration to a degree where there is a risk of lack of fusion.

7.4 THE FUSION LINE

Having obtained the profile of the previous bead, the next step is to determine the fusion line. The fusion line can also be modelled by a parabolic function. The two parameters that define the parabola are the width and the depth. The width is defined by the limits of melting (see Figure 7.3). Melting associated with the last bead must commence on the surface of the previous bead, at the trough between the last bead and the previous bead. Melting will cease at the toe of the last bead. It must be noted that melting will not proceed at 90° to the x-axis; it will proceed in a direction that is perpendicular to the straight line between the limits of melting. Consequently, an x'-y' coordinate system

was defined in order to describe the melting parabola. Melting will proceed at 90° to the x' axis in Figure 7.3.

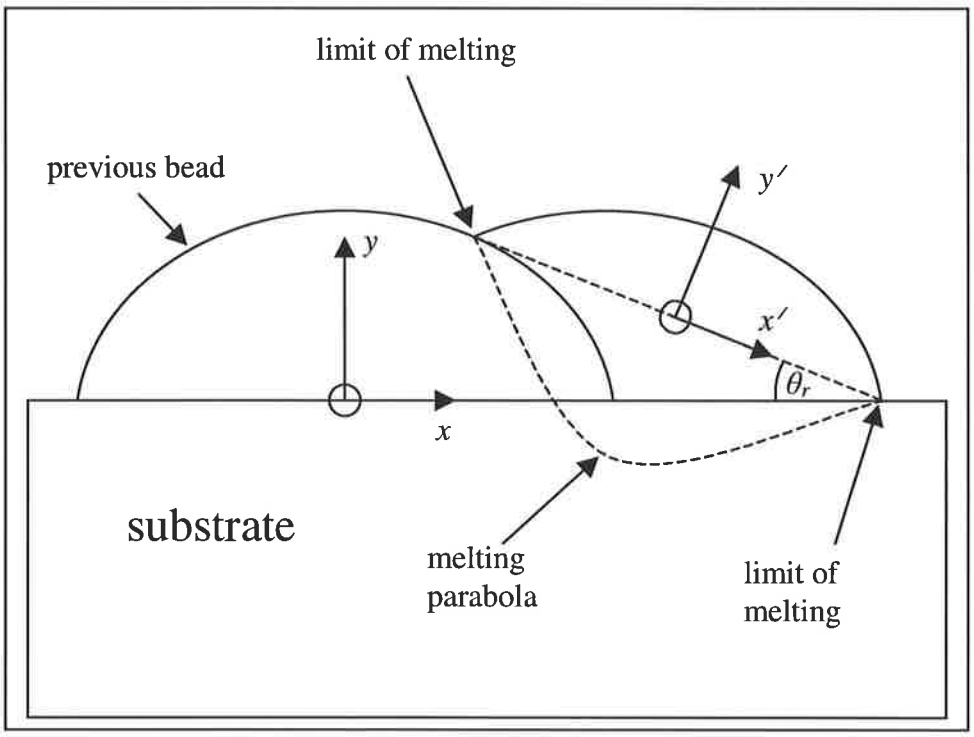

Figure 7.3: - The limits of melting and the coordinate system for the melting parabola. The coordinate system for the melting parabola is denoted x'-y' in the diagram and is rotated by an angle θ_r relative to the x-y coordinate system.

The other constraint on the melting parabola is the requirement that the correct amount of material is melted. This information is obtained from the equivalent single-bead dilution. Thus a parabolic approximation to the fusion line is available. The melting parabola, however, is difficult to solve explicitly, largely due to its axis being rotated relative to the x-y coordinate system. Consequently, a spreadsheet program was developed to solve for the steady-state fusion line numerically.

7.4.1 A Spreadsheet Solution

The spreadsheet program requires the user to enter the following input data:

i. Wire feed rate (*i.e.* deposition rate, W).

ii. Travel Speed, S.

iii. Step-over, δ.

iv. Bead width, w.

v. Single-bead dilution, D_{sb}.

Values for the first three inputs are generally set by the operator and recorded on the welding procedure sheet. Values for the single-bead dilution and width can be predicted using equations 2.2 (page 10) and 3.4 (page 44) respectively. Alternatively, they can be measured directly by depositing a single bead-on-plate.

The bead profile and fusion line are generated in the following steps:

(a) An x-y Cartesian coordinate system is established as defined in Figure 7.2.

(b) The steady-state parabola for the bead profile is generated at discrete points (three times to represent three adjacent beads) using equation 7.7 and data inputs (i) to (iv). Each parabola is offset from its nearest neighbour by one step-over, δ. The all-weld-metal density, ρ, was assumed to be 7500 kg/m^3 for high-chromium white irons. (The all-weld-metal density is a function of the volume fraction of carbides in the all-weld metal deposit. This value was obtained by assuming a total carbide volume fraction of 50% in the all-weld-metal deposit and referring to the density data of Maratray and Usseglio-Nanot (1970)).

(c) The width of the melting parabola, w^* (see Figure 7.4), is calculated using Pythagoras' theorem:

$$w^* = \sqrt{w^2 + \left[y\left(\frac{\delta}{2}\right)\right]^2}$$

The function $y(x)$ is given by equation 7.7.

(d) The area of substrate that is melted in a matching single-bead deposit is calculated using equation 6.18 (page 130).

(e) The melting area correction, as defined in Figure 7.5, is determined by numerical integration.

(f) The melting area correction is added to the area of substrate that is melted in a matching single-bead deposit to give the area of the melting parabola and hence the melting depth.

(g) The melting parabola is generated at discrete points in its own x'-y' coordinate system.

(h) The desired angle of rotation, θ_r (see Figure 7.3), is calculated from the Pythagorean triangle described in step (c).

(i) The melting parabola is rotated, translated and plotted for each of the three bead profiles generated in step (b) to complete an image of the overlay. The rotation is achieved by performing a matrix operation on each of the discrete points generated for the melting parabola. The coordinates of a point (x', y') in the x'-y' coordinate system are converted to a point (x, y) in the x-y coordinate system by the following transformtion (Anton and Rorres, 1987):

$$\begin{bmatrix} x \\ y \end{bmatrix} = \begin{bmatrix} \cos\theta_r & \sin\theta_r \\ -\sin\theta_r & \cos\theta_r \end{bmatrix} \begin{bmatrix} x' \\ y' \end{bmatrix}$$

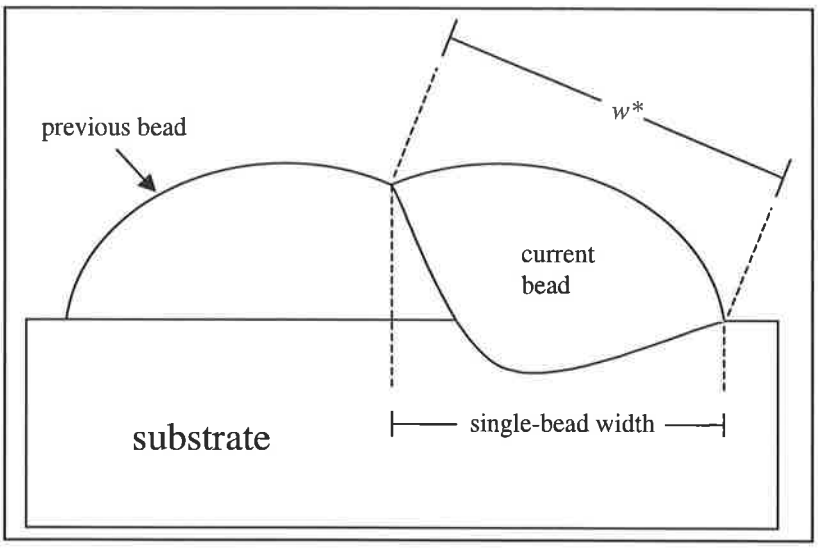

Figure 7.4: - The straight line distance between the limits of melting, w^*, is shown in the diagram. The geometric model assumes that the projected bead width is equal to the single-bead width. The width of the melting parabola, w^*, is then calculated using Pythagoras' theorem.

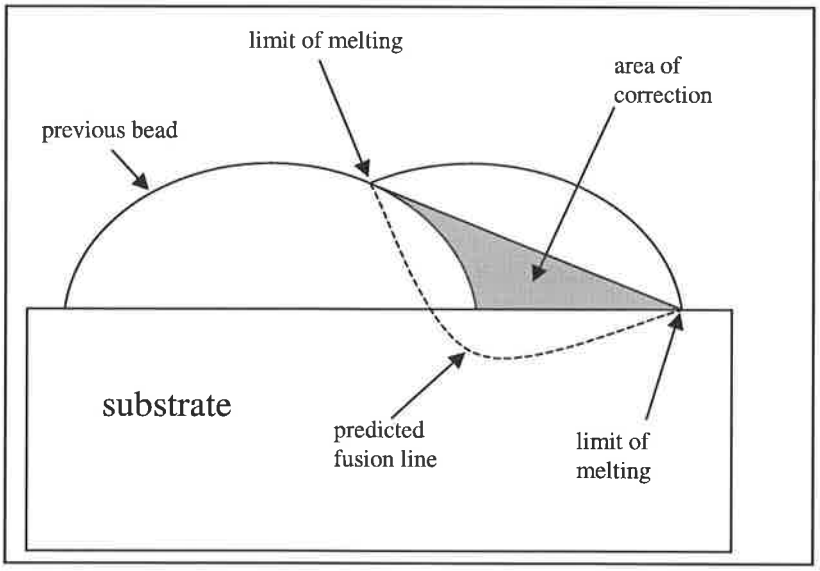

Figure 7.5: - Schematic representation of the melting area correction.

Two examples of the output from the spreadsheet program and hence the geometric model are given in Figures 7.6 and 7.7. The first welding condition corresponds to sample overlay "E" described in section 6.6 and the second to overlay "H". The deposition conditions are summarised in Table 6.2 (page 121) and details of the geometry of each sample are given in Table 6.3 (page 122).

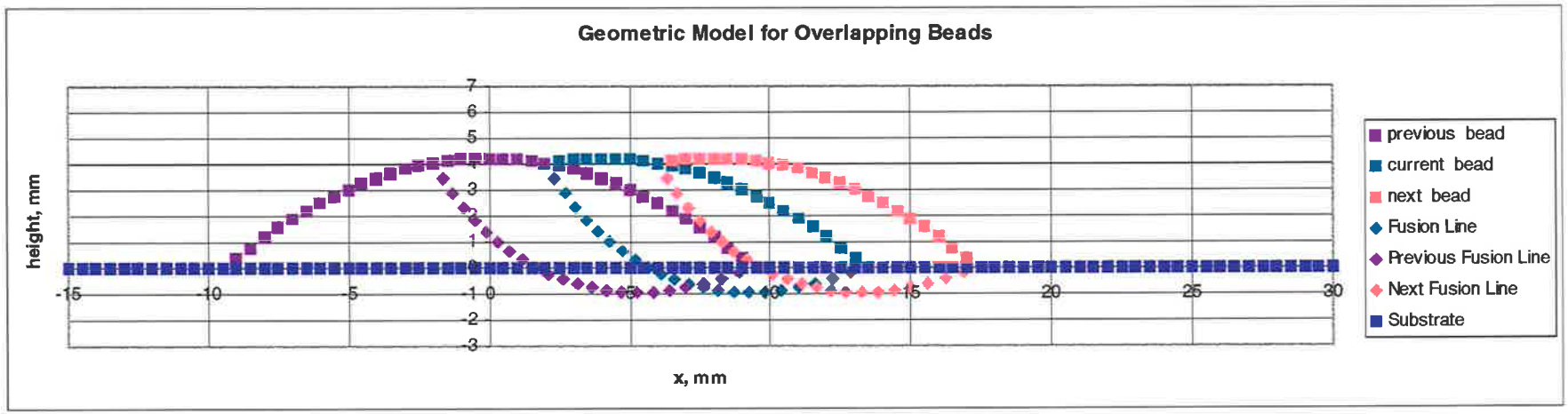

Figure 7.6: - The output of the geometric model for welding condition E (see Table 6.2 – page 121). In agreement with the model, the measured steady-state penetration for this sample was 0.9mm (see Table 6.3 – page 122). The first bead contains the entire steady-state parabola for the bead profile, for the purpose of illustration. The original substrate surface has been included for clarity.

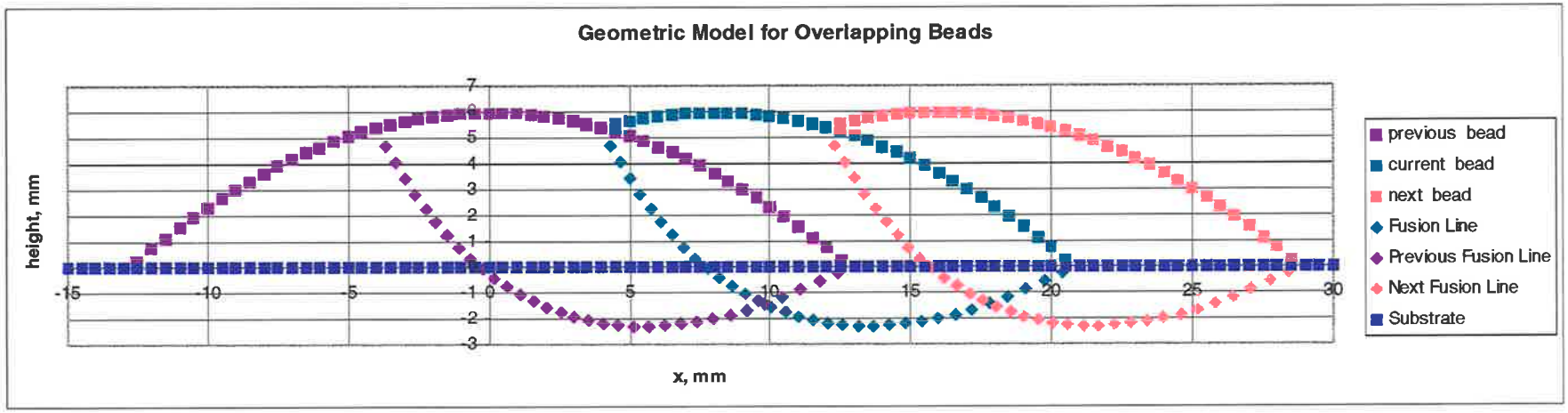

Figure 7.7: - The output of the geometric model for welding condition H (see Table 6.2 – page 121). The measured steady-state penetration for this sample was 1.7mm (see Table 6.3 – page 122) and the output of the model suggests that the average penetration is 2.0mm. This welding condition provides a contrast to that in Figure 7.6. The original substrate surface has been included for clarity.

7.5 COMPARISON WITH EXPERIMENTS

The output data from the geometric model were compared with the results of experiments "A" to "H" (see section 6.6). Once again, the test of accuracy was to determine the ability of the model to predict the average penetration of the overlay under steady-state conditions. In addition, the peak-to-valley ripples were measured for each sample and included in Table 7.1. One of the key assumptions in the development of the model was that the projected bead width in a multi-pass overlay is the same as the single-bead width. Consequently, the projected bead width in each overlay is also compared to the width of the matching single bead.

Sample	Height (mm)	Overlap	IP Temp. (°C)	Penetration (mm)		Ripple (mm)		Width (mm)	
				Predicted	Measured	Predicted	Measured	Single Bead	Projected Width
A	2.0	0.48	25	1.8	2.0	0.3	0.5	11.6	10.0
B	3.0	0.44	25	1.7	1.5	0.5	0.5	10.8	10.5
C	4.3	0.50	25	2.0	1.8	0.5	0.3	15.9	15.5
D	4.1	0.55	400	2.3	2.1	0.4	0.2	17.9	16.5
E	4.3	0.65	25	0.9	0.9	0.2	0.1	11.4	11.5
F	4.3	0.69	400	1.3	1.3	0.1	0.2	12.8	13.0
G	5.2	0.62	25	1.3	1.3	0.3	0.2	13.2	12.5
H	6.1	0.52	25	2.0	1.7	0.6	0.2	16.8	16.0

Table 7.1: - A comparison of the geometric models predictions with experimental results.

It can be seen that there is good agreement between the penetrations predicted by the geometric model and the experimental results. The agreement is acceptable over the

entire range of welding conditions that were considered, and it is similar to that achieved by the k-λ model with an empirical correction. There is also reasonable agreement between the predicted ripples and those measured in experiment for all conditions except "H". Furthermore, for each of the eight overlays, the projected bead width remained virtually unchanged from the width of the matching single-bead deposit.

There appears to be a tendency to overestimate the average penetration for the overlays deposited at low speeds (*i.e.* conditions "C", "D" and "H"). For the overlays deposited at higher travel speeds, (*i.e.* "A", "B", "E", "F" and "G") this trend does not appear to exist. It is most likely that, at slow welding speeds, the discrepancy is caused by the weld pool flowing under the influence of gravity. Under these conditions the weld pool is larger, the cooling times are slower, and the weld pool has more time to flow. Flow occurs both in front of the electrode and behind it. The flow in front of the electrode may result in material from the previous bead flowing on to molten substrate, thus reducing the amount of substrate that is melted and exposing more of the previous bead to the arc. Flow behind the electrode causes the bead profile to deviate from a parabolic shape and form a flatter, wider bead. Consequently, when the next bead is deposited, the arc is forced to melt more of the previous bead and less of the substrate.

The peak-to-valley ripple is a feature that is difficult to predict accurately because the surface of an overlay is not perfectly smooth. The predictions of the model do, however, appear to be reasonable, particularly for those samples deposited at moderate-to-high speeds. There is a tendency, at slow travel speeds, (*i.e.* for "C", "D" and "H") to overestimate the ripple. Once again, this can be explained in terms of weld bead

flattening caused by gravity-induced flow. This flattening effect is particularly prevalent in high overlays such as "H".

It would appear that the major sources of error for this model are related to the geometry of the overlay and not the thermal or physical properties. For both the penetration and peak-to-valley ripple, the most noticeable discrepancies occur when the assumption of a parabolic bead profile is least accurate. If the differences in thermal properties between the overlay material and substrate were the principal causes of error, one might expect, for example, the penetrations to be consistently overestimated. High-chromium white irons have a lower melting point than steels, typically 1220-1250°C, compared with 1450-1500°C. Consequently they are likely to be the first material to melt and they may melt preferentially to steel, thus reducing the penetration of the overlay. However, such a consistent discrepancy is not observed in the experimental data.

The apparent insensitivity of the overlay penetrations to thermal or physical property differences is an interesting point. During the course of the experiments it was observed that, if the same amount of heat were to be delivered to each material, white iron would melt in greater quantities than steel. This observation, however, does not necessarily create a problem for the model. It was noted in section 6.3 that, to define the steady-state dilution, it is necessary to know only the quantity of material that is deposited per pass and the amount of new substrate that is melted per pass. The quantity of the previous bead that is melted will not matter provided that it does not influence the amount of new substrate that is melted.

7.6 GAS-TUNGSTEN ARC WELDING EXPERIMENTS

A series of experiments were planned to further investigate the influence of thermal properties on the location of the fusion line. In these experiments the intention was to maintain a gas-tungsten arc while travelling along the interface between two flat bars, one being a steel and the other a white-iron casting. The flat surface prior to welding would eliminate the effects of overlay geometry, and the partitioning of melting between the two materials could then be identified. A schematic representation of the experiment is given in Figure 7.8.

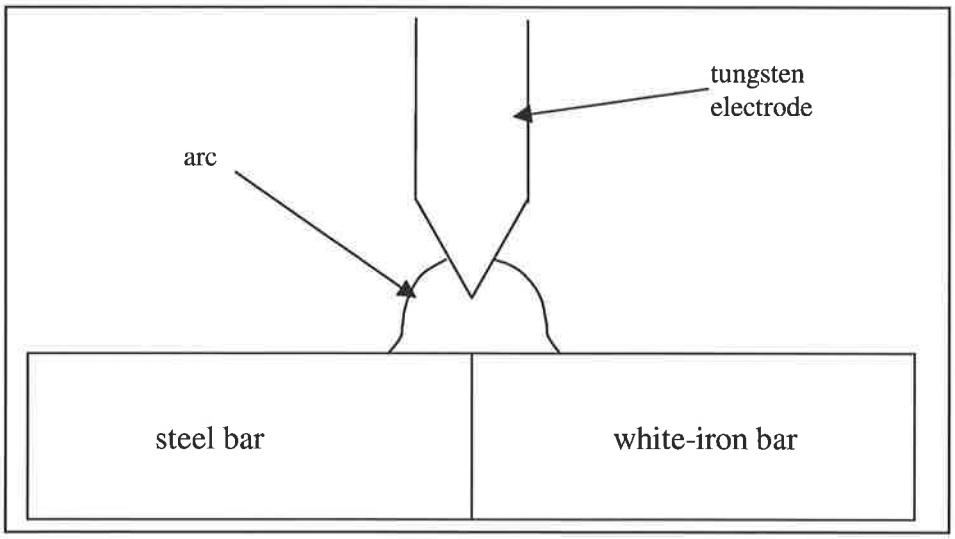

Figure 7.8: - Schematic representation of the GTAW welding experiments.

GTAW welding was selected for two reasons. The problem is simplified by removing the influence of metal transfer. In addition, GTAW welding removes the possibility of the electrode wandering and thus influencing the partitioning of heating between the two materials. (FCAW welding consumables usually acquire some degree of curvature when they are wound on to a reel. When welding commences, this curvature may cause the

length of electrode that is protruding from the contact tip to "wander" from the desired position.)

7.6.1 Description of Experiments

There were four welds in total. In each case the weld configuration was a partial-penetration square-butt weld approximately 300mm in length. All welds were autogenous and the materials to be welded were flat bars 50mm wide, 350mm long and 25mm thick. In all cases both bars were tack welded on to a flat base plate prior to the experiment as shown in Figure 7.9.

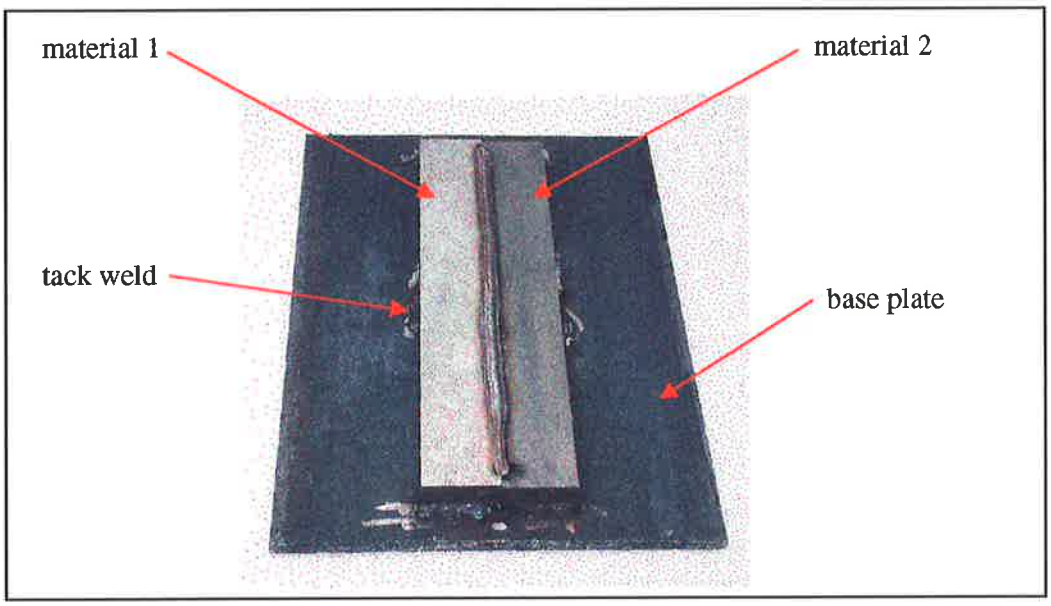

Figure 7.9: - The configuration of a sample in the GTAW welding experiments.

Two holes were drilled in each base plate for work-return leads; one at each end and both on the centre line of the weld, so that the probability of arc blow was reduced. The tack welds, which provided the electrical contact between the work and the base plate, were also distributed symmetrically about the weld centre line. Great care was taken to ensure that the tungsten electrode was aligned with the interface between the materials to

be welded. The electrode was moved down towards the seam, so that it almost touched the bars, and was aligned at both ends before being retracted to the desired arc length.

The experimental plan is summarised in Table 7.2. In one of the experiments a white-iron casting is welded to a steel bar, a steel-to-steel weld is included and a white-iron bar is also welded to another white-iron bar. Finally, a steel bar is welded to a white-iron bar with a 2mm step at the interface. In this case the white-iron bar was closest to the welding electrode. All of the steel bars used in the experiments were cold-finished carbon steels, containing 0.2 wt.% C. The white-iron bars were sand castings containing 19.6% Cr, 3.95% C, 1.5% Mo, 0.9% Mn and 0.9% Si by weight. This composition was chosen as it is representative of that which might be achieved in a low-dilution 4mm high weld overlay.

Experiment No.	Material 1	Material 2	Step (mm)	Arc Length (mm)	Voltage (V)	Current (A)	Speed (mm/min)
I	steel	steel	0	2.5	14.3	350	400
II	white iron	white iron	0	2.5	14.4	350	400
III	steel	white iron	0	2.5	13.6	350	400
IV	steel	white iron	2	1.0 (from near surface)	11.6	350	400

Table 7.2: - A summary of the welding conditions for each of the four GTAW experiments. Voltages and currents were recorded on the CSIRO welding monitor described in section 3.2.

In all cases the direct-current, electrode-negative (DCEN) configuration was selected to prevent melting of the 4mm diameter, ceriated tungsten electrode. The electrode was ground so that it had a conical tip with an included angle of 90°. A large angle was selected to reduce the current density (Hiraoka *et al.*, 1986), and therefore produce a weld bead that was wide, with a penetration profile that was approximately parabolic in shape. A helium-rich shielding gas was selected as this also favours the formation of wide beads (AWS Welding Handbook, 1991). The shielding gas comprised 75 vol.% helium with the balance being argon. A summary of other parameters is included in Table 7.2.

7.6.2 Results

After the experiments were completed, each weld was sectioned, polished, etched and photographed. For the steel-to-steel weld the etchant was 2% Nital, for the steel-to-white-iron samples 2% Nital was used followed by Vilella's reagent, whereas the white-iron-to-white-iron weld was etched with Vilella's reagent only. The photographs are shown in Figures 7.10. For each experiment, the cross-sectional area of material that was melted from each of the bars was measured and included in Tables 7.3. The melted areas were measured by printing the images, reconstructing the original surfaces of the bars, cutting the melted sections from the images and then weighing them. It can be seen that there are two results listed for experiment I. For the steel-to-steel sample the weld pool solidified, in some instances, before it was able to flow and weld the bars together. This sample was sectioned twice, once where the weld pool was intact and once where it was not, and results are shown for both cases.

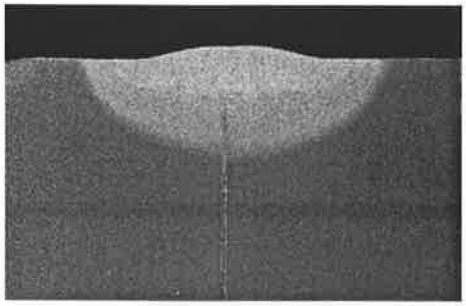

steel steel

a) Experiment I

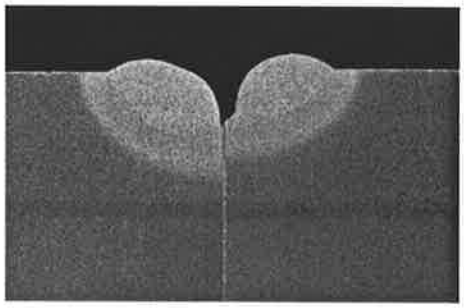

steel steel

b) Experiment I

white iron white iron

c) Experiment II

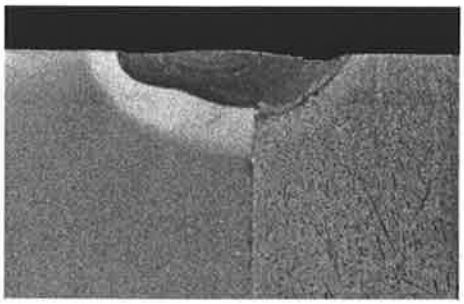

steel white iron

d) Experiment III

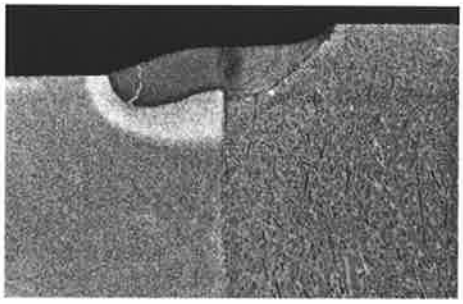

steel white iron

e) Experiment IV

Figures 7.10: - The results of the GTAW welding experiments. Note the step change in the location of the fusion line at the interface between the bars in (d) and (e).

Similar Materials

Experiment	Material	Area Melted (left-hand side), mm^2	Area Melted (right-hand side), mm^2	Total Area Melted, mm^2
I	steel (unbroken weld)	6.6	7.9	14.5
I	steel (broken weld)	10.9	7.7	18.6
II	white iron	13.0	14.3	27.3

Dissimilar Materials

Experiment	Steel Melted, mm^2	White-Iron Melted, mm^2	Total Area Melted, mm^2
III	11.2	7.7	18.9
IV	5.5	10.6	16.1

Tables 7.3: - A summary of the results of cross-sectional area measurements for the GTAW welding experiments.

7.6.3 Discussion

Figures 7.10 and, in particular, the welds between similar materials show that the alignment of the tungsten electrode was accurate. These welds were distributed evenly across the interface between the bars. While the areas measured for the broken steel-to-steel weld indicate that, at that particular location, melting occurred preferentially on one side of the interface, a close examination of the image reveals that the edges of the weld pool were approximately equi-distant from the interface. Thus, the apparent bias may have been related to the location of the weld pool at the moment the arc passed by.

It is evident from experiments I and II that, for a given set of welding parameters, more material will melt when the substrate is a high-chromium white iron than when it is mild steel. This result is not unexpected since high-chromium white irons have a lower melting point than steels. It is also evident from experiment I that the location of the weld pool affects the amount of material that is melted, with 25 – 30% more material being melted when the weld pool was broken than when it was continuous. This result indicates that the weld pool does, to some extent, cushion the surrounding material from further melting, as was suggested in an early work by Farmer (1966b).

Experiment III provided an unexpected result in that more steel was melted than white iron. One might have expected a greater quantity of white-iron to melt given its lower melting point. It would appear, therefore, that heat from the arc was delivered preferentially to the steel. Such a bias may have been introduced by asymmetric convection within the weld pool. Lancaster (1986) illustrated how, when welding dissimilar materials, asymmetric surface tension gradients may result in the preferential melting of one material (see Figure 7.11). The superheated molten metal immediately

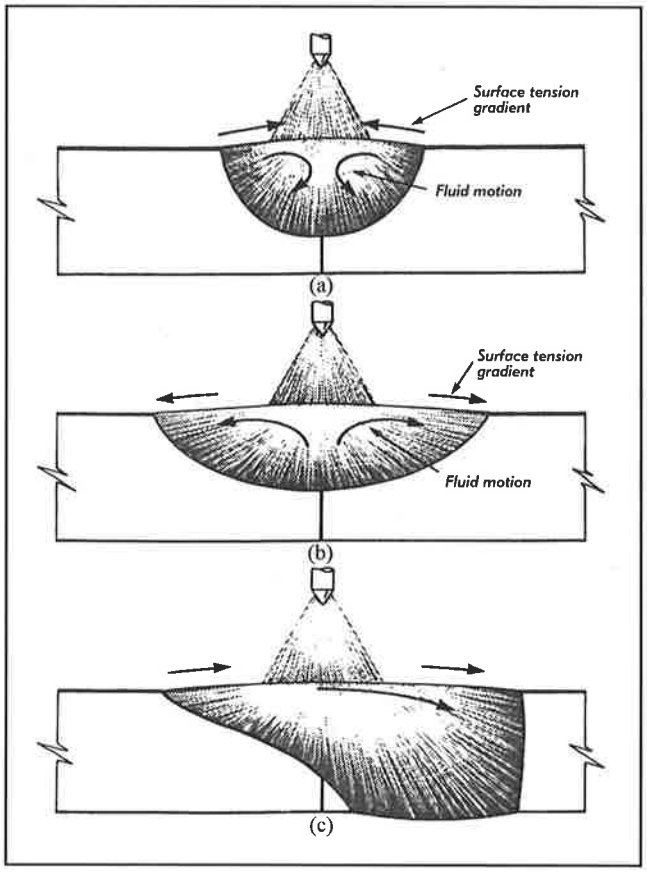

Figure 7.11: - The effects of surface-active elements on weld pool convection and fusion zone geometry in GTAW weldments (after Lancaster, 1986): (a) surface-active elements present; (b) surface-active elements absent; (c) dissimilar materials.

under the arc will be transported toward the material with the higher surface tension, resulting in the preferential melting of that material. The results of experiment I also support this argument. The fact that the weld pool was frequently broken in the steel-to-steel weld suggests that the surface tension of the liquid steel was high enough to prevent the pool from recombining. Furthermore, the weld pool remained intact for all welds with white iron, which suggests that the liquid white iron had a lower surface tension than the liquid steel. It should be noted, however, that the effects of asymmetric convection were not observed in overlays A to H, which were deposited by open-arc

FCAW. This suggests that the molten globules being transferred to the weld pool play an important role in disturbing such convection patterns. It is possible that, in this way, the globules promote a relatively uniform distribution of heat throughout the pool.

The role played by the molten globules in determining the distribution of heat may explain why the geometric model can accurately predict average overlay penetrations. The geometric model superimposes a melting parabola, defined by the single-bead dilution, on to the profile of the previous bead to predict the fusion line. The implicit assumptions are that the heat is distributed uniformly, and that the material properties are the same for both materials. The fact that the material properties for the white iron are different to those of the steel, however, may not significantly affect the amount of steel that is melted. If the heat is distributed uniformly and, to a first-order approximation, the amount of steel that is melted remains unchanged, then the predicted overlay penetration will be accurate.

If heat were to be distributed uniformly throughout the weld pool, one might expect that the cross-sectional area of material that is melted in an overlapping bead, A_m, will be given by the following equation:

$$A_m = \gamma A_{st} + (1-\gamma)A_{wi} \quad \text{..... (7.9)}$$

where A_{st} and A_{wi} are the areas of substrate that would be melted in matching single beads deposited on steel and white-iron substrates respectively, and γ is an energy partitioning coefficient. A_m excludes the area that is contributed by deposited material. Equation 7.9 is an energy balance, and it suggests that any energy that is not used in the melting of steel must be available for the melting of white iron and vice versa. This

definition for γ is consistent with the definition given in section 6.8. The validity of equation 7.9 is tested in Tables 7.4 and 7.5.

Steel Melted in Experiment I	14.5 mm^2
Steel Melted in Experiment III	11.2 mm^2
Estimate for γ	0.77
Total White Iron Melted in Experiment II	27.3 mm^2
Predicted White Iron Melted in Experiment III	***6.2 mm^2***
Actual White Iron Melted in Experiment III	***7.7 mm^2***

Table 7.4: - The procedure for predicting the area of white iron that was melted in Experiment III using equation 7.9.

White Iron Melted in Experiment II	27.3 mm^2
White Iron Melted in Experiment III	7.7 mm^2
Estimate for $(1 - \gamma)$	0.28
Total Steel Melted in Experiment I	14.5 mm^2
Predicted Steel Melted in Experiment III	***10.4 mm^2***
Actual Steel Melted in Experiment III	***11.2 mm^2***

Table 7.5: - The procedure for predicting the area of steel that was melted in Experiment III using equation 7.9.

The results in Tables 7.4 and 7.5 indicate that, in this instance, the predictions made by equation 7.9 appear to be reasonable. The largest error was observed in Table 7.4 where the quantity of white iron that was melted was underestimated by approximately 20%. More work, however, will be required to confirm the results presented in this section and, in particular, the validity of equation 7.9.

Finally, another cause of preferential melting was demonstrated in experiment IV. If the arc gap between the electrode and one of the materials is reduced, then the heating will be biased toward that material. The results of experiment IV were not used to test the validity of equation 7.9 as a different arc length (and hence heat input) was used to that in the other experiments.

7.7 LIMITATIONS OF THE MODEL

The geometric model accurately predicts the steady-state penetration of a multi-pass overlay under many different welding conditions. There are, however, some situations in which the accuracy of the model may be compromised. This section describes some of the limitations of the geometric model.

7.7.1 Sensitivity to Input Data

The predictions of the model are sensitive to the input data. If, for example, the correct single-bead dilution is entered but the bead width is overestimated by 2mm, say, an error in penetration of up to 0.5mm may result in some circumstances. Errors in predictions of bead width or single-bead dilution change the depth-to-width ratio of the melting parabola and hence the predicted penetration. In practice the best predictions for multi-pass overlays are achieved by depositing a single bead with the chosen welding parameters, and measuring the single-bead width and dilution. If the overlay welding conditions deviate significantly from the conditions that were used for the single-bead deposit, accurate predictions may still be achieved by normalising the single-bead data with the procedure outlined in section 6.6.

7.7.2 Transient Conditions

The geometric model predicts the overlay dilution and geometry under steady-state conditions. It cannot predict the dilution for the transient period at the commencement of deposition, nor can it predict the number of beads that will be required before a steady-state condition is reached.

7.7.3 Inter-Pass Temperature

The predictions of the model are only accurate if the inter-pass temperature is maintained at the same value that was assumed (or used) to obtain values for the single-bead dilution and width. When depositing a multi-pass overlay the inter-pass temperature can deviate significantly from its initial value due to cumulative heating of the substrate. For the model to be accurate, and to keep the penetration to a minimum, appropriate cooling measures or time delays need to be introduced.

Care also needs to be taken when depositing overlays bi-directionally. If deposition proceeds without an appropriate delay at each end, the previous bead will still be very hot. Under these circumstances an alternating high-low penetration profile is observed, such as the one shown in Figure 7.12. This sample was deposited specifically to demonstrate this phenomenon. Such a penetration profile may result in the preferential wear of every second bead in the overlay, and reduce the wear life of the component.

The substrate in Figure 7.12 was a 0.2 wt.% C steel bar 350mm long, 100mm wide by 10mm thick. The welding consumable was equivalent to consumable B (see section 3.2). Four pairs of beads were deposited with each bead being approximately 300mm in length. The first bead was deposited and the arc was maintained while the welding head

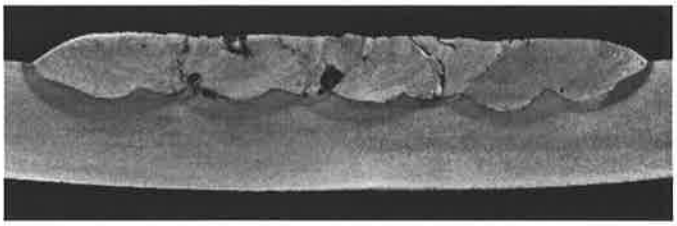

Figure 7.12: - An example of an alternating low-high penetration profile. Such a profile can be obtained at the end of an overlay that is deposited bi-directionally if there are no time delays to allow for cooling, or if the cooling is inadequate. Deposition proceeded from right to left.

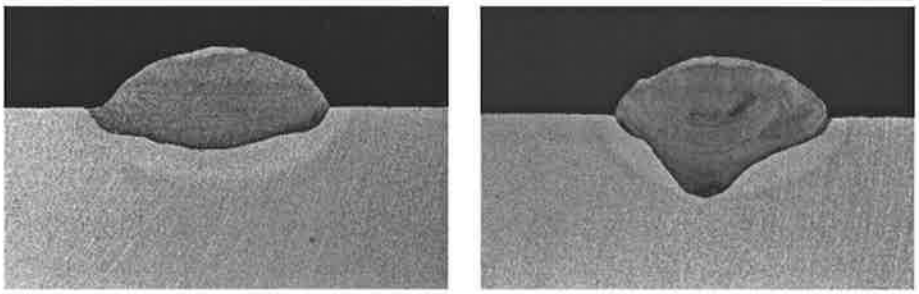

Figures 7.13: - An example of a sudden variation in the penetration profile. These two sections were taken from the same single-bead deposit and were separated by only 10mm of travel.

stepped over and immediately deposited the second bead. The plate was then left to cool for several minutes before the procedure was repeated. The intention was to reproduce the conditions that might arise, for example, at the end of a large pipe that is being surfaced bi-directionally. For all of the beads, the nominal welding parameters were 28V; 400A; 20mm work distance; 800mm/min travel speed; and 6mm step-over. The section shown in Figure 7.12 was taken approximately 40mm from the position where the welding head turned around for the second pass.

7.7.4 Bead Profile

Under certain welding conditions the profile of the fusion line may deviate from a parabolic shape. Kim and Na (1995), for example, showed that a finger-like penetration profile is favoured when a low work distance is used (see section 2.3). The predictions of the model may be less accurate if the penetration profiles of individual beads differ significantly from a parabolic shape.

In other instances a welding consumable may appear to be susceptible to random variations in penetration. Some examples were observed in the current work and one is shown in Figures 7.13. These figures show two sections through the same single-bead deposit that were separated by only 10mm of travel. Such random and sudden changes in penetration may be related to the molten globules detaching from the consumable electrode at irregular intervals. For example, a temporary reduction in the detachment frequency would initially result in a smaller weld pool. More of the underlying substrate would then be exposed to the heat of the arc and a temporary increase in the penetration would result. If the penetration profile is inconsistent, it is important to obtain more than

one measurement of the single-bead dilution and enter an average value into the geometric model.

7.8 CONCLUSIONS

A geometric model has been developed that accurately predicts the steady-state dilution of high-chromium white iron multi-pass overlays. The model is based on the assumption that both the steady-state bead profile and the fusion line can be represented by parabolic functions. The predictions of the model are most accurate when the welding conditions include a high travel speed as, under these circumstances, the bead profile closely resembles a parabola. The accuracy is acceptable, however, at lower travel speeds. The most significant limitation associated with the model is its sensitivity to the input data. Nevertheless, the model has been shown to work for two high-chromium, high-carbon type consumables, and it is anticipated that it will generally apply to similar consumables.

8

Principles for Weld Deposition of High-Chromium White Iron Surface Layers

8.1 INTRODUCTION

In chapter 3, the factors affecting the dilution and geometry of single-bead deposits were addressed. In chapters 4 and 5 the focus shifted to the relationship between the microstructure of a weld deposit and its wear performance. Chapter 5, however, revealed that the mechanisms controlling dilution in multi-pass overlays are different to those that control the dilution of single-bead deposits. Consequently, chapters 6 and 7 were concerned with the development of models for predicting dilution in multi-pass overlays. It is now possible, with the aid of these models, to identify the conditions that lead to minimum dilution. This chapter reviews the results presented thus far, and describes a set of principles that will assist in achieving the desired outcome when depositing a high-chromium white iron overlay.

8.2 ACHIEVING THE DESIRED MICROSTRUCTURE

It was seen in chapter 4 that hypereutectic microstructures often provide the best resistance to abrasion in the absence of impact. Thus, in many applications, it will be of prime importance to ensure that a hypereutectic microstructure is achieved.

A study by de Sairre Balsamo *et al.* (1995) found that the meta-stable phase diagram proposed by Jackson (1970) serves as a useful tool for predicting the microstructure of

Fe-Cr-C weld deposits. A predicted microstructure can either be read from the diagram directly or inferred from a comparison of the weld deposit composition with the eutectic carbon concentration, $[C]_{eut}$, given by:

$$[C]_{eut} = 4.25 - 0.162\left([Cr]/[C]\right) + 0.0023\left([Cr]/[C]\right)^2 \quad \cdots\cdots\cdots (8.1)$$

where $[Cr] : [C]$ is the ratio of the chromium concentration to the carbon concentration in the deposit. Equation 8.1 is a fit to Jackson's phase diagram. If the carbon concentration in the weld deposit is greater than that estimated for the eutectic composition it is likely that that the resulting microstructure will be hypereutectic. The concentrations of chromium, $[Cr]$, and carbon, $[C]$, in the weld deposit are obtained from the following expressions:

$$[Cr] = (1 - D) \times [Cr]_{awm}$$
$$[C] = (1 - D) \times [C]_{awm} \quad \cdots\cdots\cdots (8.2)$$

where $[Cr]_{awm}$ and $[C]_{awm}$ are the concentrations of chromium and carbon in an all-weld-metal deposit respectively, and D is the deposit dilution. Typical all-weld-metal compositions are usually supplied by the manufacturer of the welding consumable. Thus, an estimate for the dilution will allow the deposit microstructure to be predicted.

It can be seen that there are at least two ways in which it is possible to influence the microstructure of a weld deposit. The selection of the welding consumable defines an envelope or range of achievable deposit compositions. For example, it is not possible to achieve a composition higher in carbon and chromium than an all-weld-metal deposit. There will also be an upper limit on dilution, which will determine the lower bound for

the carbon and chromium concentrations. The exact deposit composition within that range will then be determined by the selected welding parameters and the dilution that results.

8.3 DILUTION CONTROL FOR SINGLE-BEAD DEPOSITS

8.3.1 Predicting Single-Bead Dilution

For a given combination of substrate and welding consumable, the dilution of a single-bead deposit, D_{sb}, is described by the Bednarz-Deam model (see section 2.2.3):

$$\frac{D_{sb}}{1 - D_{sb}} = \alpha \frac{VI}{W}(1 + \beta VIS) \quad \cdots\cdots\cdots \quad (2.2) \quad \text{(page 10)}$$

where V is the contact tip-to-work voltage, I is the welding current, W is the deposition rate, S is the travel speed and α and β are fitted constants relating to the particular combination of substrate and welding consumable. Thus, for a given welding consumable and substrate material, it is necessary to deposit only two single beads and measure dilutions in order to obtain values for α and β. Equation 2.2 will then predict the single-bead dilution for other welding conditions.

8.3.2 The Effects of Welding Parameters on Single-Bead Dilution

The results in chapter 3, and the previous studies addressed in chapter 2, suggest the following:

- An increase in voltage, while all other parameters remain unchanged, generally increases the single-bead dilution. An increase in the voltage will result in more heat being delivered to the base material. Consequently, a greater quantity of the base

material will melt. The deposition rate generally does not increase with voltage if the current and work distance remain unchanged, and the net result is an increase in dilution.

- The influence of welding current on single-bead dilution will not be immediately apparent. The welding current influences both the deposition rate (see equation 2.4 – page 12) and the quantity of substrate that is melted, and its effect on dilution will vary with the particular combination of substrate and welding consumable.
- An increase in work distance will result in a lower single-bead dilution. This effect arises due to the associated increase in deposition rate (see equation 2.4 – page 12) and may also be related to the associated reduction in arc voltage.
- An increase in travel speed, while all other parameters remain constant, will result in increased single-bead dilution. The heat input to the substrate and the cross-sectional area of material that is deposited are both inversely proportional to the travel speed. However, the melting efficiency is known to increase with travel speed (Swift-Hook and Gick, 1973). This increase in melting efficiency results in an increased single-bead dilution.
- An increase in preheat temperature will result in an increase in dilution. If all other parameters remain unchanged, an increase in preheat temperature will result in increased melting of substrate material.
- One parameter that has not been addressed thus far is arc polarity. If the wire feed rate and work distance remain unchanged, it is anticipated that the polarity that draws the lowest current will generally provide a lower single-bead dilution. A reduction in current will generally result in less substrate material being melted.

8.3.3 Achieving Minimum Dilution for Single-Bead Deposits

The following guidelines will assist in achieving minimum (or near-minimum) dilution for a single-bead deposit:

- **Use a low voltage.** In practice this will be the lowest voltage that provides arc stability.
- **Use a welding current at the high end of the manufacturer's recommended range.** The effects of welding current on dilution will not be immediately evident. In many instances an increase in current will result in reduced dilution and, under those circumstances, these guidelines should produce the minimum dilution. If, however, the dilution increases with increasing current, it is anticipated that the benefits associated with the higher deposition rate could outweigh the penalty of an increase in dilution.
- **Use an increased work distance.** In practice there is an upper limit for work distance associated with "wire wander". The tubular consumable is not perfectly straight when it emerges from the contact tip and any eccentricities may result in a wandering bead.
- **Use a low travel speed.** The bead profile, however, may present a limitation on the travel speed. Many low dilution beads have a convex bead profile such as the one shown in Figure 3.4(b) (page 47). If bead rollover is unacceptable, or needs to be limited, it may be necessary to increase either the travel speed or the voltage in order to improve the bead profile. Unfortunately, any improvements in bead profile will be achieved at the expense of a higher dilution.
- **Keep preheating to a minimum.**

- **Observe the manufacturer's recommendations regarding the choice of polarity.** Manufacturers often recommend that a specific polarity is used because it provides the smoothest or most desirable mode of metal transfer. If, however, no recommendations are given it is anticipated that, for a given wire feed rate and work distance, the polarity that draws the lowest current will generally provide the lower single-bead dilution.

8.4 DILUTION CONTROL FOR MULTI-PASS OVERLAYS

8.4.1 Predicting the Dilution of Multi-Pass Overlays

Two approaches have been used in the current work. The first expresses the steady-state dilution of a multi-pass overlay, D_{ov}, explicitly in terms of the single-bead dilution, D_{sb}, and γ:

$$D_{ov} = \frac{\gamma D_{sb}}{\gamma D_{sb} + 1 - D_{sb}} \quad \text{.....} \quad (6.21) \quad \text{(page 130)}$$

$$\text{where } \gamma = 1 - \phi - 0.254\,\phi\,(1-\phi)\,(H_{ss} - 3.23) \quad \text{.....} \quad (6.22) \quad \text{(page 131)}$$

and where ϕ is the bead overlap and H_{ss} is the steady-state overlay height in millimetres. The single-bead dilution in equation 6.21 must be obtained for the same welding parameters that are used in the multi-pass overlay.

The second approach is based on geometry and requires numerical methods to evaluate dilution. The details of this approach were described in chapter 7.

8.4.2 The Significance of Overlay Height

The steady-state dilution of a multi-pass overlay, D_{ov}, may be determined by measuring the steady-state height, H_{ss}, and steady-state penetration of the overlay, P_{ss}:

$$D_{ov} = \frac{P_{ss}}{P_{ss} + H_{ss}} \quad \text{.....} \quad (8.3)$$

Equation 8.3 may be used to compare the measured dilution with the dilution that is predicted by equation 6.21 or the geometric model described in chapter 7.

As the height of the overlay increases it is usually necessary to increase the bead overlap in order to achieve sufficient build-up of material. This increase in overlap results in a shift in arc impingement away from the substrate and toward the previous bead, and a lower penetration generally results. The combination of an increase in height and a reduction in penetration results in a lower dilution. To illustrate the dependence of dilution on overlay height, estimates for the minimum and maximum achievable dilutions were obtained by running the k-λ spreadsheet program, and the results are displayed in Figure 8.1. It can be seen that, by specifying a high overlay, the likelihood of achieving a low-dilution deposit increases. Conversely, if a thin overlay is specified it is most unlikely that a low-dilution deposit will be achieved. Thus, it is possible to promote the formation of a specific microstructure by carefully specifying the overlay height.

8.4.3 Achieving the Specified Overlay Height

For a given set of welding parameters, the desired steady-state overlay height, H_{ss}, will be achieved by ensuring that the correct step-over, δ, is selected. The correct step-over is given by equation 5.5, which is repeated here for convenience:

$$\delta = \frac{W}{\rho H_{ss} S} \quad \text{.....} \quad (5.5) \quad \text{(page 98)}$$

where W is the deposition rate, ρ is the density of an all-weld-metal deposit and S is the travel speed.

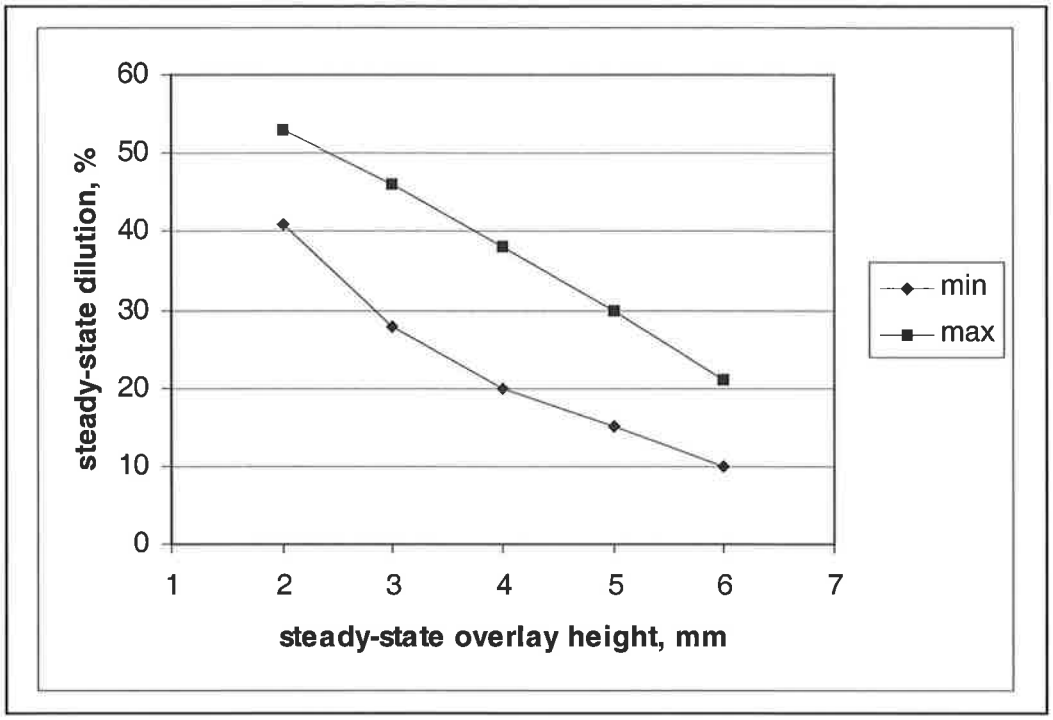

Figure 8.1: - Estimates for the upper and lower limits on dilution in a multi-pass overlay. The estimates were obtained for consumable B (see section 3.2). The upper limits were obtained assuming the inter-pass temperatures were 20°C.

8.4.4 The Effects of Welding Parameters on the Dilution of Multi-Pass Overlays

The preceding discussion demonstrated that, for a particular height of overlay, there is a range of achievable dilutions. The location of the overlay dilution within that range is then determined by the selection of welding parameters. In order to demonstrate the effects that various welding parameters have on overlay dilution, a matrix of different welding conditions was tested in the k-λ spreadsheet program. The voltage, current, work distance and travel speed were each varied systematically from base conditions of

30V, 325A, 30mm and 600mm/min. The base voltage and current were approximately in the middle of the ranges recommended for the consumables studied in the current work. The specified overlay height was 4mm. The program automatically calculates the step-over that will achieve this height. The data for consumable B were used (see section 3.2), and the results are summarised in Table 8.1.

Variable Parameter	Value of Parameter	Single-Bead Dilution, %	Required Overlap, %	Overlay Dilution, %
voltage	*27 V*	*49*	*53*	*26*
	30 V	*54*	*59*	*26*
	33 V	*59*	*65*	*27*
current	**250 A**	**55**	**66**	**22**
	325 A	**54**	**59**	**26**
	400 A	**54**	**33**	**30**
work distance	*20 mm*	*59*	*66*	*26*
	30 mm	*54*	*59*	*26*
	40 mm	*50*	*52*	*27*
travel speed	**300 mm/min**	**50**	**39**	**34**
	600 mm/min	**54**	**59**	**26**
	900 mm/min	**58**	**69**	**23**

Table 8.1: - Estimated single-bead dilutions, overlaps and steady-state overlay dilutions for consumable B under various welding conditions. The base welding conditions were 30V, 325A, 30mm and 600mm/min. The nominal steady-state overlay height was 4mm.

The following observations can be made after examining Table 8.1:

- The steady-state dilution of a multi-pass overlay is relatively insensitive to welding voltage. An increase in voltage does result in a significant increase in single-bead dilution but may also lead to a reduction in the deposition rate at a given current and work distance (Kiyohara *et al.*, 1980). Thus, a greater degree of bead overlap may be required to achieve the specified overlay height. The effect of an increase in overlap is to shift the emphasis of melting from the substrate material to the previous bead. Such a shift in the melting emphasis would offset the effect of a higher single-bead dilution.
- An increase in welding current results in a higher overlay dilution. An increase in the welding current is usually achieved by increasing the wire feed rate (and hence deposition rate). Consequently, the overlap will need to be reduced in order to maintain the specified overlay height. This reduction in overlap shifts the emphasis of melting away from the previous bead toward the substrate material. An increase in current also results in more material being melted and this also contributes to the increase in dilution.
- The steady-state dilution of a multi-pass overlay is relatively insensitive to work distance. An increase in work distance leads to a reduction in single-bead dilution but also to an increase in deposition rate. The required decrease in overlap offsets the reduction in single-bead dilution.
- An increase in travel speed causes a significant reduction in overlay dilution. The size of the bead reduces as the travel speed is increased so that increases in overlap are required in order to maintain the required overlay height. The required increases

in overlap are large enough to outweigh the effect of an increase in single-bead dilution.

The influence of a particular parameter on the steady-state dilution of a multi-pass overlay can generally be explained by combining the effects that the parameter has on both the single-bead dilution and the overlap. The welding current and travel speed appear to be the variables that have the strongest influence on the steady-state dilution of an overlay. The effect of welding current is not unexpected given that higher deposition rates will require less overlap and that higher welding currents generally produce higher penetrations. However, the potential to significantly reduce overlay dilution by increasing the travel speed is unexpected given that increases in the travel speed produce higher single-bead dilutions. This observation does emphasise the effectiveness of bead overlap as a method of reducing overlay penetration and dilution.

The geometric spreadsheet program was run for two different welding conditions in order to illustrate how high travel speeds and the associated high overlaps can shift the melting emphasis from the substrate to the previous bead. The output of the program for these two conditions is shown in Figures 8.2. The welding conditions correspond to those used for overlays C and E (see section 6.6). Both of these overlays were 4mm high and were deposited with a high current and deposition rate, yet their dilutions were significantly different due to the selection of different travel speeds.

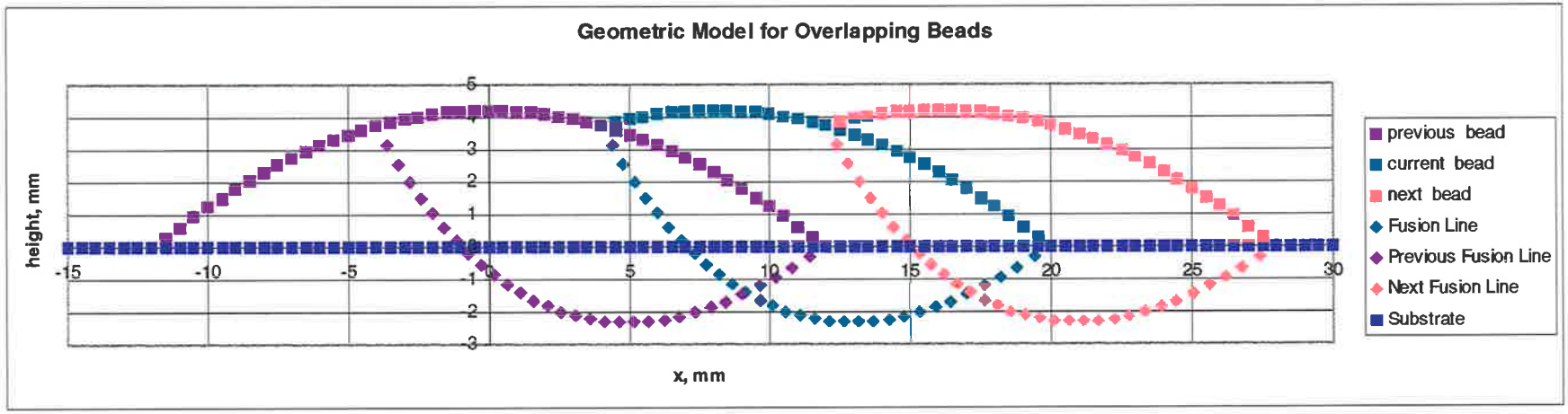

Figure 8.2(a): - The output of the geometric spreadsheet program for welding condition C (see section 6.6), which produced a 4mm high overlay. The travel speed was 400mm/min.

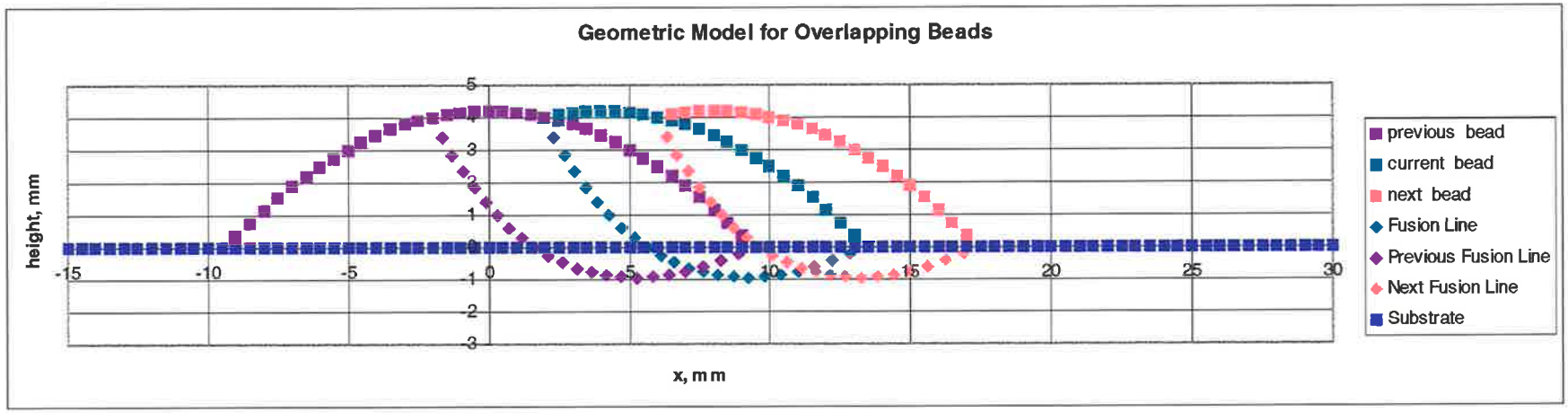

Figure 8.2(b): - The output of the geometric spreadsheet program for welding condition E (see section 6.6), which produced a 4mm high overlay. The travel speed was 800mm/min. Comparison with condition C (shown in Figure 8.2(a)), reveals that a significant reduction in penetration and hence dilution may be achieved by operating with a high-travel-speed. The deposition rates were the same for both conditions.

8.4.5 Achieving Minimum Dilution in Multi-Pass Overlays

The following recommendations and comments will assist in achieving minimum dilution in multi-pass overlays:

- ***Use a low voltage.*** Lower voltages generally result in slightly lower overlay dilutions. It is recommended that the operator select the lowest voltage that provides a consistent and stable arc.
- ***There is a trade-off between deposition rate and overlay dilution with welding current.*** If a low dilution needs to be achieved, regardless of the deposition rate, it is recommended that a low current be selected. In production situations, however, ***where deposition rate is important, an appropriate compromise will need to be reached.***
- ***Use a high travel speed.*** Higher travel speeds significantly reduce the steady-state dilution of an overlay. The upper limit on travel speed will generally be related to the ability of the welding consumable to provide a consistent bead.
- ***Use a low-to-moderate work distance.*** The dilution of a multi-pass overlay appears to be relatively insensitive to work distance. The use of a high work distance increases the probability of the electrode extension, and hence the resulting bead, wandering. Such an effect may result in parts of the substrate remaining uncovered. Uncovered regions often need to be repaired by manual welding which adds to the cost of production. There is also the risk that uncovered regions will remain unnoticed, and that components will be put into service without a complete overlay. Consequently, a low-to-moderate work distance is recommended.

- ***Keep inter-pass temperatures as low as possible.*** Any increases in inter-pass temperature associated with cumulative heating of the work piece result in increased dilution.
- ***Specify a Bead Overlap Between 40% and 60%.*** Bead overlaps between 40 and 60% are generally recommended (Gorman, 1997). Overlaps greater than 60% are likely to result in a low average penetration and, if the penetration is inconsistent, lack of fusion may occur. Such a defect could result in accelerated metal loss when the component is put into service. Conversely, overlaps below 40% may result in a large peak-to-valley ripple, which is thought to be detrimental to wear performance (Wittke, 1990).

8.5 PREDICTING THE DILUTION IN A SECOND LAYER

The steady-state dilution of a second layer with respect to the first layer, $D_{2/1}$, can be estimated using equations 6.21 (page 130) and 6.22 (page 131). The single-bead dilution, however, is replaced by the dilution of a single bead deposited on a white-iron substrate, $D_{sb/wi}$, so that:

$$D_{2/1} = \frac{\gamma D_{sb/wi}}{\gamma D_{sb/wi} + 1 - D_{sb/wi}} \quad \ldots\ldots\ldots \quad (8.4)$$

where $\gamma \approx 1 - \phi - 0.254\,\phi\,(1-\phi)\,(H_{ss} - 3.23)$ ..... (6.22) (page 131)

and where ϕ is the bead overlap and H_{ss} is the steady-state overlay height in millimetres. Alternatively, $D_{2/1}$ can be estimated by substituting $D_{sb/wi}$ into the geometric spreadsheet program, together with the correct bead width, $w_{sb/wi}$. At present, however, there is no simple procedure for estimating $D_{sb/wi}$. One approach would be to deposit a single-layer white-iron overlay until a steady state is reached. If two single beads were then

deposited on top of this layer and their dilutions were measured, values for α and β in equation 2.2 (page 10) could be obtained. These values would correspond to α and β for a substrate having the same composition as the first layer. In order to estimate the composition of the first layer it is necessary to obtain the values of α and β when the substrate is steel. Thus, the values of α and β at two different substrate compositions would be known for the particular welding consumable. Values at any other composition could then be estimated by interpolation or extrapolation. A similar approach can also be employed for the bead width, using equation 3.4 (page 44). The steady-state dilution of the second layer with respect to the substrate, D_2, is then given by:

$$D_2 = D_{2/1} \times D_1 \quad \text{.....} \quad (8.5)$$

where D_1 is the steady-state dilution of the first layer.

8.6 PREDICTING THE GEOMETRY OF HIGH-CHROMIUM WHITE IRON OVERLAYS

8.6.1 Single-Bead Deposits

8.6.1.1 Single-Bead Width

For a particular combination of welding consumable and substrate material, the width of a single-bead deposit, w, can be estimated using the following expression:

$$w = \frac{C_1}{S} + C_2 V I \quad \cdots\cdots\cdots \quad (3.4) \quad \text{(page 44)}$$

where V is the contact tip-to-work voltage, I is the current, S is the travel speed and C_1 and C_2 are constant terms depending on the substrate-consumable combination.

8.6.1.2 Single-Bead Height

The height of a single-bead deposit, h, can be estimated using the following equation:

$$h = \frac{3}{2}\frac{\eta_d f m}{\rho S w} - 84.4\left(\frac{3}{2}\frac{\eta_d f m}{\rho S w}\right)^{2.25} \quad \cdots\cdots\cdots \quad (3.12) \quad \text{(page 57)}$$

where η_d is the deposition efficiency, f is the wire feed rate, m is the mass of the electrode per unit length, ρ is the density of an all-weld metal deposit, S is the travel speed and w is the single-bead width. The deposition rate, W, has been expressed in terms of the wire feed rate in this instance.

8.6.1.3 Single-Bead Penetration

For a single-bead deposit it is possible to predict the dilution, and hence the area of substrate that is melted, with reasonable accuracy. However, the profile of the fusion line and the resulting penetration are more difficult to predict because they are affected by such factors as weld-pool depression and convection within the weld pool. There do not appear to be any general equations for predicting the single-bead penetration, p. Penetration data, however, can be represented approximately by an expression of the following form:

$$p = K\sqrt[3]{\frac{I^4}{S V^2}} \quad \cdots\cdots\cdots \quad (2.6) \quad \text{(page 22)}$$

where K is a fitted constant term, V is the voltage, I is the current and S is the travel speed.

8.6.2 Multi-Pass Overlays

8.6.2.1 Overlay Height

The average height of a multi-pass overlay under steady-state conditions, H_{ss}, is given by:

$$H_{ss} = \frac{\eta_d f m}{\rho S \delta} \quad \cdots\cdots\cdots \quad (8.6)$$

where η_d is the deposition efficiency, f is the wire feed rate, m is the mass of the electrode per unit length, ρ is the density of an all-weld metal deposit, S is the travel speed and δ is the step-over. Note that the numerator in equation 8.6 equates to the deposition rate, W. This expression estimates the average height of an overlay without regard to the uniformity in height.

8.6.2.2 Peak-to-Valley Ripple

The average variation in height between the peak of a bead and the adjacent trough, R, may be estimated using the following expression:

$$R = \left(\frac{\eta_d f m}{\rho S}\right)\left(\frac{12w^2 - 12\delta w + 3\delta^2}{12\delta w^2 - 12\delta^2 w + 2\delta^3}\right)\left(\frac{\delta^2}{(2w-\delta)^2}\right) \quad \cdots\cdots \quad (7.8) \quad \text{(page 139)}$$

where η_d is the deposition efficiency, f is the wire feed rate, m is the mass of the electrode per unit length, ρ is the density of an all-weld metal deposit, S is the travel speed, w is the bead width and δ is the step-over. Once again, the deposition rate, W, is expressed in terms of the wire feed rate, f.

8.7 PREDICTING THE WEAR RATE IN A SPECIFIC ABRASION SYSTEM

In a given wear system, the apparent wear resistance of a composite, W_c^{-1}, can be treated as the reciprocal of the wear rate, W_c (Zum Gahr, 1987). A general empirical expression for the apparent wear resistance, W_c^{-1}, of a material comprising a matrix phase and a reinforcing phase is:

$$W_c^{-1} = W_m^{-1} + \left(W_r^{-1} - W_m^{-1}\right) v^q \quad \cdots\cdots\cdots \quad (4.5) \quad \text{(page 81)}$$

where W_m^{-1} and W_r^{-1} are the apparent wear resistances of the matrix and reinforcement respectively, v is the volume fraction of the reinforcing phase present in the material and q is a fitted parameter.

It should be noted that, when estimating the wear resistance of hardfacing weld deposits, the eutectic mixture should be treated as a single phase even though, in reality, it is a mixture of two distinct constituents. As was seen in chapter 4, the smaller eutectic carbides may not always offer the same resistance to abrasion as the primary carbides and, as such, they should be treated differently.

The procedure for estimating the abrasive wear rate is summarised here:

- Estimate the dilution using the procedure described in section 8.3 if the deposit is a single bead, or section 8.4 if the deposit is a multi-pass overlay. (Section 8.5 will also be required if multiple layers are used.)
- Estimate the composition and microstructure with reference to section 8.2.

- Identify the matrix and reinforcing phases for equation 4.5. For hypoeutectic microstructures the matrix phase comprises the dendrites and the reinforcing phase is the eutectic constituent, *i.e.*:

$$W_m^{-1} = W_{dendrites}^{-1} \quad \text{and} \quad W_r^{-1} = W_{eutectic}^{-1}$$

For hypereutectic structures the eutectic constituent should be treated as the matrix phase and the primary carbides as the reinforcing phase, *i.e.*:

$$W_m^{-1} = W_{eutectic}^{-1} \quad \text{and} \quad W_r^{-1} = W_{primary\ carbides}^{-1}$$

- Estimate the volume fraction of the reinforcing phase present in the microstructure. This is achieved with the assistance of the equation proposed by Maratray and Usseglio-Nanot (1970):

$$TCVF = 12.33[C] + 0.55[Cr] - 15.2 \quad \cdots\cdots \quad (4.1) \quad \text{(page 68)}$$

where $[C]$ and $[Cr]$ are the concentrations by weight of carbon and chromium respectively. Equation 4.1 predicts a total carbide volume fraction (*TCVF*) of approximately 36% for the eutectic constituent at all eutectic compositions on the metastable phase diagram of Jackson (1970). Thus, for hypoeutectic materials it is possible to estimate the *TCVF* and interpolate between 0% and 36% *TCVF* for the volume fraction of the eutectic constituent. Similarly, for the hypereutectic materials it is possible to estimate the *TCVF* and interpolate between 36% and 100% *TCVF* for the volume fraction of primary carbides.

- Estimate the wear resistance and wear rate using equation 4.5. It should be noted that equation 4.5 will only apply to a given wear system since wear resistance is not an intrinsic property of a material (Czichos, 1977). Furthermore, a minimum of three previous wear results will be required to

obtain values for the apparent wear resistances W_m^{-1} and W_r^{-1} and the fitted index, q.

The above procedure completes a link between the selected welding parameters and the abrasive wear performance of the resulting overlay. A schematic representation of this link is shown for both single-bead deposits and multi-pass overlays in Figure 8.3.

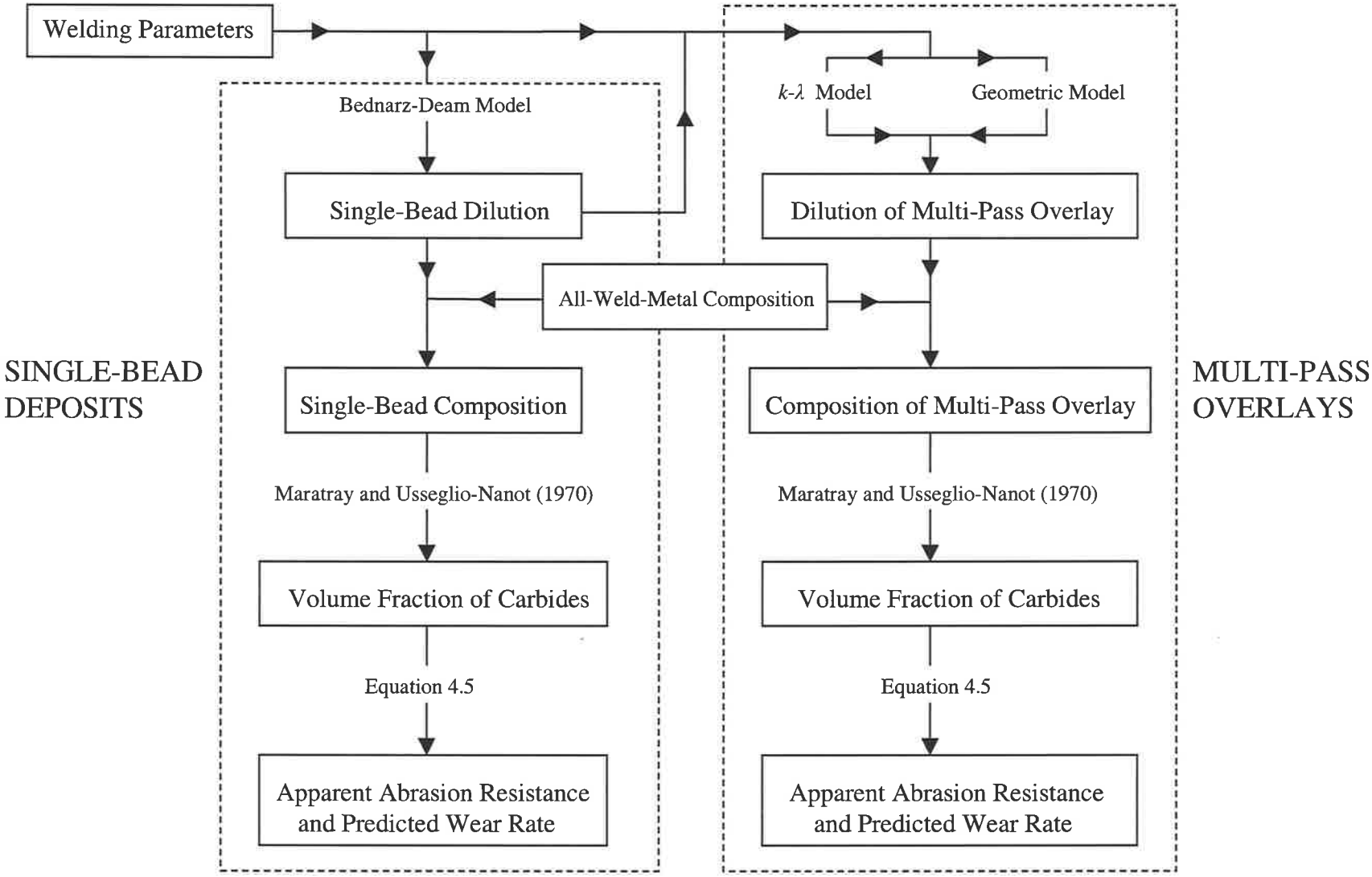

Figure 8.3: - A schematic representation of the link between welding parameters and abrasive wear rate for both single-bead deposits and multi-pass overlays.

9

CONCLUSIONS AND SUGGESTIONS FOR FUTURE RESEARCH

9.1 CONCLUSIONS

At the commencement of the current work the hardfacing industry did not have a systematic procedure for predicting the most important features of a hardfacing overlay, namely the composition and geometry. The current work has culminated in the first set of working principles for the deposition of high-chromium white iron surface layers comprising overlapping beads. It is anticipated that these principles will significantly increase the level of predictability in hardfacing operations, as it is now possible to predict the composition and many of the geometric features of an overlay prior to deposition.

One of the major findings of the current work was that the control of dilution in single-bead deposits and multi-pass overlays are fundamentally different problems. In single-bead deposits minimum dilution can be achieved by minimising the ratio of substrate melted to material deposited, regardless of the dimensions of the bead. In multi-pass overlays, however, there is a height constraint that changes the nature of the problem, so that the objective is to minimise the average penetration subject to the constraint that the overlay height is fixed.

The dilutions of single-bead deposits are adequately predicted by the Bednarz-Deam model. This model resulted in a form of expression that is consistent with observations

of experiments both in the current work and in previous studies. The form of expression was also found to be consistent with the expression for the width of a single bead that was developed in the current work.

Two models were developed in the current work for predicting dilution in multi-pass overlays. The trends in the output from these models were consistent with one another. In fact, the geometric model described in chapter 7 provided accurate predictions of average overlay penetrations directly from first principles. The accuracy of these predictions and the close agreement between the models provided a level of confidence in the output and, as such, the output could be used to draw conclusions and identify trends over a broader range of conditions. Some of the major findings regarding multi-pass overlays were:

- The range of achievable dilutions is a function of the average height of the overlay, with the probability of achieving a low-dilution deposit increasing with increasing overlay height. Consequently, the overlay height also largely determines the range of achievable microstructures and the range of achievable wear performances.
- For an overlay of a given height, the selected welding parameters determine where the dilution lies within the achievable range.
- The two parameters with the strongest effect on overlay dilution are the travel speed and the welding current. Higher travel speeds reduce the dilution of a multi-pass overlay. Reductions in welding current also reduce the dilution but at the expense of deposition rate. In most hardfacing operations the appropriate balance will need to be achieved between wear performance and productivity.

Another parameter that can have a significant bearing on the dilution is the inter-pass temperature. If the component being hardfaced is not allowed to cool adequately between successive passes, the inter-pass temperature will rise and so too will the dilution. Cumulative heating of the work piece can result in large temperature excursions and large variations in wear performance. Care needs to be taken to ensure that, either through cooling systems or the appropriate delays, the inter-pass temperature is maintained within acceptable limits. Care is also necessary when depositing overlays bi-directionally. If the welding head commences each pass immediately after completing its predecessor, the end of the previous bead has not had sufficient time to cool and large variations in dilution can be expected.

With respect to the wear performance of hardfacing weld deposits, a significant observation was made in that the eutectic carbides may not offer the same benefits to wear resistance as the primary carbides. It has been reported previously (Diesburg and Borik, 1974) that fine eutectic structures, which form at high solidification rates, offer inferior abrasion resistance to that offered by coarser structures. The experimental results obtained in the current work are consistent with this report. Consequently, in applications where high volume fractions of carbides are beneficial, it is important to ensure that the microstructure is strongly hypereutectic, so that primary carbides are present in sufficient quantities to provide the desired benefits to wear performance.

For a given abrasive wear system, it is possible to predict the wear performance in service provided that one has access to three previous wear results, the all-weld-metal composition for the consumable and its deposition characteristics. A general form of

expression for the apparent wear resistance of a high-chromium white iron in a given wear system was proposed.

A link between the selected welding parameters, deposit microstructure and the resulting abrasion resistance has now been established.

9.2 SUGGESTIONS FOR FUTURE RESEARCH

In the course of this study several areas were identified as warranting further investigation. The following areas deserve specific mention:

- The relationship between deposition rate and welding parameters such as voltage, current and work distance requires further work. It is known (Kiyohara *et al.*, 1980) that the welding voltage does affect the deposition rate but none of the equations presented in the literature incorporate any voltage effects. At present it is possible to achieve the correct overlay height by setting the deposition rate directly. (The deposition rate can be set by the correct choice of wire feed rate and knowledge of the deposition efficiency.) However, for a given wire feed rate, it is necessary to predict the current that will be drawn from the welding power supply in order to estimate the resulting penetration and hence dilution with sufficient accuracy. It is anticipated that an improved understanding of the factors that affect the deposition rate will bring benefits to both hardfacing and the broader field of welding science.
- The factors affecting the distribution of heat in arc welding of dissimilar metals are not well understood. Further work is required to establish the

causes of, and to quantify, any biases that may arise in the melting of each material.

- It may not always be practical to deposit an overlay exclusively in the down-hand position. It would be valuable to extend the principles developed in the current work to out-of-position welding.
- The possibility arises for an alternative process to bring further improvements to the control of dilution and hence the wear performance of overlays. At present it is not possible to control the deposition rate independently of the amount of substrate that is melted by virtue of the fact that the welding current is intimately related to both of these quantities. If the heat delivered to the substrate were to be divorced from the deposition rate by employing alternative technology (*i.e.* a process other than a consumable-electrode process) it is possible that a greater degree of control over dilution will be achieved.
- The field trials demonstrated that, when exposed to impact, single-layer hypereutectic white iron overlays are susceptible to spalling and fracture. Further work is required to establish whether this is a general characteristic of hypereutectic weld deposits or whether the root cause lies elsewhere. For example, the residual stresses in single-layer hypereutectic overlays may be sufficient in themselves to cause spalling, and significant improvements may be observed if a hypereutectic second layer were to be deposited on to a high-dilution buffering layer. Another possible cause for the apparent susceptibility of hypereutectic deposits to spalling is the formation of the

complex regular microstructure. If an interlinked carbide network were present, it would provide continuous paths for crack propagation.

- Further work is required to compare the wear performance of complex regular microstructures with conventional hypereutectic microstructures that have equivalent total carbide volume fractions. Very little is known about the wear properties of complex regular white-iron microstructures.

10

REFERENCES

ANTON, H. and RORRES, C. (1987): "Elementary Linear Algebra with Applications", *John Wiley and Sons*, pp. 229 – 230.

ARNOLD, B.K., BEDNARZ, B., FRANCIS, J.A., JONES, E.P. and BEE, J. (1998): "Principles for Weld Deposition of Hardfacing – Field Trials", CRC Project 95:23, Final Report – Part 2.

ASHIDA, T., YOSHIDA, H. and SUGIOKA, S., Kurimoto Ltd. (1994): "Multi-Layer Welding Process with High Hard Metal", *Australian Patent AU-B-87877/91.*

ASM HANDBOOK (1992): "Volume 18 – Friction, Lubrication, and Wear Technology", *ASM International*, pp. 184.

ASM HANDBOOK (1993a): "Volume 6 – Welding, Brazing and Soldering", *ASM International*, pp.1208.

ASM HANDBOOK (1993b): "Volume 6 – Welding, Brazing and Soldering", *ASM International*, pp. 789 - 792.

AVERY, H.S. (1961): "The Measurement of Wear Resistance", *Wear*, **4**, 427 – 449.

AVERY, H.S. and CHAPIN, H.J. (1952): "Hard-Facing Alloys of the Chromium Carbide Type", *Welding Journal*, **31** (10), 917 – 930.

AWS WELDING HANDBOOK (1991): "Volume 2 - Welding Processes", 8th Edn., *American Welding Society*, 133 – 135.

BAESLACK, W.A. III, LIPPOLD, J.C. and SAVAGE, W.F. (1979): "Unmixed Zone Formation in Austenitic Stainless Steel Weldments", *Welding Journal*, **58** (6), 168s – 176s.

BEDNARZ, B. (1996): *Private Communication.*

BERNS, H. and FISCHER, A. (1986): "Abrasive Wear Resistance and Microstructure of Fe-Cr-C-B Hard Surfacing Weld Deposits", *Wear*, **112**, 163 – 180.

CHERMANT, J.L. and OSTERSTOCK, F. (1976): "Fracture Toughness and Fracture of WC-Co Composites", *Journal of Materials Science*, **11**, 1939 – 1951.

CHRISTENSEN, N., DAVIES, V. De L. and GJERMUNDSEN, K. (1965): "Distribution of Temperatures in Arc Welding", *British Welding Journal*, **12**, 54 - 75.

COOKSON, C.P. (1982): "Hardness v. Wear Resistance", *Surfacing Journal*, **13** (2), 32 – 34.

CZICHOS, H. (1977): "A Systems Analysis Data Sheet for Friction and Wear Tests and an Outline for Simulative Testing", *Wear*, **41**, 45 – 55.

CZICHOS, H. (1978): "Tribology – A Systems Approach to the Science and Technology of Friction, Lubrication and Wear", Tribology Series, **1**, *Elselvier*.

de SAIRRE BALSAMO, P.S., SCOTTI, A. and BIASOLI de MELLO, J.D. (1995): "Interpretacion de la Microestructura de Recargues Duros Depositados por Soldadura Utilizando la Superficie de Liquidus de Diagramas Fe-Cr-C, *Revista de Soldadura*, **25** (4), 199 – 207.

DEAM, R.T. (1996): "Surfacing: Process Modelling Considerations", *Private Communication*.

DICK, I.R. (1991): "A Computer-Based Welding Data Monitor", In Proceedings of the 39th Annual WTIA Conference *Welding Towards 2000*, August, Surfers Paradise, Australia.

DIESBURG, D.E. and BORIK, F. (1974): Optimising Abrasion Resistance and Toughness in Steels and Irons for the Mining Industry, in Proceedings Symp. *"Materials for the Mining Industry"*, Vail, CO, July, Climax Molybdenum Company, 15 - 38.

DOGAN, O.N. and HAWK, J.A. (1995): "Effect of Carbide Orientation on Abrasion of High Cr White Cast Iron", *Wear*, **189**, 136 – 142.

DuPONT, J.N. and MARDER, A.R. (1996): "Dilution in Single Pass Arc Welds", Metallurgical and Materials Transactions B, **27B**, 481 – 489.

EAGAR, T.W. and TSAI, N.-S. (1983): "Temperature Fields Produced by Travelling Distributed Heat Sources", *Welding Journal*, **62** (12), 346s – 354s.

ELLIOTT, R. (1983a): "Eutectic Solidification Processing: Crystalline and Glassy Alloys", *Butterworths*, London, pp. 147.

ELLIOTT, R. (1983b): "Eutectic Solidification Processing: Crystalline and Glassy Alloys", *Butterworths*, London, pp. 169.

ELLIS, T. (1985): "An Evaluation of the Effects of Process Variables in the Flux-Cored Arc Welding Process on the Wear Resistance of Hardfacing Deposits", M.Sc. Dissertation, University of the Witwatersrand, Johannesburg, South Africa.

ELLIS, T. and GARRETT, G.G. (1986): "Influence of Process Variables in Flux Cored Arc Welding of Hardfacing Deposits", *Surface Engineering*, **2** (1), 55 - 66.

EROKHIN, A.A. (1979): "Force Exerted by the Arc on the Metal being Melted", *Avt. Svarka*, (7), 21 – 26.

FARMER, H.N. (1966a): "How to Control Dilution in Weld Overlays – Part 1", *Welding Design and Fabrication*, **39** (10), 85 – 86.

FARMER, H.N. (1966b): "How to Control Dilution in Weld Overlays – Part 2", *Welding Design and Fabrication*, **39** (11), 62 – 63.

FARMER, H.N. (1974): "Factors Affecting Selection and Performance of Hard-Facing Alloys", in Proceedings Symp. *"Materials for the Mining Industry"*, Vail, CO, July, 85 – 91.

FORSBERG, S.G. (1985): "Resistance Electroslag (RES) Surfacing", *Welding Journal*, **64** (8), 41 – 48.

FRANCIS, J.A. and JONES E.P. (1997): "The Influence of Welding Parameters on the Wear Performance of High Chromium White Iron Hardfacing Alloys", *WTIA National Seminars*, July, Mackay, Australia.

FRANCIS, J.A., BEDNARZ, B., ARNOLD, B.K., JONES, E.P. and BEE, J. (1998): "Principles for Weld Deposition of Hardfacing", CRC Project 95:23, Final Report – Part 1.

FRENCH, I.E. (1984): "Effects of Electrode Extension on Deposit Characteristics and Metal Transfer of E70T-4 Electrodes", *Welding Journal*, **63** (6), 167s – 172s.

FRIEDMAN, E. (1978): "Analysis of Weld Puddle Distortion and Its Effect on Penetration", *Welding Journal*, **57** (6), 161s – 166s.

FULCHER, J.K., KOSEL, T.H. and FIORE, N.F. (1983): "The Effect of Carbide Volume Fraction on the Low-Stress Abrasion Resistance of High Cr-Mo White Cast Irons", *Wear*, **84**, 313 – 325.

GORMAN, R. (1997): *Private Communication.*

GUNDLACH, R. B. and PARKS, J.L. (1978): "Influence of Abrasive Hardness on the Wear Resistance of High Chromium Irons", *Wear*, **46**, 97 – 108.

HALMØY, E. (1979): "Wire Melting Rate, Droplet Temperature and Effective Anode Melting Potential", *Proceedings of the International Conference on Arc Physics and Weld Pool Behaviour*, London.

HEIPLE, C.R. and ROPER, J.R. (1982): "Mechanism for Minor Element Effect on GTA Fusion Zone Geometry", *Welding Journal*, **61** (4), 97s – 102s.

HINKEL, J.E. (1968): "Long Stickout Welding – A Practical Way to Increase Deposition Rates", *Welding Journal*, **47** (11), 869 – 874.

HIRAOKA, K., OKADA, A. and INAGAKI, M. (1986): "Effect of Electrode Geometry on Maximum Arc Pressure in Gas Tungsten Arc Welding", *Transactions of National Research Institute for Metals*, **28** (1), 63 – 70.

HIRATA, Y. (1995): "Physics of Welding III – Melting Rate and Temperature Distribution of Electrode Wire", *Welding International*, **9** (5), 348 – 351.

HOULDCROFT, P.T. (1954): "Part III – Dilution and Uniformity in Alloy Weld Beads", *British Welding Journal*, October, 468 – 472.

HUTCHINGS, I.M. (1992): "Tribology – Friction and Wear of Engineering Materials", *Edward Arnold.*

JACKSON, C.E. and SHRUBSALL, A.E. (1953): "Control of Penetration and Melting Ratio with Welding Technique", *Welding Journal*, **32** (4), 172s – 178s.

JACKSON, R.S. (1970): "The Austenite Liquidus Surface and Constitutional Diagram for the Fe-Cr-C Metastable System", *Journal of the Iron and Steel Institute*, **208**, 163 – 167.

KALLIGERAKIS, K. and MELLOR, B.G. (1995): "Overlay Welding Using Pulsed MIG Welding: Bead Profile and Dilution", *International Journal for the Joining of Materials*, **7** (1), 16 – 22.

KHRUSCHOV, M.M. (1957): "Resistance of Metals to Wear by Abrasion, as Related to Hardness", paper 46 in *Proceedings of the Conference on Lubrication and Wear*, October, London, England.

KIM, I.S., BASU, A. and SIORES, E. (1994): "Mathematical Models for Optimal Weld Bead Geometry for GMAW Process", Ph.D Student Report, Wollongong University.

KIM, J.–W. and NA, S.–J. (1995): "A Study on the Effect of Contact Tube-to-Workpiece Distance on Weld Pool Shape in Gas Metal Arc Welding", *Welding Journal*, **74** (5), 141s – 152s.

KIYOHARA, M., YAMAMOTO, H. and HARADA, S. (1979): "Melting Characteristics of a Wire Electrode in the MIG-Welding of Aluminium", Paper 26 in Proceedings of the Conference *Arc Physics and Weld Pool Behaviour*, May, London, England.

KOTECKI, D.J. (1996): "Dilution Control in Single-Wire Stainless Steel Submerged Arc Cladding", *Welding Journal*, **75** (2), 35s – 45s.

KOU, S. and SUN, D.K. (1985): "Fluid Flow and Weld Penetration in Stationary Arc Welds", *Metallurgical Transactions A*, **16A**, 203 – 213.

KOU, S. and WANG, Y.H. (1986): "Weld Pool Convection and Its Effect", *Welding Journal*, **65** (3), 63s – 70s.

LAIRD, G., II. and POWELL, G.L.F. (1993): "Solidification and Solid-State Transformation Mechanisms in Si Alloyed High-Chromium White Cast Irons", *Metallurgical Transactions A*, **24A**, 981 – 988.

LANCASTER, J.F. (1986): "The Physics of Welding", 2nd Edn., *Permagon Press*, pp. 281.

LESNEWICH, A. (1958): "Control of Melting Rate and Metal Transfer in Gas-Shielded Metal-Arc Welding, Part 1 – Control of Electrode Melting Rate", *Welding Journal*, **37** (8), 343s – 353s.

LIN, M.L. and EAGAR, T.W. (1985): "Influence of Arc Pressure on Weld Pool Geometry", *Welding Journal*, **64** (6), 163s – 169s.

LIN, M.L. and EAGAR, T.W. (1986): "Pressures Produced by Gas Tungsten Arcs", *Metallurgical Transactions B*, **17B** (3), 601 – 607.

LIPPOLD, J.C. and SAVAGE, W.F. (1980): "Solidification of Austenitic Stainless Steel Weldments: Part 2 – The Effect of Alloy Composition on Ferrite Morphology", *Welding Journal*, **59** (2), 48s – 58s.

MARATRAY, F. and USSEGLIO-NANOT, R. (1970): Factors Affecting the Structure of Chromium and Chromium-Molybdenum White Irons. AMAX Inc. Paris, France.

MARTIN, P.J., TAYLOR, W.A. and BAHRANI, A.S. (1991): "Weld Bead Geometry Prediction for Self-Shielded Flux-Cored Arc Welding", *Joining Sciences*, **1** (1), 49 – 53.

McGLONE, J.C. (1982): "Weld Bead Geometry Prediction – A Review", *Metal Construction*, July, 378 – 384.

MENON, R. (1996): "New Developments in Hardfacing Alloys", *Welding Journal*, **75** (2), 43 – 49.

MOORE, M.A. (1974): "The Relationship Between the Abrasive Wear Resistance, Hardness and Microstructure of Ferritic Materials", *Wear*, **28**, 59 – 68.

MUSCARA, J. and SINNOTT, M.J. (1972): "Construction and Evaluation of a Versatile Abrasive Wear Testing Apparatus", *Metals Engineering Quarterly*, **12** (2), 21 - 32.

NOBLE, D.N. (1985): "Abrasive Wear Resistance of Hardfacing Weld Deposits", *Metal Construction*, September, 605 – 611.

OH, Y.K., DEVLETIAN, J.H. and CHEN, S.J. (1990): "Low-Dilution Electroslag Cladding for Shipbuilding", *Welding Journal*, **69** (8), 37 – 44.

POWELL, G.L.F. (1979): "The Microstructure of Hypereutectic Cr-C Hard Surfacing Deposits and its Dependence on Welding Variables", *Australian Welding Research*, January, 16 – 23.

POWELL, G.L.F. and LAIRD, G. (1992): Structure, Nucleation, Growth and Morphology of Secondary Carbides in High Chromium and Cr-Ni White Cast Irons. *Journal of Materials Science*, **27**, 29 - 35.

POWELL, G.L.F., CARLSON, R.A. and RANDLE, V. (1994): The Morphology and Microtexture of M_7C_3 Carbides in Fe-Cr-C and Fe-Cr-C-Si Alloys of Near Eutectic Composition. *Journal of Materials Science*, **29**, 4889 - 4896.

POWELL, G.L.F., FRANCIS, J.A., BEDNARZ, B. and LLOYD, P.G. (1997): "Undercooling and Welding Metallurgy", Paper 49 in Proceedings of the 45th Annual WTIA Conference *Technological Developments and Advances for Australian Industry*, November, Melbourne, Australia.

RAVEENDRA, J. and PARMAR, R.S. (1987): "Mathematical Models to Predict Weld Bead Geometry for Flux Cored Arc Welding", *Metal Construction*, January, 31R – 35R.

RENSE, C.E.C., EDWARDS, G.R. and FROST, H.R. (1983): The Effect of Open-Arc Process Variables on the Microstructure and Wear Resistance of a Typical Chromium-Carbide-Type Hardfacing Deposit. *Journal of Materials for Energy Systems*, **5** (3), 149 - 159.

RHEE, S. and KANNATEY-ASIBU, E. Jr. (1993): "Melting Rate and Heat Flow for Wire Electrode in GMAW", *Joining Sciences*, **1** (4), 231 – 236.

RICHARDSON, R.C.D. (1967): "The Maximum Hardness of Strained Surfaces and the Abrasive Wear of Metals and Alloys, *Wear*, **10**, 353 – 382.

RIVLIN, V.G. (1984): "Critical Review of Constitution of Carbon-Chromium-Iron and Carbon-Iron-Manganese Systems", *International Metals Reviews*, **29**, 299 - 327.

ROKHLIN, S.I. and GUU, A.C. (1993): "A Study of Arc Force, Pool Depression, and Weld Penetration During Gas Tungsten Arc Welding", Welding Journal, **72** (8), 381s – 390s.

ROSENTHAL, D. (1941): "Mathematical Theory of Heat Distribution During Welding and Cutting", *Welding Journal*, **20** (5), 220s – 234s.

RYKALIN, N.N. (1951): "Calculation of Heat Flow in Welding", Moscow.

SARE, I.R. (1979): "Abrasion Resistance and Fracture Toughness of White Cast Irons", *Metals Technology*, November, 412 – 419.

SARE, I.R. and CONSTANTINE, A.G. (1991): "Design and Analysis of Jaw-Crusher Gouging Abrasion Tests", *ASTM Journal of Testing and Evaluation*, **19** (2), 115 – 122.

SMITH, D.C. (1970): "Flux-Cored Electrodes – Their Composition and Use", *Welding Journal*, **49** (7), 535 – 547.

STEVENSON, A.N.J. (1995): "Wear and Microstructure of Weld-Hardfacing Deposits of High Chromium White Cast Irons", Ph.D Thesis, University of Cambridge, Cambridge, U.K.

SWIFT-HOOK, D.T. and GICK, E.F. (1973): "Penetration Welding With Lasers", *Welding Journal*, **52** (11), 492s – 499s.

TABRETT, C.P. (1997): "Microstructure-Property Relationships in High Chromium White Irons", Ph.D Thesis, University of South Australia, Adelaide, Australia.

TARASOV, V.V. et al (1975): "Heterogeneity in the Structure of Iron Found During Multipass Surfacing", *Avt. Svarka*, (3), 73 – 74.

THORPE, W.R. (1980): "The Effect of Welding Variables in Automatic Open-Arc Hard Facing with an Austenitic Chromium Carbide Alloy". *Metals Forum*, **3** (1), 62 - 73.

THORPE, W.R. and CHICCO, B. (1985): "The Fe-Rich Corner of the Metastable C-Cr-Fe Liquidus Surface", *Metallurgical Transactions A*, **16A** (9), 1541 – 1549.

USHIO, M., FAN, D., MURATA, Y. and MATSUDA, F. (1985): "Melting Phenomena of Flux Cored Wire", *Transactions of JWRI*, **14** (2), 9 – 16.

WELLS, A.A. (1952): "Heat Flow in Welding", *Welding Journal*, **31** (5), 263s – 267s.

WITTKE, P. (1990): "Preventive Hardsurfacing of Pipes in a Vertical Thermal Catalitic Cracking Tower", *Australian Welding Journal*, **35** (1), 13 - 14.

WTIA : TECHNICAL NOTE 1 (1996): "The Weldability of Steels", *Welding Technology Institute of Australia.*

YELLUP, J.M. and ARNOLD, B.K. (1996): "A Literature Review on The Effect of Welding Parameters Upon Wear Properties of Weld Deposited Chromium White Iron Surfaces", CRC No. 17, *Australian Welding Research.*

YELLUP, J.M., ARNOLD, B.K., FRANCIS, J.A. and BEE, J.V. (1996): "Development of a Hardfacing Procedure – The Significance of Welding Parameters", *WTIA National Seminars*, July - August, Gladstone, Perth and Newcastle, Australia.

YELLUP, J.M., and SMOKER, K. (1995): "The Effect of Welding Parameters on the Properties of Hardfacing Alloys". *Proceedings of the IMMA/WTIA Welding and Joining Conference*, Adelaide, August 1995.

ZOLLINGER, O., BECKHAM, J.E. and MONROE, C. (1998): "What to Know Before Selecting Hardfacing Electrodes", *Welding Journal*, **77** (2), 39 – 43.

ZUM GAHR, K.-H. (1987): "Microstructure and Wear of Materials", Tribology Series, 10, *Elselvier*.

ZUM GAHR, K.-H. and DOANE, D.V. (1980): "Optimising Fracture Toughness and Abrasion Resistance in White Cast Irons", *Metallurgical Transactions A*, **11A**, 613 – 620.

ZUM GAHR, K.-H. and ELDIS, G.T. (1980): "Abrasive Wear of White Cast Irons", *Wear*, **64**, 175 - 194.

APPENDIX 1:- EXAMPLES OF THE OUTPUT FROM THE *k-λ* SPREADSHEET PROGRAM

A spreadsheet program was developed based on the *k-λ* model for multi-pass overlays described in chapter 6. The original spreadsheet was developed solely by the author and applied to develop welding conditions for overlays trialed in the alumina industry (see Arnold *et al.*, 1998). The spreadsheet was subsequently refined and expanded with the assistance of Dr. B. Bednarz of CSIRO Manufacturing Science and Technology. Full details are presented in Francis *et al.* (1998).

Examples of the output from the final version of the *k-λ* spreadsheet program are included at the end of the appendix. A worksheet for 4mm high single-layer weld overlays is shown. The user may enter data in areas that are shaded yellow. There are two yellow boxes in the top-left hand corner of the worksheet where the user can enter the substrate and consumable composition. Also within the purple region there is a yellow box where information relating to the deposition rate can be entered.

There are three main user areas in the worksheet. The first, User Area "A", shows output for a matrix of different welding conditions. In this area the user may change only the voltage. It was intended that this area would give the user an appreciation of the effects of different welding variables. For example, given a consumable with an all-weld-metal composition of 25wt.% Cr and 5wt.% C (and deposition properties as given on the worksheet), deposited on to a mild steel substrate, a low-dilution welding condition is the following;

28V, 350A, 40mm work distance and 900mm/min. The calculated steady-state dilution is 24% and the corresponding carbon and chromium concentrations are 3.8% and 19.0% respectively. The overlay would be hypereutectic. The predicted ripple is 0.7mm using an approximation developed prior to the one presented in this thesis. The earlier version is also given in Francis *et al.* (1998).

The second area, User Area "B", allows the user to enter any combination of voltage, current, work distance and travel speed. In this area the spreadsheet will automatically calculate the step-over that is required to achieve a 4mm high overlay. Predictions of various parameters, including the steady-state overlay dilution, are then given. In User Area "B", four sets of welding conditions can be compared simultaneously for a specified height of 4mm.

Finally, User Area "C" allows the user to enter the voltage, current, work distance, travel speed and step-over. The spreadsheet will then estimate the steady-state overlay height that will result from the welding conditions that were entered (*i.e.* the height is no longer restricted to 4mm). Predictions of various parameters, such as the steady-state overlay dilution, are then given. In User Area "C" four different sets of welding parameters can also be compared simultaneously.

It can be seen that the worksheet does not give predictions for all of the entered welding conditions. The predicted steady-state dilution *etc.* will only be given if the welding condition is deemed to be viable, and there is a column in the worksheet that states whether the welding condition is expected to be viable or not. The viability of a welding condition

is based on the estimated overlap. Bead overlaps between 40 and 60% are generally recommended (Gorman, 1997). Overlaps higher than 60% are likely to result in a low average penetration and, if the penetration is inconsistent, lack of fusion may occur. Conversely, if the estimated overlap is below 40%, the peak-to-valley ripple may be large. In the example shown, an overlay is deemed to be viable if the estimated overlap is between 40 and 60%. However, the user may alter these limits by adjusting the viability parameter at the top of User Area "A". The limits on bead overlap are set to "50 ± viability parameter". The viability parameter is set to 10% in this example so the limits on bead overlap are 50 ± 10%, i.e. 40 and 60%.

The columns in red predict the wire feed rate that corresponds to the entered welding condition. The estimated steady-state height of the overlay is based on this estimated wire feed rate. This column is highlighted to emphasize that it is possible to ensure that the correct overlay height is achieved by controlling the wire feed rate directly.

The worksheet shown is for 4mm high single-layer overlays. The complete *k-λ* spreadsheet program also has worksheets for 2mm, 3mm, 5mm and 6mm high single-layer overlays. In addition, two worksheets are included for double layers. One applies to a 2mm high overlay being deposited on another 2mm high overlay. The other applies to a 3mm high overlay being deposited on another 3mm high overlay.

4 mm single-layer overlay

Substrate composition [data below are for mild steel]							
% Carbon	0.2	Substrate thermal conductivity in Watts per metre.Kelvin		40	T1	1250	
% Chromium	0.0	Initial temperature of substrate in Celsius		20	T2	150	
All weld metal wire composition [if available, use analysis for the particular batch of wire, otherwise refer to manufacturer's data sheet]							
% Carbon	5.0	Deposition efficiency in %	95				
% Chromium	25.0	Wire feed speed at 28V,40mm and 300A	2.81				
Polarity	dcep	Wire feed speed at 28V,40mm and 400A	4.33				
Wire diameter (mm)	2.8	Wire weight in grams per metre	36	Wire sheath material		mild steel	
Deposition rate parameters [these data are calculated from measured wire feed speeds]							
dep1	8.46E-03						
dep1a	3.01E-02						
dep2	7.49E-07						
dep2a	3.01E-02						
Single bead dilution parameters [generic data]							
dil1	4.35E-04						
dil2	8.12E-08						
Bead width parameters [generic data]							
w1	2.34E+03						
w2	8.10E-04						
w3	0.00E+00						
Specified overlay height [usually specified by the user of the clad material]							
H(mm)	4						

OVERLAY SPREADSHEET, Version 1.1, April, 1998.

Disclaimer

Every effort has been made to supply reliable data and formulae.
With respect to data either supplied in these worksheets or derived from the use of these worksheets, the CRC for Materials Welding and Joining has not made any warranties and excludes all warranties either express or implied including any implied warranty of merchantability or of fitness for a particular purpose. In no event will the CRC be liable for direct, indirect, special, incidental, or consequential damages arising out of the use of or inability to use data supplied or results derived.
The principles underlying this worksheet have not been assessed with respect to side product generation and emission of metal fume. The user should give appropriate attention to the control of fume emissions in accord with the scale of operations. The Environment Protection Act (1993) and its associated Air Quality Policy (1994) should be consulted regarding limits of metal fume in emissions, as well as the requirement to take all practicable steps to minimise those emissions. Where fume is generated in the workplace, the duty of care provisions of the OHS & W Act (1986) and Division 5.9 of the associated regulations apply. The exposure of those persons operating the process must be rigorously minimised by means of adequate ventilation.

ESTIMATED OVERLAY PROPERTIES FOR DEPOSITS PUT DOWN AT 28 VOLTS

VIABILITY PARAMETER, % 10 — **USER AREA "A"**

voltage	current	work_dist	tr_speed	heat input	cooling time	dep_rate	wire_feed	coverage	s_b_dil	bead width	stepover	overlap	viability		penetration	mean_dil	mean_C	mean_Cr	ripple
volts	amps	mm	mm/minute	kJ/mm	seconds	kg per hr	metres/min.	hr per sq.m	%	mm	mm	%	Yes or No		mean, mm	%	%	%	mm
28	300	20	300	1.7	46	4.1	2.01	7.4	52	15	7.6	48	Yes		1.7	30	3.5	17.4	1.2
28	300	20	600	0.8	23	4.1	2.01	7.4	55	11	3.8	65	No						
28	300	20	900	0.6	15	4.1	2.01	7.4	59	9	2.5	73	No						
28	300	30	300	1.7	46	4.9	2.41	6.1	47	15	9.0	38	No						
28	300	30	600	0.8	23	4.9	2.41	6.1	51	11	4.5	58	Yes		1.3	25	3.8	18.8	0.8
28	300	30	900	0.6	15	4.9	2.41	6.1	54	9	3.0	68	No						
28	300	40	300	1.7	46	5.8	2.81	5.3	43	15	10.5	28	No						
28	300	40	600	0.8	23	5.8	2.81	5.3	47	11	5.3	51	Yes		1.4	25	3.8	18.6	1.1
28	300	40	900	0.6	15	5.8	2.81	5.3	51	9	3.5	63	No						
28	350	20	300	2.0	54	5.0	2.45	6.0	51	16	9.2	42	Yes		2.0	33	3.4	16.6	1.5
28	350	20	600	1.0	27	5.0	2.45	6.0	56	12	4.6	61	No						
28	350	20	900	0.7	18	5.0	2.45	6.0	59	11	3.1	71	No						
28	350	30	300	2.0	54	6.1	2.99	5.0	46	16	11.2	29	No						
28	350	30	600	1.0	27	6.1	2.99	5.0	51	12	5.6	53	Yes		1.5	27	3.7	18.2	1.0
28	350	30	900	0.7	18	6.1	2.99	5.0	54	11	3.7	65	No						
28	350	40	300	2.0	54	7.3	3.53	4.2	42	16	13.3	16	No						
28	350	40	600	1.0	27	7.3	3.53	4.2	46	12	6.6	44	Yes		1.6	28	3.6	18.0	1.4
28	350	40	900	0.7	18	7.3	3.53	4.2	50	11	4.4	58	Yes		1.3	24	3.8	19.0	0.7
28	400	20	300	2.2	61	6.0	2.92	5.1	51	17	10.9	35	No						
28	400	20	600	1.1	31	6.0	2.92	5.1	56	13	5.5	58	Yes		1.6	28	3.6	17.9	0.8
28	400	20	900	0.7	20	6.0	2.92	5.1	60	12	3.6	69	No						
28	400	30	300	2.2	61	7.4	3.62	4.1	45	17	13.6	19	No						
28	400	30	600	1.1	31	7.4	3.62	4.1	50	13	6.8	48	Yes		1.7	30	3.6	17.6	1.2
28	400	30	900	0.7	20	7.4	3.62	4.1	54	12	4.5	61	No						
28	400	40	300	2.2	61	8.9	4.33	3.4	41	17	16.2	4	No						
28	400	40	600	1.1	31	8.9	4.33	3.4	46	13	8.1	37	No						
28	400	40	900	0.7	20	8.9	4.33	3.4	50	12	5.4	54	Yes		1.4	26	3.7	18.5	0.9
28	450	20	300	2.5	69	7.0	3.41	4.3	51	18	12.8	29	No						
28	450	20	600	1.3	34	7.0	3.41	4.3	56	14	6.4	55	Yes		1.7	30	3.5	17.4	0.9
28	450	20	900	0.8	23	7.0	3.41	4.3	60	13	4.3	67	No						
28	450	30	300	2.5	69	8.8	4.30	3.4	45	18	16.1	10	No						
28	450	30	600	1.3	34	8.8	4.30	3.4	50	14	8.1	43	Yes		1.9	32	3.5	17.1	1.5
28	450	30	900	0.8	23	8.8	4.30	3.4	54	13	5.4	58	Yes		1.5	27	3.7	18.2	0.8
28	450	40	300	2.5	69	10.7	5.20	2.8	40	18	19.5	0	No						
28	450	40	600	1.3	34	10.7	5.20	2.8	45	14	9.7	31	No						
28	450	40	900	0.8	23	10.7	5.20	2.8	50	13	6.5	49	Yes		1.6	28	3.6	17.9	1.1

USER AREA "B"

USER AREA FOR ASSESSING OTHER COMBINATIONS OF PARAMETERS FOR SPECIFIED HEIGHT
ESTIMATED OVERLAY PROPERTIES FOR USER-CHOSEN COMBINATIONS — H (mm) 4

voltage	current	work_dist	tr_speed	heat input	cooling time	dep_rate	wire_feed	coverage	s_b_dil	bead width	stepover	overlap	viability		penetration	mean_dil	mean_C	mean_Cr	ripple
28	400	20	800	0.8	23	6.0	2.92	5.1	58	12	4.1	66	No						
26	350	30	800	0.7	19	6.4	3.14	4.7	49	10	4.4	57	Yes		1.3	24	3.9	19.0	0.8
28	450	20	1000	0.8	21	7.0	3.41	4.3	61	13	3.8	69	No						
26	400	30	500	1.2	34	7.8	3.80	3.9	45	13	8.6	35	No						

USER AREA "C"

ESTIMATED OVERLAY PROPERTIES FOR USER-CHOSEN STEP-OVER, HEIGHT IS NOW CALCULATED

voltage	current	work_dist	tr_speed	stepover	bead width	heat input	cooling time			dep_rate	wire_feed	height	coverage	s_b_dil	overlap	viability		penetration	mean_dil	mean_C	mean_Cr	ripple
28	300	20	300	6.0	15	1.7	46			4.1	1.99	5.0	9.3	52	59	Yes		1.3	21	4.0	19.8	0.9
28	300	20	600	6.0	11	0.8	23			4.2	2.04	2.6	4.6	55	44	Yes		1.7	40	3.1	15.0	0.9
28	300	20	900	6.0	9	0.6	15			4.2	2.06	1.7	3.1	58	36	No						
28	450	40	500	6.0	15	1.5	41			10.3	5.03	7.5	5.6	45	60	Yes		0.5	6	4.7	23.4	1.3